MULTI-SCALE HOMOGENIZATION OF MOVING INTERFACE PROBLEMS WITH FLUX AND FIELD JUMPS

by

Sangmin Lee

A dissertation submitted in partial fulfillment
of the requirements for the degree of
Doctor of Philosophy
(Mechanical Engineering)
in The University of Michigan
2011

Doctoral Committee:

Assistant Professor Veera Sundararaghavan, Co-Chair
Professor Anthony M. Waas, Co-Chair
Associate Professor Krishna Garikipati
Assistant Professor Anton Van der Ven

To my grandmother

ACKNOWLEDGEMENTS

This dissertation is a milestone in my life, and I would like to express my sincere appreciation to the people who made it possible, especially my advisor Veera Sundararaghavan and my parents. During a Ph.D program, course work, the qualifying exam, and research might not be happy activities for graduate students, but at the end there is pleasure and satisfaction at having completed the program. Now I recognize these accomplishments were possible because of the many people who continuously supported me.

Being a Ph.D student requires not only knowledge about the research field but also good relationships with colleagues and advisors. Professor Sundararaghavan was a great research advisor. He always treated me with respect, like a coworker, and let me make the important research decisions. In our regular meetings, he helped me see the large perspective as well as the important details. His continuous support encouraged and guided my research. I also have had a special privilege of being advised by Professor Anthony M. Waas. It has been an honor to receive academic guidance, instruction, encouragement, and insight from him throughout my doctoral study.

The first course that I took in the University of Michigan was with Professor Krishna Garikipati. Without any notes, he taught Continuum Mechanics and Finite Element Method seamlessly. I have tremendous gratitude for his serving on my thesis committee and I appreciate learning from an excellent Professor.

Deep appreciation goes to rest of my thesis committee, Professor Anton Van der Ven for his time, dedication and valuable advice.

I gratefully acknowledge the support of my research sponsor, NASA Constellation University Institutes Project under grant NCC3-989 with Claudia Meyer as the project manager.

Now, being a father, I understand how much love has been given to me by my parents. Boksun Kim, my mother, and Changhyun Lee, my father, love and support me and my brothers endlessly. My father was a farmer also started without his own land, but now our family has one Ph.D, two restaurant owners, and one university student. I grew up helping my parents with their fall harvest, and experienced how difficult farming is. I dedicate this thesis to my parents in appreciation for all their love and sacrifice. They are the heros in my life.

The most precious present from God in my Ann Arbor life is Grace Hyorim Lee, my daughter. Your smile and even your cries always please me.

Finally, words do not come easy to describe the dedication of my wife, Hyejin Kim. Her sacrifice staying with me in a totally different culture and foreign country will never be forgotten. Your being with me generates a great power inside me. I love you.

TABLE OF CONTENTS

DEDICATION . . . . . **ii**

ACKNOWLEDGEMENTS . . . . . **iii**

LIST OF FIGURES . . . . . **vii**

LIST OF TABLES . . . . . **xi**

LIST OF APPENDICES . . . . . **xii**

ABSTRACT . . . . . **xiii**

CHAPTER

I. Introduction 1

1.1 Overview 1
1.2 Literature review 2

II. Multi-scale homogenization with flux jumps - Application to solidification 8

2.1 Multi-scale formulation 9
2.2 Evaluation of homogenized transport properties 15
2.3 Numerical examples 19
2.3.1 Micro-scale simulation approach 20
2.3.2 Case 1. Single-scale simulation results 22
2.3.3 Case 2. Multi-scale simulation 22
2.4 Conclusion 28

III. Oxidative degradation of ceramic matrix composites 30

3.1 Computational Homogenization Approach: Micro-scale Boundary Conditions 32
3.2 Micro–Macro linking: Transferring Fluxes and Diffusivities 36
3.3 Micro–scale model 37
3.3.1 Description of flow in the porous matrix at micro–scale 38
3.4 Macro-scale model 41
3.5 Tracking of the interface using level set method and adaptive meshing 46
3.6 Computational approach and Numerical Results 47
3.6.1 Convergence study 49
3.6.2 Numerical results of the Taylor and Homogenization multi-scale model 51
3.7 Conclusion 56

IV. Multi-scale model validation with direct numerical simulations(DNS) . . . 60

4.1 Direct numerical simulation . . . 60
4.2 Computational approach and numerical results . . . 62
4.3 Conclusions . . . 65

V. A 3D multiscale model for property degradation of CMCs: Temperature and stress effects . . . 70

5.1 Matrix and vector transformation . . . 72
5.2 Computational Homogenization Approach: Micro-scale Boundary Conditions 73
5.3 Micro–scale model for elasticity . . . 78
5.4 Deformation under mechanical loading . . . 81
5.5 Micro–scale Taylor model for O_2 and CO_2 diffusion in porous matrix . . . 82
5.5.1 Diffusion properties for pore matrix . . . 84
5.6 Macro-scale model for O_2 and CO_2 diffusion in C/SiC . . . 88
5.7 Computational approach and numerical Examples . . . 91
5.8 Numerical simulation results . . . 93
5.8.1 Comparison of oxidation behavior in the presence of applied stresses 102
5.9 Conclusion . . . 103

VI. Suggestions for future research . . . 108

6.1 Modeling UHTCs . . . 109
6.2 Anisotropic diffusion . . . 109
6.3 Modeling micro- damage with molecular dynamics . . . 110
6.4 SiC oxidation - effect of moisture . . . 113

APPENDICES . . . **114**

BIBLIOGRAPHY . . . **120**

LIST OF FIGURES

Figure

2.1 *Multi-scaling procedure: Macro-scale is associated with a homogenized continuum. The macro-scale temperature (and gradient in temperature) is passed to the micro-scale as boundary conditions. Macro-scale quantities such as the thermal flux and conductivity (at the material point) are computed from the mi crostructural sub-problem through consistent averaging schemes.* 10

2.2 *Solidifying interface is tracked using an adaptive meshing strategy. This allows flux discontinuities to be accurately modeled at the micro-scale.* 13

2.3 *Schematic of the enthalpy-temperature relationship for a pure substance;* (*a*) *H is a discontinuous function of the temperature* (*b*) *Numerical treatment of discontinuity.* [*64*] 22

2.4 *Case 1 study: Finite element model for single-scale simulation uses adaptive grids with refinement in the region of the moving interface* 23

2.5 *(a) Position of the phase change interface vs. time in single-scale simulation (b) Comparison of numerical and analytic solution of temperature history at x = 1, 2, 3 and 4 cms.* 23

2.6 *Finite element mesh used in the micro level* 24

2.7 *FE models at the macro-level that are designed using different mesh sizes in order to test convergence of the multi-scale simulation result.* 25

2.8 *Mean square enthalpy errors with respect to time step size (in seconds) for the two cases. The errors are computed during the simulation from* $t = 4995sec$ *to* $t = 4995sec + \triangle t$ *(a) Case I - total number of element : 80 (a) Case II - total number of element : 1280.* 26

2.9 *The enthalpy errors (in %) on each of the three integration points for all macro-scale elements at a simulation time of t = 2500 sec. (a) Case-I: elements along the x-axis in the macroscopic FE model are ordered from left to right. (b) Case-II: the enthalpy error for all elements are shown, there are four rows of elements along y-axis (see Fig. 2.7(b)), leading to four peaks for elements located at the interface.* 26

2.10 *Comparison of predicted and analytical solution for interface positions computed using FE mesh from (a) case I (b) case II. During homogenization, the true location of the interface is not explicitly tracked in the macro-scale. The elements where the interface is located are depicted in the figure.* 27

2.11 *Comparison of predicted and analytical solution of temperature history at four different locations in the macro-scale mesh for (a) case I (b) case II* 27

3.1 *Macro-scale is associated with a homogenized continuum. The macro-scale fields and field gradients are passed to the micro-scale as boundary conditions. Macro-scale fluxes and properties (at all integration points) are computed from the underlying microstructural sub–problems using averaging schemes.* 32

3.2 *The micrographs represent experimental results of C/SiC composite oxidation in a controlled environment reported in [42] and [43]. Figure (d) shows the simulation cell: all the boundaries in the model are insulated except one side that is exposed to the external oxidizing environment. Size of the simulation cell at the macro–scale is indicated using dotted lines in (b). The simulation cell contains about 600 carbon fibers.* 50

3.3 *(a) 2D Macro-scale finite element grid (b) Micro–scale finite element grid* 51

3.4 (a) A typical sequence of mesh refinement is shown along with the associated data structure. (b) Oxidizing interface is accurately tracked using this adaptive meshing strategy. 52

3.5 *(a) Micro–scale convergence study: Carbon fiber volume at the micro–scale is tracked as a function of time using different levels of adaptive meshing. The minimum element edge length in the mesh is reported here. The volume is calculated with assuming the length in z-direction is 1mm.(b) Macro–scale convergence study: Carbon fiber volume fraction vs. time is plotted for different mesh sizes. A mesh size of $a \times b$ indicates a elements along x–axis and b elements along the y–axis* 53

3.6 *Comparison of Taylor and Homogenization approaches (a) Recessed carbon fiber volume fraction vs. time at the macro-scale. (b) Oxygen pressure distributions at various times in the macro–scale.* 54

3.7 *Carbon fiber configurations in micro at 25.1 seconds at* 950°C*; tan, white and blue colored area indicate matrix, void and carbon fiber respectively.* 55

3.8 *Comparison of carbon fiber configuration and micro–scale oxygen densities for Taylor and homogenization approaches at a simulation time of 25.1 seconds.* 58

3.9 *Spatial distributions of carbon fiber volume fraction at each integration points in macro at 0, 11.1 and 25.1 sec for (a) Taylor and (b) Homogenization model* 59

4.1 *(a) 2D Macro-scale finite element grid (b) 2D Macro-scale finite element grid for validation corresponding to DNS model scale(c) Micro–scale finite element grid (d) Direct numerical simulation finite element grid (e) Larger view of the DNS model over a region indicated by the red box* 67

4.2 *DNS convergence study: DNS models with different levels of adaptive meshing were generated and the convergence of C-fiber volume fraction were tested.* 68

4.3 *Multi-scale convergence study: Simulations with difference mesh sizes are performed in order to identify the converged macro-scale mesh size. A mesh size of $a \times b$ indicates a elements along x–axis and b elements along the y–axis.* 68

4.4 *Comparison between DNS and multi-scale simulation results: (a) Oxidized carbon fiber fraction vs. time (b) Oxygen pressure contours at simulation times of 0.1, 2.1, 6.1, 10.1 and 14.1 sec* 68

4.5 *Four selected micro–scale models on the integration points in the macro–grid are compared with the DNS model: (a) and (b) show the micro–scale configuration and oxygen partial pressure, respectively, from DNS approach. Figs (c) and (d) correspond to those from the multi-scale model. Colors blue, white, and tan denote carbon fiber, void, and matrix respectively.* 69

5.1 *(a) Ceramic matrix and carbon fiber tow are indicated with values 1 and 0 at the finite element nodes and integration points where white box is 1 and black box is 0, (b) Representative unit cell is called to identify the material at any given point in the macroscale mesh.* 71

5.2 *Tow undulation and cross-section dimensions* 71

5.3 *The carbon fiber weave can be described with representative unit cell in which biaxial carbon fiber tows are modeled and the angle ψ denotes directions of carbon fiber tow with respect to $x-y-z$ coordinate system. From the carbon fiber tow, the undulation angle, θ, shows fiber directions with respect to axes $x'-y'-z'$.* 74

5.4 *The microstructure homogenization technique: Each integration point in the macro-continuum is associated with an underlying microstructure. The microstructure reference configuration ($\mathcal{B}_{ref}$) and the mapping to the present microstructure configuration ($\mathcal{B}$) are shown in contrast with the homogenized macro-continuum. In total Lagrangian kinematics, $\boldsymbol{X} = \boldsymbol{x}_o$ and $\boldsymbol{Y} = \boldsymbol{y}_o$ are taken from the configurations at time $t = t_o$.* 75

5.5 *Kinematics coupled with damage evolution in the matrix.* 80

5.6 *Predicted (a) porosity vs. temperature curve at zero applied stress (b) porosity curves depended on stress at temperature = 873.15, 1073.15, 1173.15, and 1223.15 K* 86

5.7 *Predicted (a) Aerial porosity, (b) Permeability, (c) Surface area fraction vs. porosity, and air viscosity vs. temperature* 89

5.8 *Numerical simulation model: Geometry, initial and boundary conditions* 92

5.9 *Macro model grid convergence; Simulation shows the carbon fiber volume change at 2.5 hours and at* 800°C *as a function of number of elements used in the macro–scale mesh.* 94

5.10 *Percent weight fraction remaining: Simulation results are directly compared with thermogravimetric analysis at different temperatures.* 96

5.11 *Young's modulus in z direction is predicted at different temperatures and times using Finite element homogenization (solid line) and Taylor(broken line) approaches.* . . 97

5.12 *Oxygen pressure distributions at 600°C-1400°C* 98

5.13 *Spatial distribution of carbon fiber volume fraction at* 600°C - 900°C 100

5.14 *Spatial distribution of carbon fiber volume fraction at* 950°C - 1400°C 101

5.15 *(a) Strain vs. time; solid line shows TGA experiment results (solid lines with circle and star denote simulation results for 1 atm air and inert gas environment cases respectively). (b) Total volume losses in the composite (solid lines with circle and star denote no stress applied and stress applied respectively)* 103

6.1 *The transport parameters such as diffusivity and traction–separation laws for the micro-scale model can be calculated from molecular simulations. We performed a preliminary study to this end in Ref. [37]* 111

6.2 *Normal stress displacement response of the interface model: During tensile separation, the normal stress displacement response shows a dominant peak with associated peak stress. Peak stress is around 14 GPa.* 112

6.3 *The plastic strain locations during initiation of plasticity. The plastic strains are concentrated on grain boundary triple points or sharp corners(SiC is polycrystalline.)* 112

LIST OF TABLES

Table

2.1 Solution scheme for multiscale homogenization of solidification problems 19

2.2 List of material constants (for both solid and liquid phase) and boundary and initial conditions used for the 1D solidification problem 21

3.1 Lennard Jones potential parameters for the diffusivity between O_2 and CO_2 (k: Boltzmann constant) 40

3.2 List of material constant for the carbon fiber oxidation example. 47

3.3 Solution scheme for multiscale modeling of carbon fiber oxidation 48

3.4 Square root and linear rate constants obtained by curve fitting the simulation results 53

4.1 Solution scheme for direct numerical simulation of carbon fiber oxidation 63

5.1 Solution scheme for multi–scale modeling of C/SiC 106

5.2 Material properties employed in the multiscale model of 3D CMC oxidation 106

5.3 Porosity and surface area fraction for CMC oxidation simulations 107

LIST OF APPENDICES

Appendix

A. Volume average of heat flux at the micro-scale 115

B. Homogenized Flux Derivation Based on Hill's Macro-homogeneity Condition 117

ABSTRACT

MULTI-SCALE HOMOGENIZATION OF MOVING INTERFACE PROBLEMS WITH FLUX AND FIELD JUMPS

by
Sangmin Lee

The current choice of materials for extreme high temperature, oxidizing conditions in advanced flight vehicles is ceramic matrix composites (CMCs). Such composites are used in rocket nozzles, leading edges of the space shuttles, and thermal protection systems. CMCs used in these applications experience large thermal stresses and are subject to high temperature oxidation. These two effects progressively degrade the carbon fibers within the matrix and eventually lead to component failure. The overarching aim of this thesis is to develop a validated numerical model of carbon reinforced ceramic matrix composite oxidation. Such a model will lead to accurate prediction of CMC performance during operating conditions, development of improved safety factors for CMCs and design of CMCs with improved high temperature properties.

CMC oxidation involves interplay of mechanisms at different length scales. At the macroscopic scale, the composite is subject to external thermo-chemo–mechanical boundary conditions in the form of ambient oxygen concentrations, heat flux and applied stresses. The intact matrix is porous, leading to entry of oxygen into the matrix due to concentration and pressure gradients. The tows in the CMC contain thousands of micro-scale carbon fibers that oxidize under these conditions. Fiber oxidation leads to deterioration in the mechanical stiffness, which in turn leads to

increase in matrix damage in the presence of applied stresses. Increase in matrix damage leads to further ingress of oxygen and thus, increased oxidation. For modeling this strong stress–oxidation coupling, we need to model the interactions between two different length scales.

At the micro–scale, we model the oxidation of individual carbon fibers using a level set technique. At the macro scale, oxidation of the interwoven tow structure is captured using homogenized mass transport and stress equilibrium equations. A computational homogenization approach has been developed to link these two simulations. Computational homogenization provides an attractive avenue for computing the macroscopic response in problems with discontinuities and non-linearities. In this thesis, we present series of developments that lead to a coupled micro–macro model of CMC oxidation. Novel developments in this thesis include a new homogenization technique for problems involving moving interfaces and flux jumps that has been validated with numerical models and direct numerical simulations (DNS), calibrated models for oxygen and carbon dioxide transport through the porous matrix and heterogeneous surface chemical reactions, a constitutive damage model for relating damage measures (porosity, exposed surface area fraction, tortuosity etc.) to temperature and stress state in the matrix and a coupled micro–macro simulation that captures experimentally observed stressed–oxidation behavior of a CMC.

CHAPTER I

Introduction

1.1 Overview

Study of high temperature composites involves understanding a number of complex physical mechanisms: (i) Heat, mass transport and chemical reactions, (ii) Dynamics of moving or ablating interfaces, (iii) Coupling of oxidation and stress effects and (iv) Time varying thermo-chemo-mechanical properties. Most critically, non-linear coupling among these significantly increases the difficulty of analyzing the performance of high temperature composites. Computer modeling can help provide physical insight into various physical mechanisms at play in high temperature composites and allows design of optimized materials. In these models, the underlying length–scales may vary from the level of nano– to micro– upto centi–meters, spanning the length scale of a single carbon fiber to the level of a interwoven tow–based composite structure. Modeling of systems of this size and complexity at atomistic scale is not yet feasible. Modeling continuum systems with micro-scale resolution grids is computationally expensive, and in many cases, not feasible. In this thesis, we look into numerically inexpensive techniques for modeling continuum–scale systems while still keeping track of the physics at the micro–scale.

In the multi-scale approach, macro-scale analysis represents overall material be-

havior at the level of interest to engineers, and micro- or other smaller scale studies focus on details such as damage evolution, fiber oxidation, and interfacial chemical reactions. Macroscopic measurements become possible when the underlying physics at finer scales can be effectively communicated to macro–scale simulations through averaging schemes. Micro–scale response, on the other hand, relies on the knowledge of macroscopic boundary conditions. This kind of coupled macro–micro analysis is highly desirable as they not only resolve different length–scales, but are also capable of generating fast and accurate numerical results. Another interesting multiscale example is solidification where the nucleation, growth and interaction of crystals in the melt need to be modeled to compute the properties of the final product. Investigating the micro-scale crystal growth physics is computationally challenging; if one uses purely macro-scale models, the simulations lack accuracy due to large simplifications. Multi-scale modeling by coupling macroscopic and microscopic models allows us to take advantage of both the efficiency of the macroscopic models and the accuracy of the microscopic models.

1.2 Literature review

The multi-scale homogenization method is developed to extract effective parameters for heterogeneous media based on volume averaging [1, 66, 79]. The homogenization method initially was studied for partial differential equations (PDEs) with non-smooth coefficients [3, 4, 5, 32, 17, 62]. Independent initial efforts also were made in the 1970s' to develop homogenization theory; these studies are well summarized in [7].

In homogenization theory, effective material properties are predicted from the micro–scale model through volume averaging schemes. The term "homogeneous"

or "macroscopic" denotes the up-scaling process from micro–scale to macro–scale, within the constraint of satisfying basic conservation laws (eg. mass and energy balance). Use of representative elementary volume (REV) in [26] has made analysis of large structures on a microstructural level possible. Extensive studies of the REV have been presented in [24] and the accuracy of these approaches have been explored in [29]. At the micro-scale, bounds on homogenized quantities have also been derived analytically ([25, 24, 27, 12]).

Multi-scale analysis of general diffusion problems have been previously addressed using micro-scale effective properties obtained through either bounding relations [24, 60] or analytical closed-form expressions (reviewed in [48]) in a macro-scale model. These approaches were restricted to simple geometries with a simple material response, not yielding accurate results when discontinuous interfaces are present. More recently, numerical schemes using asymptotic homogenization approaches, based on an expansion of the unknown temperature or displacement with respect to a micro-scale length parameter, have been developed to address micro-macro heat conduction problems [2, 11, 21, 30, 50, 65]. However, the problems considered are restricted to constant conductivity and focused on steady-state heat conduction problems. Problems such as solidification and oxidation involve transient effects, and in addition, field discontinuities (flux jumps) that have not been previously addressed in a multi-scale methodology. Previous works in literature for addressing multi-scale solidification problems have involved analytical studies [77] or simple numerical computation [15] at the micro-scale followed by transfer of data to the macro-scale model. Other approaches include multi-scale algorithms driven by microscopic numerical solution data, e.g. database look-up or regression fit [35, 75] and sub-grid modeling [56] approaches. A recent article in this journal summarizes various techniques proposed

in the solid and fluid mechanics community for addressing multi-scale problems in general [20].

In [77], the macroscopic transport equations are derived using volume averaging technique and closed by supplementary relations, which are obtained from the micro-scale. In [77], there is no numerical computation performed at the micro-scale. In [35, 75], micro-scale computations are used to obtain data for regression fit of a predictive equation, which is further used for macro-scale computations. Since micro- and macro- scale equations are decoupled in database approaches, they do not model loading history dependence and non-linearity in micro-scale data. In [15, 56], a sub-grid based model was suggested wherein a micro-scale model passes volume fraction information to a macro-scale model. However, in these studies, no attempt is made to prove micro-macro thermodynamic balance laws when using the proposed scale transition. The emphasis in this paper, is to provide a generalized macro-micro homogenized model of diffusion problems with flux discontinuities where scale transitions are derived from balance laws.

Computational homogenization provides an attractive avenue for computing the macroscopic response in problems with discontinuities and non-linearities in the microstructural behavior. Application of such approaches for mechanical deformation has been well studied previously [67, 45, 34, 70] and recently extended to thermo-mechanical problems [52]. In this approach, a representative volume element (RVE) is defined at the micro-scale and boundary conditions are defined on the RVE in terms of macroscopic quantities. The data from micro-scale simulations are used to extract quantities for the macroscopic simulation via consistent averaging schemes. Homogenization approaches remain valid as long as the length scale over which the macroscopic field variables vary remains much larger than the microscopic length-

scale. Recently, such a scheme was developed for thermal conduction problems [51] using a well-behaved micro-scale model without flux discontinuities or moving interfaces.

Problems involving transient effects and interface phenomena have not been previously addressed in a multi-scale methodology. Computational homogenization provides an attractive avenue for computing the macroscopic response in problems with discontinuities and non-linearities. Computational homogenization is a multi-scale analysis approach in which computations are concurrently performed at two different length-scales. The macro-scale is associated with the component being modeled (10^{-3} to 10^{+1} m) and the meso-scale is characterized by the underlying composite microstructure (10^{-6} to 10^{-3} m). The principle of scale separation states that the characteristic length scale over which the macroscopic field variables vary, should be much larger than the size of the microscopic volume considered. In other words, macroscopic quantities are nearly constant at the level of a RVE. A representative volume element (RVE) is defined at the micro-scale and boundary conditions are defined on the RVE in terms of macroscopic quantities. Applications of such approaches for thermo-mechanical deformation have been well studied previously [67, 45, 70].

Recently, Belytschko and co–workers[9] have modeled material discontinuities (cracks) across length–scales in solids using this technique. Complementing this development, we focus on problems involving field and flux discontinuities. Flux discontinuities arise in several problems, the most well–studied of which is fluid solidification. In solidification problems, a flux jump (manifested as latent heat) occurs at the evolving solidification front while the overall temperature field itself is continuous in the domain. Recently, the homogenization scheme was extended for addressing such problems in our recent work [36]. Oxidation problem addressed in this work not

only involves a flux discontinuity but also additionally involves a field discontinuity in the form of a jump in oxygen density field across the oxidizing interface. In this thesis, we develop a fully coupled multi–scale homogenization approach for problems involving both field and flux discontinuities.

We apply this technique for modeling oxidative degradation of a C/SiC composite. Oxygen transport phenomena in C/SiC composites is primarily through an interconnected void network in the matrix formed due to thermal expansion mismatch between carbon fibers and the matrix during processing. At the micro-scale, fine carbon fibers in within tows interact with oxygen and degrade at moderate to high temperatures. Initial models for studying oxidation of C/SiC composites at micro-scales have assumed a steady state diffusion through the matrix [16, 22]. While these techniques model the micro-scale, techniques for homogenizing the results for use in global analysis was not developed. In [69], a continuum level theory for modeling composite oxidation was developed. The approach models the composite as a homogeneous mixture of matrix, carbon fiber and voids. While continuum models are practical approaches for predicting the behavior of C/SiC composites, they do not model the inherent heterogeneities involved in fiber oxidation. In this thesis, a non-linear coupled macro-micro finite element model is presented for addressing carbon fiber oxidation problems. The micro-scale model incorporates the physics associated with oxidation including moving interfaces and flux discontinuities, while the macro-scale model needs to only model diffusion using continuous (homogenized) fields. Two multiscaling procedures were outlined in this work: one based on assumed solution in the micro–scale (Taylor model) and another based finite element solution of the micro–scale problem (Homogenization approach). A nested finite element solution scheme is implemented into a FE framework and the macro-

scopic diffusivity is derived in a consistent manner for these two approaches. The results from these two multi–scaling approaches were compared to direct numerical simulations for model validation. In both models, the influence of microstructural evolution (e.g. carbon fiber oxidation) on the competition between macroscopic oxygen and carbon dioxide transport in the macro–scale can be introduced and treated effectively. Taylor model is computationally efficient but provides an upper bound response and predicts faster oxygen transport within the tow compared to the FE homogenization approach. In the final chapter, the multiscale approach has been combined with mechanical field effects for modeling high temperature oxidation of composites. The multiscale stressed oxidation model has allowed understanding of interesting mechanisms such as interaction of porosity evolution with carbon fiber oxidation ('stress–oxidation coupling') that cannot be explained without incorporating microstructural details.

CHAPTER II

Multi-scale homogenization with flux jumps - Application to solidification

[1]

In order to lay the groundwork for our multiscaling scheme, we present the homogenization method as applied to a fluid solidification problem. Fluid solidification has been well studied in the past and analytical models are available that allow us to validate the multiscaling procedure. Fluid solidification, like composite oxidation, includes discontinuities in flux (due to latent heat of solidification) and has moving interfaces. In this chapter, a two-scale computational homogenization procedure for addressing this problem is discussed. We provide consistent macro-micro transition and averaging rules based on Hill's macro-homogeneity condition. The overall macro-scale behavior is analyzed with solidification at the micro-scale modeled using an enthalpy formulation. The method is versatile in the sense that two different models can be employed at the macro- and micro- scales. The micro-scale model can incorporate all the physics associated with solidification including moving interfaces and flux discontinuities, while the macro-scale model needs to only model thermal conduction using continuous (homogenized) fields. The convergence behavior of the tightly coupled macro-micro finite element scheme with respect to decreasing element

[1] Reproduced from [36], S Lee and V Sundararaghavan, Multiscale modeling of moving interface problems with flux jumps: Application to solidification, Computational Mechanics, vol. 44(3), pp. 297-307, 2009.

size is analyzed by comparing with a known analytical solution of the Stefan problem. The chapter is arranged as follows. In section 2.1, the multi-scale formulation is introduced, followed by description of the micro- and macro- scale problems and the computational scheme in section 2.2. In section 2.3, we demonstrate the potential of the approach by comparing the results from this approach with a well-known analytical solution.

2.1 Multi-scale formulation

We consider a problem of heat conduction in an incompressible fluid, where parts of the fluid are frozen, while other parts are in a liquid state. The interface between the frozen and molten region is an unknown moving internal boundary. At the micro-scale, material 1 (in liquid state) occupies the domain V^+ and material 2 (in solid state) occupies the domain (V^-), where V^+ and V^- are open subsets of V. At the interface S^I, material 2 solidifies further and advances into V^+. The interface S^I moves in the direction $-\boldsymbol{n}^I$ with speed V_n, where $\boldsymbol{n}^I$ is the outward normal of V^+) at the interface.

Macro-micro linking is achieved by decomposing the micro-scale temperature field (T)into a sum of macroscopic field and a fluctuation field ($\tilde{T}$) as:

$$T = T_{ref} + \overline{\nabla T} \cdot \boldsymbol{x} + \tilde{T} \tag{2.1}$$

Here, $\boldsymbol{x}$ is the coordinate of a point on the micro-scale relative to a reference point on the bottom left corner of the microstructure where temperature is T_{ref} (as shown in Fig. 2.1). In general, we denote a macroscopic counterpart of a microscopic field quantity (say, χ) as $\overline{\chi}$. In the above equation, gradient in temperature at macroscopic material point is denoted as $\overline{\nabla T}$ ($= \nabla_{macro}\bar{T}$). Our basic homogenization assumption is that $\overline{\nabla T}$ can be computed from the temperature at the external boundary (S) of

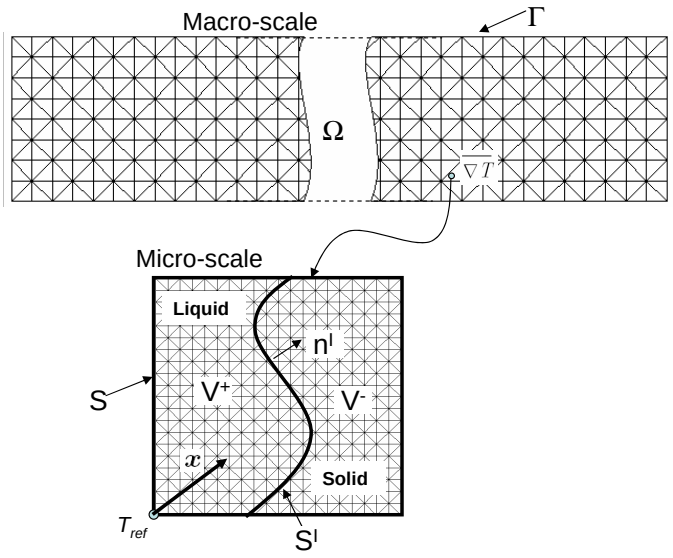

Figure 2.1: *Multi-scaling procedure: Macro-scale is associated with a homogenized continuum. The macro-scale temperature (and gradient in temperature) is passed to the micro-scale as boundary conditions. Macro-scale quantities such as the thermal flux and conductivity (at the material point) are computed from the mi crostructural sub-problem through consistent averaging schemes.*

the microstructure with outward normal $\boldsymbol{n}$ as:

$$\overline{\nabla T} = \frac{1}{V}\int_S T\boldsymbol{n}dS \tag{2.2}$$

Using the decomposition of the micro-scale temperature field, it can be shown that:

$$\frac{1}{V}\int_V \nabla T dV = \overline{\nabla T} + \frac{1}{V}\int_V \nabla \tilde{T} dV \tag{2.3}$$

We employ the generalized divergence theorem of the form $\int_V \nabla\chi dV = \int_S \chi\boldsymbol{n}dS + \int_{S^I}[|\chi|]\boldsymbol{n}^I dS^I$ in the above equation (where, $[|\chi|]$ denotes the jump in the field quantity across the evolving interface (S^I) with normal n^I) to obtain the following relationship:

$$\frac{1}{V}\int_S T\boldsymbol{n}dS = \overline{\nabla T} + \frac{1}{V}\int_S \tilde{T}\boldsymbol{n}dS + \frac{1}{V}\int_{S^I}([|\tilde{T}|] - [|T|])\boldsymbol{n}^I dS^I \tag{2.4}$$

The jump in a field quantity, say T, across such an interface is computed as $[|T|] = T_+ - T_-$. Here, T_+ and T_- refer to the quantity in domain V^+ and V^-,

respectively, close to a point on the interface (as shown in Fig. 2.2). We aim to build boundary conditions at the micro-scale that satisfies Eq. 2.4. Assumption of $\tilde{T} = 0$ at all points in the microstructure leads to rule of mixtures (or Taylor model in deformation problems). This is not a valid assumption for solidification problems as the solid-melt interface is at the melting point, whereas in a Taylor model, temperature at all points are constrained as $T = T_{ref} + \overline{\nabla T} \cdot \boldsymbol{x}$. In addition, Taylor model solution does not satisfy micro-scale thermal equilibrium. Due to the strong constraint imposed on micro-scale temperatures, it can be shown that the Taylor model produces an upper-bound result for conductivities calculated. Two other boundary conditions are applicable to the solidification problem that can allow satisfaction of equilibrium constraint as well as interface temperature constraint. The first is an essential boundary condition on the surface of the microstructure and the other is a periodic boundary condition (refer [51]) on temperatures. In this chapter, we restrict ourselves to the essential boundary conditions given below:

$$\tilde{T} = 0 \text{ on } S \tag{2.5}$$

$$([|\tilde{T}|] - [|T|]) = 0 \text{ on } S^I \tag{2.6}$$

In this case, temperature at the boundaries of the microstructure is derived from the macro-scale temperature field and temperature gradient as $T = T_{ref} + \overline{\nabla T} \cdot \boldsymbol{x}$. The interface temperature jump constraint (Eq. 2.6) is trivially satisfied (by computing jump from Eq. 2.1 and noting that macroscopic fields are assumed continuous). In solidification problems, temperature fields are continuous ($[|T|] = 0$) and an additional boundary condition is applied that enforces the interface to be at the melting point (or calculated using Gibbs-Thomson relation for dendritic growth simulations (eg. [75]).

Solidification is modeled at the micro-scale using the convection-diffusion equation:

$$\frac{\partial(\rho c T)}{\partial t} + \nabla \cdot \boldsymbol{q} = -\nabla \cdot (\rho c T \boldsymbol{v}) \tag{2.7}$$

Where, $\boldsymbol{q}$ represents the heat flux ($\boldsymbol{q} = -k\nabla T$, where k is the thermal conductivity), ρ denotes the density, c is the heat capacity and $\boldsymbol{v}$ represents the velocity field. For simplicity, convective effects within the fluid are ignored and the velocity field is assumed to be non-zero only on the evolving solidification front. Since the microscopic length scale is considered to be much smaller than the scale of variation of the macroscopic temperature field, the micro-scale can be assumed to be at steady state at any instant of the macroscopic (transient) evaluation [51]. The microscopic diffusion equation is then given as:

$$\nabla \cdot \boldsymbol{q} = -\nabla \cdot (\rho c T \boldsymbol{v}) \tag{2.8}$$

Consider the space of weighting functions, $\mathcal{V}$, given by

$$\mathcal{V} = \{\phi : \phi \in H^1 \text{ over } V, \phi = 0 \text{ on } S\} \tag{2.9}$$

and the space of trial functions, $\mathcal{L}$, given by

$$\mathcal{L} = \{T : T \in H^1 \text{ over } V^+ \cup V^-, T \text{ given on } S \cup S^I\} \tag{2.10}$$

Weak form of the above equation can be simplified as follows (where ϕ is the weighting function that is assumed to be continuous across the microstructure):

$$(\nabla\phi, \boldsymbol{q})_V = (v_n[|\rho c T|], \phi)_{S^I} + ([|q_n|], \phi)_{S^I} \tag{2.11}$$

In the above equation, the symbol $(.,.)$ represents the Euclidean inner product over the domain given by the subscript. To obtain the above mentioned weak form,

we have assumed that the velocity at all points (aside from the points on the interface) are small (ie. $\boldsymbol{v} = 0$ on $V^+ \cup V^-$). As described previously, the micro-scale model includes both heat capacity jump ($[|\rho c|]$) and flux jump ($[|\boldsymbol{q}|]$) in the normal direction across the solidifying interface. The velocity of the solid-liquid interface is governed by the heat flux jump through the classical Stefan equation:

$$([|q_n|] + v_n[|\rho c|]T) = 0 \tag{2.12}$$

$$\text{where, } T[|\rho c|] = L \text{ or } [|q_n|] = -v_n L \tag{2.13}$$

where, L is the latent heat of phase transformation per unit volume.

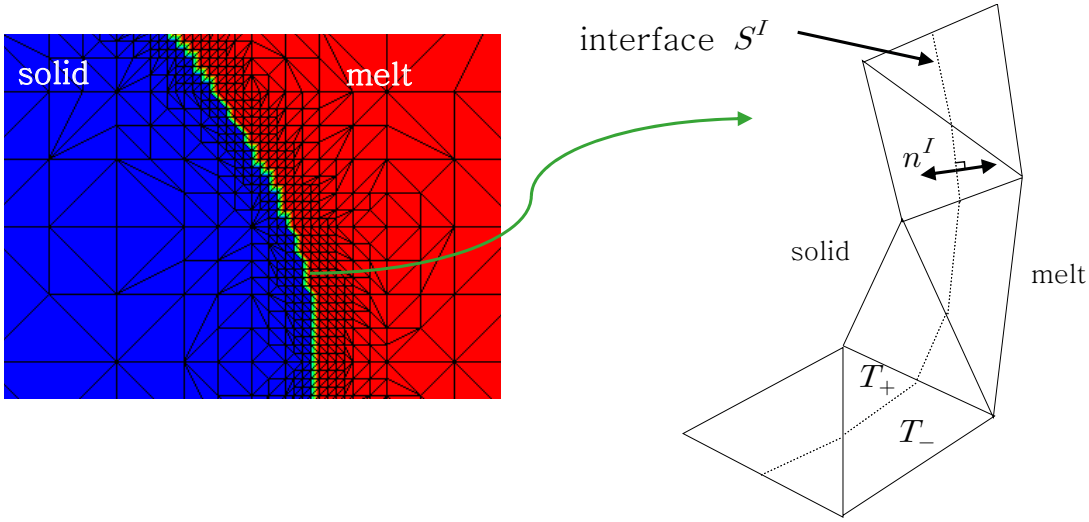

Figure 2.2: *Solidifying interface is tracked using an adaptive meshing strategy. This allows flux discontinuities to be accurately modeled at the micro-scale.*

Based on Stefan equation, it can be proved that the integral of normal heat flux over the microstructure surface goes to zero as follows:

$$\begin{aligned}\int_S q_n dS = \int_S \boldsymbol{q}\cdot\boldsymbol{n} dS &= \int_V \nabla\cdot\boldsymbol{q} dV - \int_{S^I}[|q_n|]dS^I \\ &= -\int_V \nabla\cdot(\rho c T\boldsymbol{v})dV - \int_{S^I}[|q_n|]dS^I \\ &= -\int_{S^I}(v_n[|\rho c|]T + [|q_n|])dS^I = 0\end{aligned} \tag{2.14}$$

The above relation is subsequently used for homogenization of the micro-scale flux. In particular, we are interested in obtaining a macroscopic flux that satisfies Hill's macro-homogeneity condition (which relates the macroscopic flux ($\bar{\boldsymbol{q}}$) with its microstructural counterpart ($\boldsymbol{q}$ [49]) as follows:

$$\overline{\nabla T} \cdot \overline{\boldsymbol{q}} = \overline{\nabla T \cdot \boldsymbol{q}} \tag{2.15}$$

Application of the governing equation (Eq. 2.8) changes the macro-homogeneity condition to the following form:

$$\begin{aligned} \overline{\nabla T} \cdot \overline{\boldsymbol{q}} = \overline{\nabla T \cdot \boldsymbol{q}} = \frac{1}{V}\int_V (\nabla \cdot (T\boldsymbol{q}) - T\nabla \cdot \boldsymbol{q}) dV \\ = \frac{1}{V}\int_S T q_n dS + \frac{1}{V}\int_{S^I} [|T q_n|] dS^I + \frac{1}{V}\int_V T\nabla \cdot (\rho c T \boldsymbol{v}) dV \end{aligned} \tag{2.16}$$

We can reduce the first term in the above equation using the definition of micro-scale temperature (Eq. 2.1) and the homogeneous boundary conditions as:

$$\begin{aligned} \frac{1}{V}\int_S T q_n dS = \frac{1}{V}\int_S [T_{ref} + \overline{\nabla T} \cdot \boldsymbol{x}] q_n dS \\ = \overline{\nabla T} \cdot \frac{1}{V}\int_S \boldsymbol{x} q_n dS \ (\text{ using } \int_S q_n dS = 0) \end{aligned} \tag{2.17}$$

The second and third terms in Eq. (2.16) are again reduced using the generalized divergence theorem as:

$$\begin{aligned} \frac{1}{V}\int_{S^I} [|T q_n|] dS^I + \frac{1}{V}\int_V T\nabla \cdot (\rho c T \boldsymbol{v}) dV \\ = \frac{1}{V}\int_{S^I} [|T q_n|] dS^I + \frac{1}{V}\int_V \nabla \cdot (\rho c T^2 \boldsymbol{v}) dV - \frac{1}{V}\int_V \nabla T \cdot (\rho c T \boldsymbol{v}) dV \\ = \frac{1}{V}\int_{S^I} T[|q_n|] dS^I + \frac{1}{V}\int_{S^I} T^2 [|\rho c|] v_n dS^I = 0 \end{aligned} \tag{2.18}$$

In the above derivation, we use Stefan equation and the fact that the particle velocity is zero at all points in the material except the interface. Combining equations (2.16,2.17,2.18), the macroscopic flux is obtained as:

$$\overline{\boldsymbol{q}} = \frac{1}{V}\int_S \boldsymbol{x} q_n dS \tag{2.19}$$

The above equation allows macroscopic heat flux to be computed from the normal flux at the boundaries of the microstructure similar to Eq. 2.2. Using Stefan equation, we can also show that the macroscopic heat flux thus computed corresponds to the volume averaged heat flux at the micro-scale (see appendix A).

2.2 Evaluation of homogenized transport properties

The macroscopic diffusion equation is defined on a uniformly meshed domain (Ω) on which solidification occurs. Boundaries of the macro-scale domain is denoted as Γ. Solidification is explicitly modeled at the micro-scale, while only heat conduction is modeled at the macro-scale using homogenized quantities as follows:

$$\frac{\partial \bar{H}}{\partial t} = -\nabla \cdot \bar{\boldsymbol{q}}, T(\Gamma, t > 0) = \widehat{T}, T(\Omega, t = 0) = T_0 \tag{2.20}$$

where, the macroscopic (homogenized) enthalpy ($\bar{H}$) is defined using microscopic volume averaged heat capacity ($\overline{\rho c}$) as follows:

$$\bar{H} = \overline{\rho c T + L\rho f} = \overline{\rho c}\bar{T} + L\overline{\rho f} \tag{2.21}$$

Here, f is the volume fraction of liquid in the micro-scale, L is the latent heat of solidification defined per unit mass. In the above equation, the enthalpy is defined using microscopic volume averaged heat capacity ($\overline{\rho c}$). This definition is consistent with the condition that stored energy at macro-scale is same as the average micro-scale stored energy [51]. The temperature boundary conditions at the micro-scale

is completely defined once T_{ref} for the next time step is computed using Eq. 2.21 and Eq. 2.1 at the end of each time step of the simulation. Due to the use of an explicit scheme to calculate T_{ref}, smaller time steps at the macro-scale allow better satisfaction of balance of stored energy. In the numerical examples, we report the error between the macro- and micro- stored enthalpy at various material points to show that the balance of stored energy condition (Eq. 2.21) is indeed satisfied during homogenization.

To solve the non-linear macroscopic equation (Eq. 2.20), Galerkin finite element method is adopted and the weak form is solved in an incremental-iterative manner using the Newton-Raphson method. The $(\lambda+1)^{th}$ Newton-Raphson step at time $(t+1)$ involves solution of the system $\boldsymbol{K}\{\delta\bar{H}^{\lambda+1,t+1}\} = \boldsymbol{f}$, where the unknown vector in the above system is the increment in the enthalpy ($\delta\bar{H}^{\lambda+1,t+1}$). To understand the micro-scale quantities that are needed to create the system of equations, the Jacobian matrix and force vector for a finite element e with shape functions N_i occupying a volume Ω^e is expanded below:

$$\begin{aligned} K^e_{ij} &= \frac{1}{\Delta t}\int_{\Omega^e} N_i N_j d\Omega - \int_{\Omega^e} \bar{\boldsymbol{\kappa}}^{\lambda,t+1}\nabla N_i \cdot \nabla N_j d\Omega \\ f^e_j &= \int_{\Omega^e} \bar{\boldsymbol{q}}^{\lambda,t+1}\cdot\nabla N_j d\Omega - \frac{1}{\Delta t}\int_{\Omega^e}(\bar{H}^{\lambda,t+1} - \bar{H}^t)N_j d\Omega \end{aligned} \tag{2.22}$$

From the above equations, it is seen that to solve the macro-scale equations, one requires the homogenized conductivity $\bar{\boldsymbol{\kappa}}$ to be defined at each integration point in the macro-scale as follows:

$$\delta\bar{\boldsymbol{q}}^{\lambda,t+1} = \bar{\boldsymbol{\kappa}}^{\lambda,t+1}\delta(\overline{\nabla H}) \tag{2.23}$$

The homogenized conductivity can either be obtained using perturbation analysis [44] or by directly manipulating the converged Jacobian and residual matrices of the micro-scale problem[51]. In the former approach, each component of the macroscopic

temperature gradient is independently perturbed by a small amount ϵ which affects the boundary conditions at the micro-scale through Eq. 2.1. The micro-scale problem is solved again using the perturbed boundary conditions and the resulting perturbation in homogenized flux is used to compute the homogenized conductivity. This involves solution of N different micro-scale problems during each Newton-Raphson iteration at the macro-scale, where N is the dimensionality of the macro-scale problem. Note that numerical approximation of the homogenized conductivity does not change the physical result in any way, only the speed of iteration process changes.

In this work, we follow the approach of [51] to obtain homogenized conductivity by direct manipulation of the converged Jacobian and residual matrices of the micro-scale problem. The steps to compute the homogenized conductivity using the approach is as follows. Macroscopic flux is first written using the vector of normal fluxes on the external nodes of the microstructure ($\{q_n^{ext}\}$) using finite element matrix representation as follows:

$$\overline{\boldsymbol{q}} = \frac{1}{V}\int_S \boldsymbol{x} q_n dS = \boldsymbol{L}\{q_n^{ext}\} \tag{2.24}$$

To compute the homogenized conductivity, one needs to compute sensitivity of $\{q_n^{ext}\}$ to perturbations in the macroscopic enthalpy gradient $\delta(\overline{\nabla H})$ as:

$$\delta\overline{\boldsymbol{q}} = \boldsymbol{L}\{\delta q_n^{ext}\} = \bar{\boldsymbol{\kappa}}\delta(\overline{\nabla H}) \tag{2.25}$$

To obtain the homogenized conductivity, the converged finite element solution from the Newton-Raphson iterations at the micro-scale is employed as follows:

$$\begin{bmatrix} \boldsymbol{K}_{ee} & \boldsymbol{K}_{ei} \\ \boldsymbol{K}_{ie} & \boldsymbol{K}_{ii} \end{bmatrix} \begin{bmatrix} \delta\boldsymbol{H}^e \\ \delta\boldsymbol{H}^i \end{bmatrix} = \begin{bmatrix} 0 \\ 0 \end{bmatrix}$$

In the above equation, the assembled matrix ($\boldsymbol{K}$) on the left hand side is the Jacobian matrix of the Newton-Raphson iteration. The residual on the right hand side goes to zero since the micro-scale solution has converged. The assembled matrix ($\boldsymbol{K}$) is arranged such that the vectors $\delta\boldsymbol{H}^e$ and $\delta\boldsymbol{H}^i$ contain the enthalpies on the external and internal nodes of the microstructure, respectively. Sensitivity of enthalpy on external nodes of the micro-scale mesh to the perturbation in the imposed macroscopic enthalpy gradient can be written using matrix $\boldsymbol{G}$ (computed from the boundary condition on the temperatures on the external nodes (Eq. 2.1)) as follows:

$$\{\delta\boldsymbol{H}^e\} = \boldsymbol{G}\{\delta\overline{\nabla H}\} \tag{2.26}$$

Substituting the above relation into the converged matrix equation at the micro-scale and taking the known quantities to the right hand side, we obtain the equation:

$$\begin{bmatrix} \boldsymbol{K}_{ee} & \boldsymbol{K}_{ei} \\ \\ \boldsymbol{K}_{ie} & \boldsymbol{K}_{ii} \end{bmatrix} \begin{bmatrix} 0 \\ \\ \delta\boldsymbol{H}^i \end{bmatrix} = \begin{bmatrix} -\boldsymbol{K}_{ee}\boldsymbol{G}\delta\overline{\nabla H} \\ \\ -\boldsymbol{K}_{ie}\boldsymbol{G}\delta\overline{\nabla H} \end{bmatrix}$$

The vector on the right hand side provides the sensitivity of microscopic flux to the macroscopic enthalpy gradient, which leads to the homogenized conductivity, $\bar{\boldsymbol{\kappa}}$ as follows:

$$\begin{aligned} \delta q_n^{ext} &= -\boldsymbol{K}_{ee}\boldsymbol{G}\delta\overline{\nabla H} \\ \bar{\boldsymbol{\kappa}} &= -\boldsymbol{L}\boldsymbol{K}_{ee}\boldsymbol{G} \end{aligned} \tag{2.27}$$

The overall solution scheme is shown in Table. 1. To aid in speeding up the solution process for the multi-scale problem, the algorithm was parallelized using MPI. The macro-scale domain was decomposed and elements in each domain distributed to different processors. The underlying micro-scale problems were solved in

serial within each processor. The simulator was developed using object oriented programming and was dynamically linked to the parallel toolbox PetSc [8] for parallel assembly and solution of linear systems. For solution of linear systems, a GMRES solver along with block Jacobi and ILU preconditioning was employed.

Table 2.1: Solution scheme for multiscale homogenization of solidification problems

(1) Initialize macro-scale model and assign a microstructure to every integration point. Initially, all the underlying microstructures are in liquid state with known conductivity.

(2) Apply time increment Δt to the macro-scale problem.

(3) Iteration step:

- (3.1) Assemble the macroscopic stiffness matrix.
- (3.2) Solve the macroscopic system and compute temperature and the temperature gradient at each integration point.
- (3.3) Loop over all integration points
  - (a) Transfer boundary conditions to micro-scale problem using Eqs. 2.1,2.5.
  - (b) Assemble and solve the micro-scale problem.
  - (c) Calculate the macro-flux (Eq. 2.19) and the macro-conductivity (Eq. 2.27) using the micro-scale solution and store the data.
- (3.4) Assemble the macroscopic residual vector.

(4) Check convergence, if not converged go to step 3, otherwise go to step 2.

2.3 Numerical examples

In order to validate the multi-scale simulation procedure, a well-studied one-dimensional solidification problem is employed. In this simulation, one end of the simulation domain is fixed to a temperature less than melting point. The other end is assumed to at infinity and fixed to a temperature larger than the melting point so that the solid-liquid interface moves between these two ends. The analytic solution for the position of the interface ($X(t)$) at various times can be expressed as the following [61]:

$$X(t) = 2\lambda\sqrt{\alpha_s t} \tag{2.28}$$

In the above expression, $\alpha = (\frac{k}{\rho c})$ where k is the thermal conductivity and the subscripts s and l are used when using properties of solid and liquid phase respectively. Constant λ is equal to 0.2037 for this particular problem [13]. The analytical solution for the temperature history can be expressed as [61] (where erf is the error function and $T_m = 0°\text{C}$ is the melting point for the fluid):

$$T = \begin{cases} T(0,t) + \frac{T_m - T(0,t)}{erf(\lambda)} erf\left(\frac{x}{2\sqrt{\alpha_s t}}\right) & x < X(t) \\ T_m & x = X(t) \\ T(\infty,t) + \frac{T_m - T(\infty,t)}{1 - erf\left(\lambda\sqrt{\frac{\alpha_s}{\alpha_l}}\right)}(1 - erf\left(\frac{x}{2\sqrt{\alpha_l t}}\right)) & x > X(t) \end{cases} \tag{2.29}$$

In the numerical simulations, the problem is modeled in a two-dimensional domain discretized using three-noded triangular elements at the macro- and micro- scales. A sufficiently large FE model size is chosen to approximate the infinite boundary. The material properties, boundary conditions, and initial conditions for the material used in this simulation are provided in the Table 2.

2.3.1 Micro-scale simulation approach

The problem is addressed using a single scale model as well as a multi-scale model to validate the results. Solution of micro-scale problem presents computational difficulties due to the presence of interface conditions in the form of an essential boundary condition and specified heat flux jump. To overcome these issues, we have employed

Table 2.2: List of material constants (for both solid and liquid phase) and boundary and initial conditions used for the 1D solidification problem

Material constant	Value
$L\,(kJ/kg)$	100000
$\rho\,(kg/m^3)$	1
$c\,(kJ/kgK)$	2500
$k\,(W/mK)$	2
BC's $\begin{cases} T(x=0,y,t) = -4°\text{C} \\ T(x=\infty,y,t) = 2°\text{C} \end{cases}$	IC's $\begin{cases} T(x=0,y,0) = -4°\text{C} \\ T(x>0,y,0) = 2°\text{C} \end{cases}$

the now well-established enthalpy formulation [64] to solve the micro-scale problem. Using the enthalpy formulation, it is possible to formulate a solution procedure where the flux jump condition is automatically satisfied without explicitly tracking the internal boundary. The governing equation is posed using enthalpy as the unknown variable and the equations are solved using a standard Galerkin FE formulation. Enthalpy is a discontinuous function at the interface as latent heat is added during phase change from solid to liquid state. In the enthalpy approach, the discontinuity of enthalpy at the interface is treated by allowing it to be continuous in a small region with $T_s = T_m - \epsilon$ and $T_l = T_m + \epsilon$ around the interface as shown in Fig. 2.3. Because of this numerical treatment, the desired interface behavior can be achieved without divergence and singularity issues. In particular, the following enthalpy function with respect to temperature has been used in this work (with $\epsilon = 0.1K$):

$$H = \begin{cases} \rho c T & T < T_s \\ \rho c T_s + \rho \left(\frac{2c\epsilon + L}{2\epsilon}\right)(T - T_s) & T_s \leq T < T_l \\ \rho c T + \rho L & T > T_l \end{cases} \tag{2.30}$$

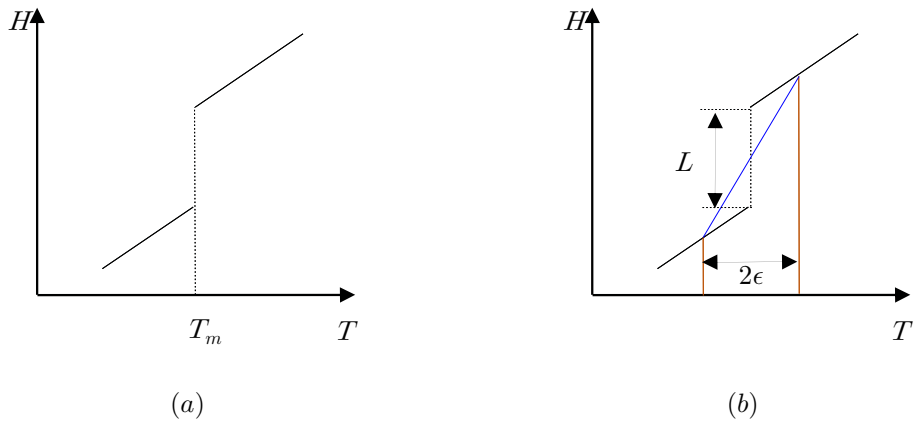

Figure 2.3: *Schematic of the enthalpy-temperature relationship for a pure substance;* (*a*) *H is a discontinuous function of the temperature* (*b*) *Numerical treatment of discontinuity.* [*64*]

2.3.2 Case 1. Single-scale simulation results

We first compare simulation results (based on the enthalpy formulation) to the analytical solution. Please note that the simulation reported in this case is a *transient* simulation based on Eq. 2.7. Adaptive meshing is employed with grids continuously refined in the region of the interface during the simulation in order to accurately track the solidification front as shown in Fig. 2.4. The interface velocities (solidification front) and the temperature distribution is well predicted by the model and compares favorably with the analytic solution. Comparison of numerical results with the analytical solution of the solidification front position and temperature time history at various locations is shown in Fig. 2.5(a) and Fig. 2.5(b) respectively.

2.3.3 Case 2. Multi-scale simulation

In the multi-scale simulation reported here, the micro-scale is considered to be in steady state as given in Eq. 2.8 while the time-dependence is incorporated at the macro-scale using Eq. 2.20. The finite element model at the microscopic scale for the multi-scale simulation is shown in Fig. 2.6.

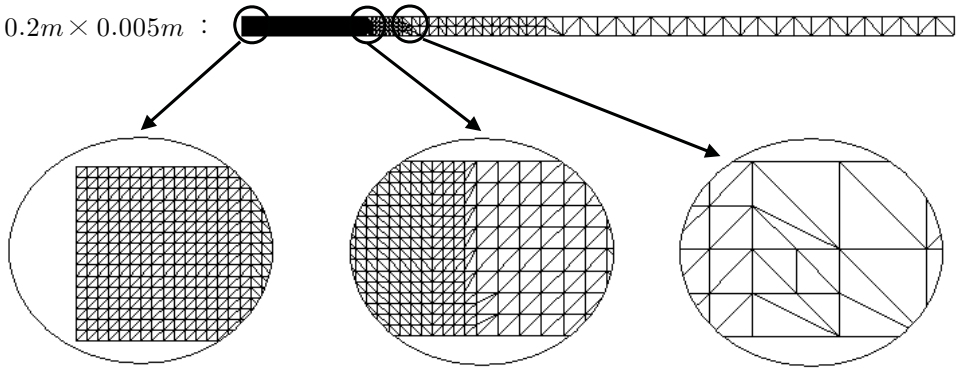

Figure 2.4: *Case 1 study: Finite element model for single-scale simulation uses adaptive grids with refinement in the region of the moving interface*

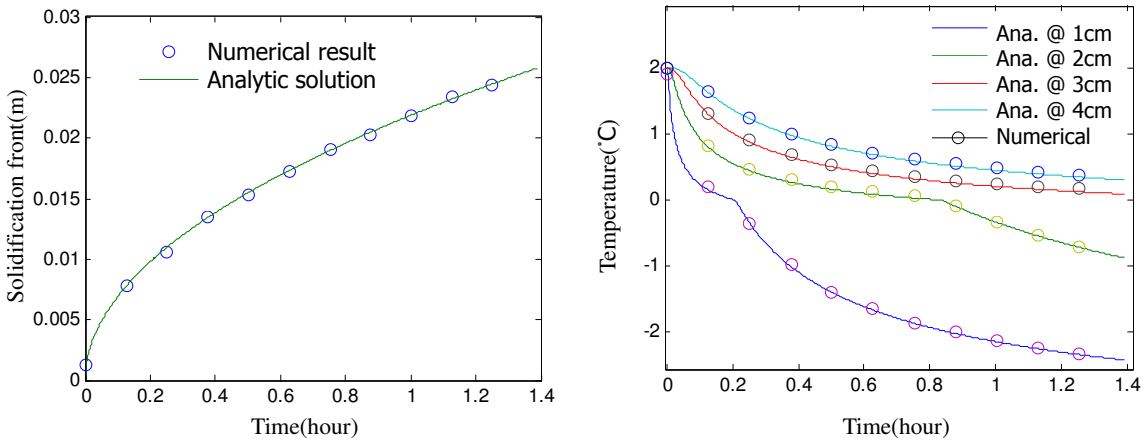

(a) (b)

Figure 2.5: *(a) Position of the phase change interface vs. time in single-scale simulation (b) Comparison of numerical and analytic solution of temperature history at x = 1, 2, 3 and 4 cms.*

The ability of the multi-scale model to capture the solidification front accurately is dictated by the mesh density at the macro-scale. Two meshes with increasing mesh density were used to test the convergence behavior of the multi-scale model. These meshes are depicted in Fig. 2.7.

Due to the tightly coupled nature of the macro- and micro- scale problems, numerical convergence needs to be established through careful control of mesh size and time steps. In all cases, the time steps were carefully controlled so that difference in enthalpy at the macro- and micro- scales at various integration points are minimized.

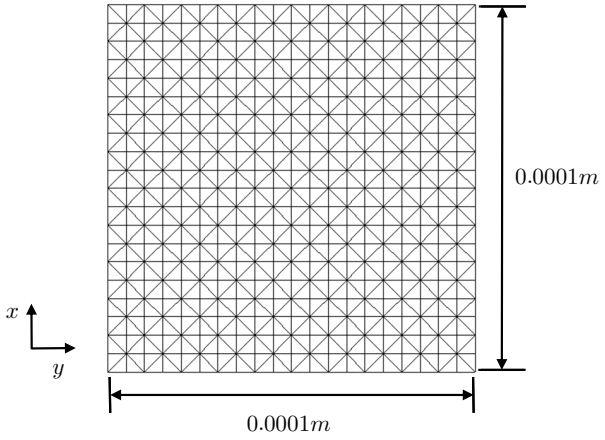

Figure 2.6: *Finite element mesh used in the micro level*

As discussed in Sec. 2.2, energy balance dictates the choice of time steps used in the multi-scale problem. In order to ascertain the time step size needed to solve the multi-scale problem, the enthalpy difference between macro- and micro- at the integration points is computed as below:

$$\text{Mean square error} = \sqrt{\frac{\sum \left(\frac{H_M^i - \bar{H}^i}{H_M^i}\right)^2}{N}} \tag{2.31}$$

In the above equation, H_M denotes the macro-scale enthalpy, $\bar{H} = \frac{1}{V}\int_V H dV$ is the volume average of enthalpy (H) at the micro-scale and N denotes number of integration points in macro-scale FE model. As shown in the Fig. 2.8(a), the error increases rapidly as time step, $\triangle t$ increases beyond 8 seconds for Case I. If a time step larger than 8 seconds is employed, the simulation rapidly diverges during the non-linear iterations. It is seen that the choice of time step is closely related to the mesh density used at the macro-scale. The overall error in enthalpy remains the same as the time step is reduced below eight seconds. The percentage error at each integration point calculated as $100(\frac{H_M^i - \bar{H}^i}{H_M^i})$ is plotted in Fig. 2.9(a,b) for the coarse and fine macro-scale mesh, respectively. The enthalpy difference between micro- and macro-scales are primarily observed at elements that involve the evolving interface

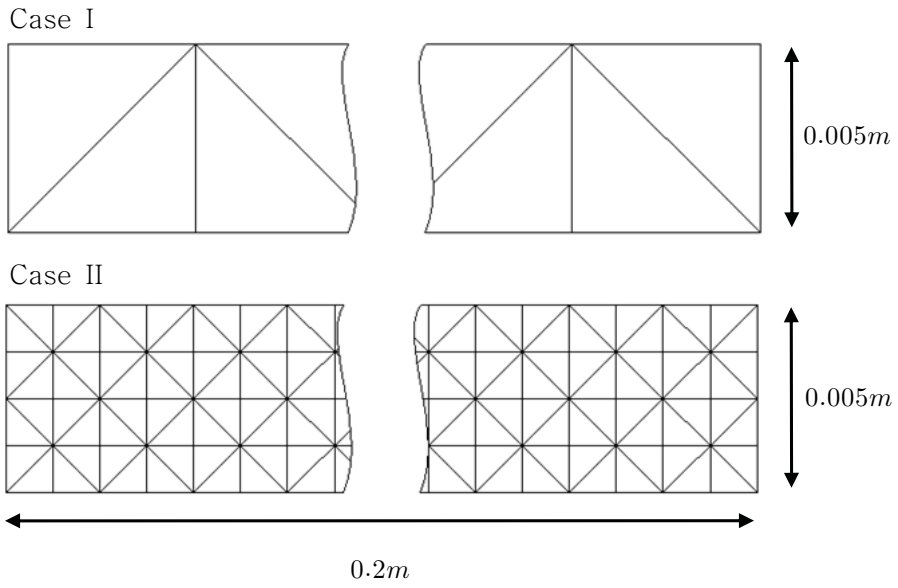

Figure 2.7: *FE models at the macro-level that are designed using different mesh sizes in order to test convergence of the multi-scale simulation result.*

due to a large jump in enthalpy at these locations.

During homogenization, the front is not as accurately tracked as in a single scale simulation (where adaptive meshing was used to capture the interface details). It is to be noted that the aim of homogenization is to obtain a homogenized description of the interface and capture fine scale information at various points in the macro-mesh with lower computational effort. The accuracy obtained during tracking of the solid-liquid interface is dictated by the element size in the macro-scale mesh. As the element size reduces, it is expected that the interface is better represented in the macro-scale model. As expected, it is seen from Fig. 2.9(b) that the enthalpy errors between macro- and micro- scales decreases as FE model with a finer macro-scale grid (Case II). A time step of one second was used in this case based on the mean square enthalpy error tests plotted in Fig. 2.8(b).

The results of solidification front position and the temperature-time history at various locations in the mesh are compared with analytical solution for two cases in

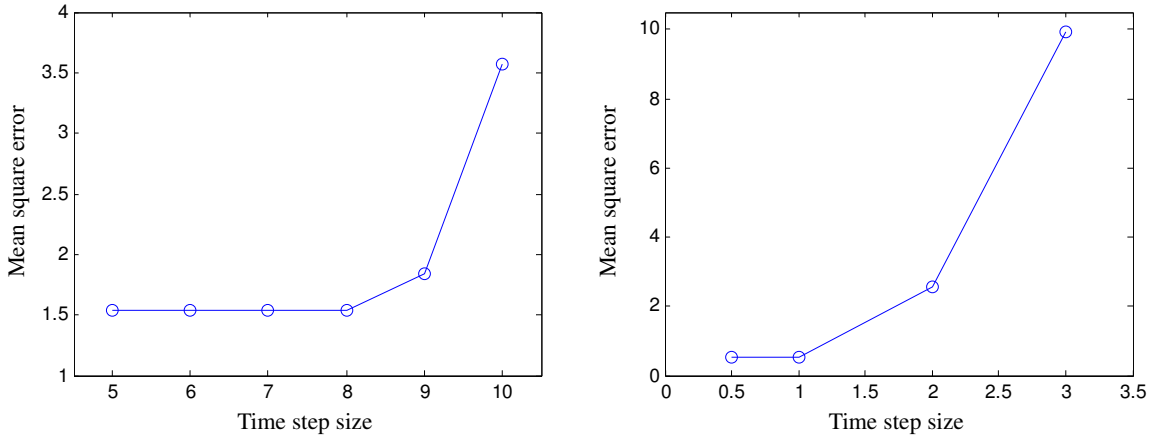

(a) (b)

Figure 2.8: *Mean square enthalpy errors with respect to time step size (in seconds) for the two cases. The errors are computed during the simulation from* $t = 4995sec$ *to* $t = 4995sec + \triangle t$ *(a) Case I - total number of element : 80 (a) Case II - total number of element : 1280.*

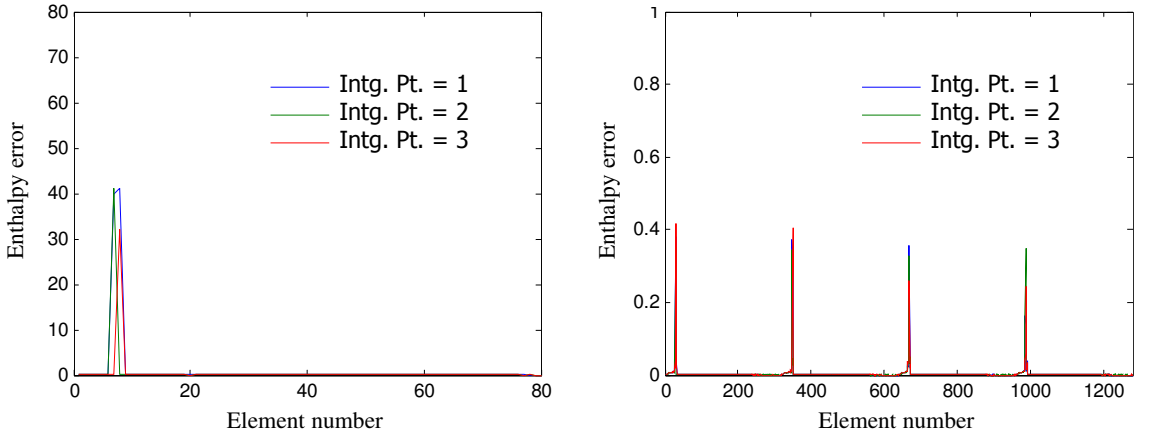

(a) (b)

Figure 2.9: *The enthalpy errors (in %) on each of the three integration points for all macro-scale elements at a simulation time of* $t = 2500$ *sec. (a) Case-I: elements along the x-axis in the macroscopic FE model are ordered from left to right. (b) Case-II: the enthalpy error for all elements are shown, there are four rows of elements along y-axis (see Fig. 2.7(b)), leading to four peaks for elements located at the interface.*

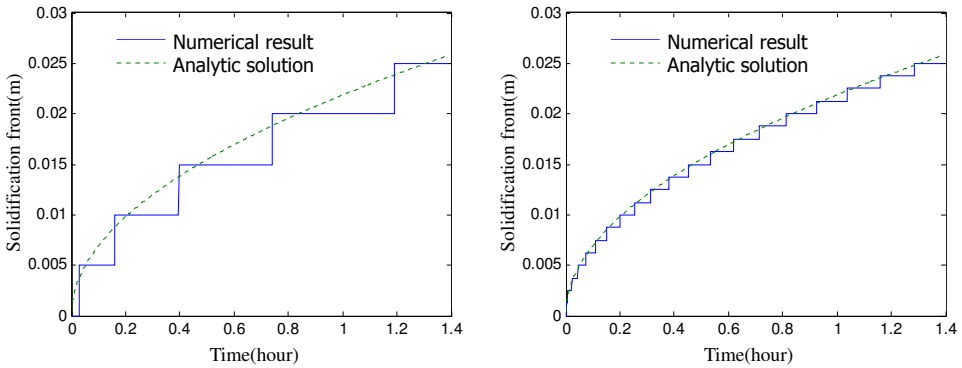

(a) (b)

Figure 2.10: *Comparison of predicted and analytical solution for interface positions computed using FE mesh from (a) case I (b) case II. During homogenization, the true location of the interface is not explicitly tracked in the macro-scale. The elements where the interface is located are depicted in the figure.*

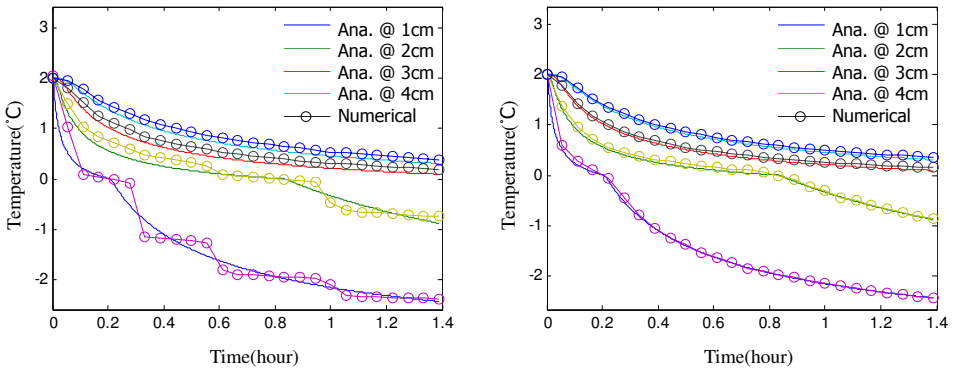

(a) (b)

Figure 2.11: *Comparison of predicted and analytical solution of temperature history at four different locations in the macro-scale mesh for (a) case I (b) case II*

Fig. 2.10 and Fig. 2.11 respectively. It is clear that as finer grids are employed at the macro-scale, the solid-liquid interface and temperature distribution are captured in an increasingly better manner. Multi-scale approach proposed here is computationally well suited in problems where there is a clear scale separation (eg. dendritic microstructure formation) and it is computationally impossible to resolve the fine scale details at macroscopic scales. Although the problem chosen here mimics scale separation, the real purpose however, is to validate the multi-scale homogenization with a known analytical solution. Future work in this area would involve development of adaptive mesh refinement and time-stepping methods to accelerate computation and address problems with large scale separation.

2.4 Conclusion

In this chapter, a non-linear coupled macro-micro finite element model is presented for addressing fluid solidification problems. Solidification problems involve evolution of surfaces coupled with flux jump boundary conditions across interfaces that have not been addressed using homogenization approaches. Homogenization of complex micro-scale behavior including moving interfaces and flux jumps has been performed. Based on the Hill's macro-homogeneity condition, macroscopic quantities are evaluated via consistent averaging of the microscopic values. The micro-scale model incorporates the physics associated with solidification including moving interfaces and flux discontinuities, while the macro-scale model needs to only model thermal conduction using continuous (homogenized) fields. The convergence behavior of the coupled macro-micro finite element scheme with respect to decreasing element size is analyzed by comparing with a known analytical solution of the Stefan problem. In this coupled non-linear multi-scale problem, although good convergence is achieved

at higher mesh densities, the time steps need to be carefully controlled to achieve macro-micro enthalpy balance and numerical stability. The approach is expected to be computationally superior in problems where there is a large scale separation between micro and macro scales , e.g. in case of dendritic growth.

CHAPTER III

Oxidative degradation of ceramic matrix composites

[1]Problems involving reaction and species diffusion involve field and flux jumps at a moving reaction front. In multi–scale problems such as carbon fiber composite oxidation, these effects need to be tracked at the microscopic scale of individual carbon fibers. A multi–scale model is derived in this paper for predicting species distribution in such problems using a fully–coupled multi-scale homogenization approach. The homogenized fluxes from the micro–scale are derived using Hill's macro–homogeneity condition accounting for both flux jumps and species density field jumps at the reacting interface in the micro–scale unit cell. At the macro–scale, the competition between the transport of reacting species (oxygen) and the reaction product (carbon dioxide) is modeled using homogenized mass conservation equations. The moving reaction front in carbon fibers at the micro–scale is tracked using level set method and an adaptive meshing strategy. The macroscopic weight loss of the composite when exposed to oxygen is simulated as a function of time using a coupled finite element methodology at various locations in a validated macroscopic model.

Advanced launch vehicles employ ceramic matrix composites (CMCs) as structural elements in heat shields, propulsion components and other applications that

[1]Reproduced from [38], S Lee and V Sundararaghavan, Multi-scale modeling of oxidative degradation of C/SiC composite, International Journal for Numerical Methods in Engineering, Published online, 2010

encounter high temperature oxidizing environments. These conditions progressively degrade the material which eventually leads to failure of the component well short of its expected life [19]. A variety of degradation mechanisms exist , with the predominant one being the oxidation of C fibers. For moderate to high temperatures, this oxidation process is controlled by the transport of oxygen into the porous SiC matrix. The oxygen transport phenomena in C/SiC composites is primarily through an interconnected void network in the matrix formed due to thermal expansion mismatch between carbon fibers and the matrix during processing. At the micro-scale, fine carbon fibers in within tows interact with oxygen and degrade at moderate to high temperatures. Initial models for studying oxidation of C/SiC composites at micro-scales assumed a steady state diffusion through the matrix [16, 22]. While these techniques model the micro-scale, techniques for homogenizing the results for use in global analysis was not developed. In [69], a continuum level theory for modeling composite oxidation was developed. The approach models the composite as a homogeneous mixture of matrix, carbon fiber and voids. While continuum models are practical approaches for predicting the behavior of C/SiC composites, they do not model the inherent heterogeneities involved in fiber oxidation. Multi-scale modeling by coupling macroscopic and microscopic models allow us to take advantage of both the efficiency of continuum models and the accuracy of the microscopic models.

The paper is organized as follows: In sections 3.1 and 3.2, a generalized scale transition for the multiscale problem is derived. The micro–scale and the macro–scale models are explained in sections 3.3 and 3.4, respectively. In section 3.5, the level set method used to model the moving interface is explained. Finally, in section 3.6, we discuss the methodology through an example of oxidation of a carbon composite.

3.1 Computational Homogenization Approach: Micro-scale Boundary Conditions

We consider a problem of oxidation, where carbon fibers residing in an inert matrix reacts with oxygen. The microstructure of a 2-D C/SiC composite is shown in Fig. 3.1. The unit cell consists of a single carbon fiber in a porous matrix occupying a volume V with external boundary S and outward normal $\boldsymbol{n}$. The oxidizing interface is a moving internal boundary which is initially an intact fiber–matrix interface. Material outside of the exposed carbon fiber surface occupies a volume V^+ and the exposed carbon fiber occupies a volume V^-. Here, V^+ and V^- are open subsets of the total unit cell volume V. At the interface S^I between V^+ and V^-, the carbon fiber oxidizes further and recedes into V^- along $\boldsymbol{n}^I$ with speed v_n, where $\boldsymbol{n}^I$ is the inward normal of S^I as indicated in Fig. 3.1). One such unit cell is attached to every integration point in the macro–scale finite element mesh.

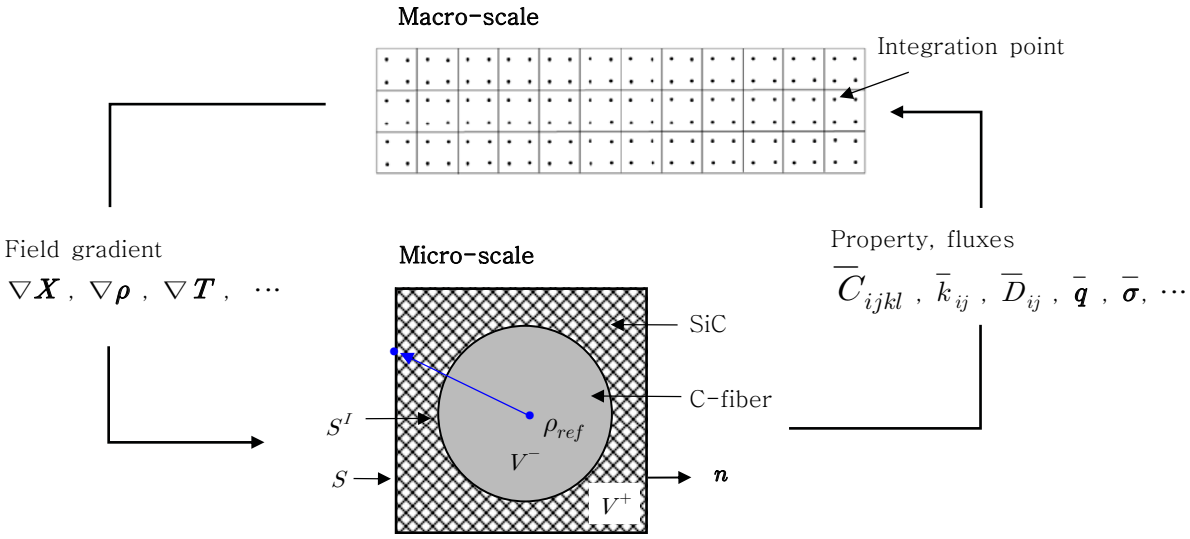

Figure 3.1: *Macro-scale is associated with a homogenized continuum. The macro-scale fields and field gradients are passed to the micro-scale as boundary conditions. Macro-scale fluxes and properties (at all integration points) are computed from the underlying microstructural sub–problems using averaging schemes.*

To identify boundary conditions that needs to be employed at the unit-cell level,

we employ the computational homogenization approach developed in [67, 45, 70, 51]. Macro-micro linking is achieved by decomposing the micro-scale field (ρ) into a sum of macroscopic field and a fluctuation field ($\tilde{\rho}$) as:

$$\rho = \rho_{ref} + \overline{\nabla \rho} \cdot \boldsymbol{x} + \tilde{\rho} \tag{3.1}$$

Here, the coordinate $\boldsymbol{x}$ represents a point on the micro-scale relative to a reference point at the center of the unit cell. The micro-scale partial density field of species i is denoted as ρ and the macroscopic reference partial density field of species i is denoted as ρ_{ref}. No subscripts (for eg. ρ_i for species i) are used in this section to maintain generality.

In general, we denote a macroscopic counterpart of a microscopic quantity (say, $\boldsymbol{\chi}$) as $\overline{\boldsymbol{\chi}}$. In the above equation, gradient in partial density of specie i at the macroscopic material point is denoted as $\overline{\nabla \rho}$ ($= \nabla_{macro} \bar{\rho}$). The most general assumption behind homogenization theory is that the gradient as seen at the macro-scale ($\overline{\nabla \rho}$) can be represented purely in terms of the field variables at the exterior boundary of the microstructure (Ref. [36, 28]):

$$\overline{\nabla \rho} = \frac{1}{V} \int_S \rho \boldsymbol{n} dS \tag{3.2}$$

Using the micro–scale field decomposition (Eq. 3.1), it can be shown that:

$$\frac{1}{V} \int_V \nabla \rho dV = \overline{\nabla \rho} + \frac{1}{V} \int_V \nabla \tilde{\rho} dV \tag{3.3}$$

We employ the generalized divergence theorem of the form $\int_V \nabla \chi dV = \int_S \chi \boldsymbol{n} dS + \int_{S^I} [|\chi|] \boldsymbol{n}^I dS^I$ in the above equation (where, $[|\chi|]$ denotes the jump in the field quantity across the evolving interface) to obtain the following relationship:

$$\frac{1}{V} \int_S \rho \boldsymbol{n} dS = \overline{\nabla \rho} + \frac{1}{V} \int_S \tilde{\rho} \boldsymbol{n} dS + \frac{1}{V} \int_{S^I} ([|\tilde{\rho}|] - [|\rho|]) \boldsymbol{n}^I dS^I \tag{3.4}$$

In the above equation, $[|\rho|]$ denotes the jump in partial density of specie i across the interface (S^I) with normal n^I. The jump in field across an interface is computed as $[|\rho|] = \rho_+ - \rho_-$. Here, ρ_+ and ρ_- refer to the field values in domain V^+ and V^-, respectively, close to a point on the interface.

Boundary conditions at the micro–scale are identified by comparing Eq. 3.2 with Eq. 3.4. Thus, any such boundary conditions derived must satisfy the 'linking condition':

$$\frac{1}{V}\int_S \tilde{\rho}\boldsymbol{n}dS + \frac{1}{V}\int_{S^I}([|\tilde{\rho}|] - [|\rho|])\boldsymbol{n}^I dS^I = 0 \tag{3.5}$$

A variety of boundary conditions may be derived that satisfy this constraint, however, following our previous work in [36], we focus on two possible boundary conditions (also called 'macro–micro linking assumption') as given below:

1. *Taylor boundary condition* involves specification of density field at all points in the microstructure. The approach is called 'Taylor model' based on similar terminology used in multi–scale deformation problems where displacements are fully specified at micro–scale. The Taylor model involves the following boundary conditions:

$$\tilde{\rho} = 0 \text{ on } V^+ \tag{3.6}$$

$$\rho = 0 \text{ on } V^- \tag{3.7}$$

The first term in Eq. 3.5 vanishes based on the first condition (Eq. 3.6). The second equation implies that the density of oxygen (and carbon dioxide) is negligible inside the carbon fiber. The mechanism of transport of oxygen in the carbon fiber is through lattice diffusion and this rate of diffusion is indeed negligible compared to gas phase transport (within pores) as noted in diffusion studies [78]. Comparing Eq. 3.7 with Eq. 3.1 leads to expression for $\tilde{\rho}$ inside

the carbon fiber: $\tilde{\rho} = -\rho_{ref} - \overline{\nabla\rho} \cdot \boldsymbol{x}$ on V^-. This leads to the expression for jump in the fluctuation density field at the interface:

$$[|\tilde{\rho}|] = \rho_{ref} + \overline{\nabla\rho} \cdot \boldsymbol{x} \text{ on } S^I \tag{3.8}$$

Similarly, comparing Eq. 3.6 with Eq. 3.1 leads to $\rho = \rho_{ref} + \overline{\nabla\rho} \cdot \boldsymbol{x}$ on V^+. Since $\rho = 0$ on V^- (Eq. 3.7), we can obtain the expression for jump in field at the interface

$$[|\rho|] = \rho_{ref} + \overline{\nabla\rho} \cdot \boldsymbol{x} \text{ on } S^I \tag{3.9}$$

From Eqs. 3.8 and Eq. 3.9, it can be verified that the expression $[|\tilde{\rho}|] - [|\rho|]$ in Eq. 3.5 also vanishes at points on the interface S^I. Thus, the Taylor assumption fully satisfies the linking condition (Eq. 3.5). Note that when using the Taylor linking assumption, the density fields at the micro–scale are fully specified from macro–scale quantities using the following equation:

$$\begin{aligned} \rho &= \rho_{ref} + \overline{\nabla\rho} \cdot \boldsymbol{x} \text{ on } V^+ \\ \rho &= 0 \text{ on } V^- \end{aligned} \tag{3.10}$$

2. Homogenization boundary condition: The essential boundary condition of the following form is specified:

$$\tilde{\rho} = 0 \text{ on } S \tag{3.11}$$

$$([|\tilde{\rho}|] - [|\rho|]) = 0 \text{ on } S^I \tag{3.12}$$

Using Eq. 3.11, essential boundary conditions (in the form of densities of oxygen and oxide species) are enforced at the boundaries of the unit cell as:

$$\rho = \rho_{ref} + \overline{\nabla \rho} \cdot \boldsymbol{x} \text{ on } S. \tag{3.13}$$

The second constraint in Eq. 3.12 is trivially satisfied based on Eq. 3.1 since macroscopic fields are assumed to be continuous. In homogenization approach, the density fields are known at the external boundary and micro–scale equilibrium equations are solved using finite element analysis to completely describe the oxygen density distribution at the micro–scale.

3.2 Micro–Macro linking: Transferring Fluxes and Diffusivities

In a coupled multi-scale model, the micro-scale results are used to compute transport properties and mass flux of species at the macro-scale. This forms the basis for *micro- to macro- linking*. In particular, we are interested in obtaining a macroscopic flux that satisfies Hills macro-homogeneity condition (which relates the macroscopic flux ($\bar{\boldsymbol{q}}$) with its microstructural counterpart ($\boldsymbol{q}$ [36, 49]) as follows:

$$\overline{\nabla \rho} \cdot \overline{\boldsymbol{q}} = \overline{\nabla \rho \cdot \boldsymbol{q}} \tag{3.14}$$

The fluxes need to be derived such that the above macro–homogeneity condition is satisfied when using either Taylor or homogenization boundary conditions as follows:

- *The Taylor model* Using boundary conditions (Eq. 3.6 and Eq. 3.7) in the macro–homogeneity condition (Eq. 3.14) leads to the following:

$$\begin{aligned} \overline{\nabla \rho \cdot \boldsymbol{q}} &= \frac{1}{V} \int_V \nabla \rho \cdot \boldsymbol{q} dV = \frac{1}{V} \int_V \nabla (\rho_{ref} + \overline{\nabla \rho} \cdot \boldsymbol{x}) \cdot \boldsymbol{q} dV \\ &= \overline{\nabla \rho} \cdot \frac{1}{V} \int_V \nabla \boldsymbol{x} \cdot \boldsymbol{q} dV = \overline{\nabla \rho} \cdot \frac{1}{V} \int_V \boldsymbol{q} dV \end{aligned} \tag{3.15}$$

Comparing Eq. 3.15 with Eq. 3.14:

$$\overline{\boldsymbol{q}} = \frac{1}{V} \int_V \boldsymbol{q} dV \tag{3.16}$$

- *The Homogenization model*

  We can show that a similar expression holds for the homogenization approach, ie. the macroscopic flux is same as the volume averaged heat flux at the micro-scale as shown below:

$$\overline{\boldsymbol{q}} = \frac{1}{V}\int_S \boldsymbol{x} q_n dS = \frac{1}{V}\int \boldsymbol{q} dV \tag{3.17}$$

  Derivation of the macroscopic flux for homogenization approach is more detailed than the derivation shown for the Taylor model. The derivation, which is based on the model explained in section 3.3, is separately provided in appendix B for the interested reader.

3.3 Micro–scale model

Since the microscopic length scale is considered to be much smaller than the scale of variation of the macroscopic temperature field, the micro-scale can be assumed to be at steady state at any instant of the macroscopic (transient) evaluation. This is a general assumption in homogenization theory due to the scale separation principle (eg. [51]).

The microscopic mass conservation equation is given as:

$$\nabla \cdot \boldsymbol{q}_i = -\nabla \cdot (\rho_i \boldsymbol{v}) \tag{3.18}$$

where, $\boldsymbol{q}_i$ denotes the mass flux of species i and ρ_i denotes the partial density of species i, and $\boldsymbol{v}$ represents the velocity of recession of the exposed carbon ($\boldsymbol{v}$ is non-zero only on the evolving interface). The micro–scale model includes both density jump ($[|\rho_i|]$) and flux jump ($[|\boldsymbol{q}_i|]$) for each specie i in the normal direction across the oxidizing interface. The condition for local mass balance across the oxidizing interface (with the flux and velocity component along the normal to the interface

given as q_n and v_n, respectively) is given by the Rankine–Hugoniot condition [57, 39]:

$$([|q_{n_i}|] + v_n[|\rho_i|]) = 0 \tag{3.19}$$

As described before, the primary mechanism of oxygen transport is concentration and pressure gradient driven diffusion through the pores (or cracks) in the matrix. In comparison, the species density and mass flux inside the carbon fiber is negligible (ie. $\boldsymbol{q}_i^- = \mathbf{0}$). Thus, the following interface flux condition can be derived to simulate mass loss of carbon fiber during oxidation:

$$\boldsymbol{q}_{O_2}^+ = -\frac{M_{O_2}}{M_C}\rho_c \boldsymbol{v}, \quad \boldsymbol{q}_{CO_2}^+ = \frac{M_{CO_2}}{M_C}\rho_c \boldsymbol{v} \text{ on } S^I \tag{3.20}$$

where, ρ_c is the density of the carbon fiber and M_i denotes the molecular mass of species i. The sign in the above equation indicates that oxygen is consumed and carbon dioxide is released at the interface during oxidation. The presence of interface flux at the micro–scale leads to a homogenized source term (for oxygen and carbon dioxide densities) in the macroscopic model.

3.3.1 Description of flow in the porous matrix at micro–scale

The mass flux of species within the matrix with volumetric porosity (ϕ) is a result of both pressure gradient driven flow and concentration gradient driven flow. The net flux is represented as:

$$\boldsymbol{q} = \boldsymbol{q}_i^\alpha + \boldsymbol{q}_i^\beta \tag{3.21}$$

where $\boldsymbol{q}_i^\alpha$ and $\boldsymbol{q}_i^\beta$ are the mass flux of species i due to pressure gradient-driven flow and concentration gradient-driven flow, respectively.

The flux contribution within the porous matrix due to pressure gradient driven flow is given by the Darcy's equation as:

$$\boldsymbol{q}_i^\alpha = -\rho_i^p \frac{1}{\mu_g}\mathbf{k}\nabla P \tag{3.22}$$

Here, $\rho_i^p = \frac{\rho_i}{\phi}$ denotes the partial density of the species i in the pore. In addition, μ_g denotes the viscosity of the gas mixture, $\mathbf{k} = k\boldsymbol{I}$ ($\boldsymbol{I}$ is the identity matrix) denotes the second-order material permeability tensor and P ($= \sum_i P_i = P_{O_2} + P_{CO_2}$) represents the total pressure of the gas mixture within the pore. The partial pressures (P_i) for each specie i are obtained using the ideal gas law ($\rho_i^P = \frac{M_i P_i}{RT}$, where R is the universal gas constant and T is the temperature). Similarly, the density of the mixture within the pore can be computed as $\rho^p = \frac{MP}{RT}$, where M is the averaged molecular weight of the gas mixture.

The concentration gradient driven mass flux in the porous matrix (based on Ref. [69]) is given using Fick's law of diffusion that involves the second-order areal porosity tensor ($\boldsymbol{\varphi}^A$) which is used as a measure of resistance to concentration gradient-driven flow through the pore network:

$$\boldsymbol{q}_i^\beta = -\rho^p D \boldsymbol{\varphi}^A \nabla \left(\frac{\rho_i^p}{\rho^p} \right) \tag{3.23}$$

where D is the diffusivity of oxygen w.r.t carbon dioxide. The areal porosity tensor can be thought of as a ratio of porosity to the tortuosity [6]. We employ the calibrated isotropic areal porosity from Ref. [69] for the matrix in the micro-scale calculations. The diffusivity D of gas specie A w.r.t gas specie B as given by the Chapman–Enskog equation [10]:

$$D = 0.0018583 \frac{\sqrt{T^3 \left(\frac{1}{M_A} + \frac{1}{M_B} \right)}}{P \sigma_{AB}^2 \Omega_{D,AB}} \left[cm^2/sec \right] \tag{3.24}$$

where, M_i is the molecular weight of species i and $\Omega_{D,AB}$ and σ_{AB} are computed from the Lennard-Jones potentials of the respective species (the parameters employed are tabulated in Table 3.1).

Table 3.1: Lennard Jones potential parameters for the diffusivity between O_2 and CO_2 (k: Boltzmann constant)

	$\sigma(\mathring{A})$	$\frac{\epsilon}{k}(K)$	$\sigma_{AB}(\mathring{A})$	$\frac{\epsilon_{AB}}{k}(K)$
O_2	3.433	113	$= \frac{1}{2}(\sigma_A + \sigma_B)$	$= \frac{\sqrt{\epsilon_A \epsilon_B}}{k}$
CO_2	3.996	190	$= 3.7145$	$= 146$

Temp.(°C)	$\frac{kT}{\epsilon_{AB}}$	$\Omega_{D,AB} = f(\frac{kT}{\epsilon_{AB}})$
900	8.01	0.7710
950	8.35	0.7657

Based on Eq. 3.21, Eq. 3.22 and Eq. 3.23, the constitutive relationships between homogenized fluxes and pressure gradients of oxygen and carbon dioxide can be derived as shown below:

$$\begin{aligned} \boldsymbol{q}_{O_2} &= \boldsymbol{\kappa}^{O_2/O_2}\nabla\rho_{O_2} + \boldsymbol{\kappa}^{O_2/CO_2}\nabla\rho_{CO_2} \\ \boldsymbol{q}_{CO_2} &= \boldsymbol{\kappa}^{CO_2/O_2}\nabla\rho_{O_2} + \boldsymbol{\kappa}^{CO_2/CO_2}\nabla\rho_{CO_2} \end{aligned} \tag{3.25}$$

where, $\boldsymbol{\kappa}^{A/B}$ denotes the micro–scale diffusivity relating the mass flux of species A with respect to the pressure gradient of species B and is computed as follows:

$$\begin{aligned} \boldsymbol{\kappa}^{O_2/O_2} &= -P_{O_2}\frac{1}{\phi\mu_g}\mathbf{k} - \frac{D}{\phi}\boldsymbol{\varphi}^A\frac{P_{CO_2}}{P} \\ \boldsymbol{\kappa}^{O_2/CO_2} &= \frac{M_{O_2}}{M_{CO_2}}(-P_{O_2}\frac{1}{\phi\mu_g}\mathbf{k} + \frac{D}{\phi}\boldsymbol{\varphi}^A\frac{P_{O_2}}{P}) \\ \boldsymbol{\kappa}^{CO_2/O_2} &= \frac{M_{CO_2}}{M_{O_2}}(-P_{CO_2}\frac{1}{\phi\mu_g}\mathbf{k} + \frac{D}{\phi}\boldsymbol{\varphi}^A\frac{P_{CO_2}}{P}) \\ \boldsymbol{\kappa}^{CO_2/CO_2} &= -P_{CO_2}\frac{1}{\phi\mu_g}\mathbf{k} - \frac{D}{\phi}\boldsymbol{\varphi}^A\frac{P_{O_2}}{P} \end{aligned} \tag{3.26}$$

The computational approach used for solve for the micro–scale field and flux distribution using the Taylor and homogenization approaches are listed below:

1. *Micro–scale model – Taylor approach*: The oxygen and carbon dioxide density field distributions in the micro–scale are directly obtained from the macro–scale solution using the Taylor boundary conditions (Eq. 3.10). The fluxes at all

points within the microstructure are subsequently calculated using Eq. 4.3. Note that the Taylor solution may not satisfy the micro–scale equilibrium (Eq. 3.18).

2. *Micro–scale model – Homogenization approach*: Boundary conditions (Eq. 3.13) are specified in each unit cell. The two coupled non-linear partial differential equations (Eq. 3.18), one equation each for O_2 and CO_2) are solved using finite element analysis. To solve these non-linear equations, Galerkin finite element method is adopted and the weak form is solved in an incremental iterative manner using the Newton-Raphson method.

3.4 Macro-scale model

The macroscopic simulation is performed using a diffusion equation that is defined on a uniformly meshed domain (Ω) with boundaries defined as Γ. Degrading interfaces are explicitly modeled at the micro-scale, while only homogenized transport equations are modeled at the macro-scale as given below:

$$\begin{aligned} \frac{\partial \bar{\rho}_{O_2}}{\partial t} + \nabla \cdot \bar{\boldsymbol{q}}_{O_2} &= \bar{Q}_{O_2} \\ \frac{\partial \bar{\rho}_{CO_2}}{\partial t} + \nabla \cdot \bar{\boldsymbol{q}}_{CO_2} &= -\bar{Q}_{CO_2} \\ \bar{\rho}(\Gamma, t > 0) = \hat{\rho}, \quad \bar{\rho}(\Omega, t = 0) &= \bar{\rho}_0 \end{aligned} \tag{3.27}$$

where, $\bar{\rho}$ is the macroscopic (homogenized) partial density and $\bar{Q}_i$ is the homogenized mass consumption rate of species i per unit bulk volume defined as (where f is the volume fraction of the burnt carbon fiber at the micro–scale):

$$\bar{Q}_i = \rho_c \frac{M_i}{M_c} \frac{\partial f}{\partial t} \tag{3.28}$$

To solve the non-linear transient macroscopic equations (Eq. 3.27), Galerkin finite element method and backward Euler time integration are adopted and the

weak form is solved in an incremental iterative manner using the Newton-Raphson method. The $(\lambda+1)^{th}$ Newton-Raphson step at time $(t+1)$ involves solution of the system $\boldsymbol{K}\{\delta\bar{\boldsymbol{\rho}}^{\lambda+1,t+1}\} = \boldsymbol{f}$, where the unknown vector in the above system is the increment in the partial density ($\delta\bar{\boldsymbol{\rho}}^{\lambda+1,t+1}$) of oxygen and carbon dioxide. In our numerical approach, the reference density ρ_{ref} and consumption rate $\bar{Q}$ (of each species i) for the next time step are evaluated at the end of each time step of the simulation. The reference density ρ_{ref} is obtained using the macro–micro balance of mass condition ($\bar{\rho} = \frac{1}{V}\int_V \rho dV$) and Eq. 3.1. This definition is consistent with the condition that stored mass at macro-scale is same as the average micro-scale stored mass [36]. To further understand the micro-scale quantities that are needed to create the overall system of equations, the Jacobian matrix and force vector for a finite element e with shape functions N_i occupying a volume Ω^e are expanded below:

$$K_{ij}^{t+1,\lambda} = \begin{bmatrix} \frac{1}{\triangle t}\int_{\Omega^e} N_i N_j dV - \int_{\Omega^e} \frac{dN_i}{dx_p}\bar{\kappa}_{pq}^{O_2/O_2}\frac{dN_i}{dx_q}dV & -\int_{\Omega^e} \frac{dN_i}{dx_p}\bar{\kappa}_{pq}^{O_2/CO_2}\frac{dN_i}{dx_q}dV \\ -\int_{\Omega^e} \frac{dN_i}{dx_p}\bar{\kappa}_{pq}^{CO_2/O_2}\frac{dN_i}{dx_q}dV & \frac{1}{\triangle t}\int_{\Omega^e} N_i N_j dV - \int_{\Omega^e} \frac{dN_i}{dx_p}\bar{\kappa}_{pq}^{CO_2/CO_2}\frac{dN_i}{dx_q}dV \end{bmatrix}$$

$$f_i^{t+1,\lambda} = \begin{bmatrix} -\int_{\Omega^e} N_i \frac{\bar{\rho}_{O_2} - \bar{\rho}^t_{O_2}}{\triangle t}dV + \int_{\Omega^e}\frac{dN_i}{dx_p}\bar{q}_{O_2p}dV + \int_{\Omega^e} N_i \bar{Q}^t_{O_2}dV \\ -\int_{\Omega^e} N_i \frac{\bar{\rho}_{CO_2} - \bar{\rho}^t_{CO_2}}{\triangle t}dV + \int_{\Omega^e}\frac{dN_i}{dx_p}\bar{q}_{CO_2p}dV + \int_{\Omega^e} N_i \bar{Q}^t_{CO_2}dV \end{bmatrix}$$

From the above equations, it is seen that homogenized diffusivities $\bar{\boldsymbol{\kappa}}^{A/B}$ relating the mass flux of species A with respect to the pressure gradient of species B needs to be defined at each integration point in the macro-scale. The evaluation of the homogenized diffusivity for Taylor and Homogenization approaches are listed below: In the Taylor model, the diffusivity is directly obtained by comparing Eq. 3.10, Eq. 4.3 and Eq. 3.16 as:

$$\bar{\boldsymbol{\kappa}}^{A/B} = \frac{1}{V}\int_\Omega \boldsymbol{\kappa}^{A/B} dV \tag{3.29}$$

In the homogenization approach, the homogenized diffusivity can be obtained using a perturbation analysis [44] or direct matrix manipulation [36]. In the perturbation approach, components of the macroscopic density gradient is independently perturbed by a small amount ϵ which affects the boundary conditions at the micro-scale through Eq. 3.1. The micro-scale problem is solved again using the perturbed boundary conditions and the resulting perturbation in homogenized flux is used to compute the homogenized diffusivity. This involves solution of several additional micro-scale problems during each Newton-Raphson iteration at the macro-scale to compute the values involved in $\bar{\boldsymbol{\kappa}}^{A/B}$. In this work, we follow the FE matrix approach to obtain homogenized diffusivity by direct manipulation of the converged Jacobian and residual matrices of the micro-scale problem. The highlight of this approach is that the diffusivity can be obtained as a closed form expression directly from the micro–scale solution. The steps to compute the homogenized diffusivity are as follows. In the finite element formulation (mesh with N nodes), the unknown vector $\boldsymbol{\rho}$ and the normal flux vector $\boldsymbol{q}_n$ are given as:

$$\{\rho\} = \begin{bmatrix} \rho^1_{o_2} \\ \rho^1_{co_2} \\ \dots \\ \rho^N_{o_2} \\ \rho^N_{co_2} \end{bmatrix} \text{ and, } \{q_n\} = \begin{bmatrix} q^1_{n_{o_2}} \\ q^1_{n_{co_2}} \\ ... \\ q^N_{n_{o_2}} \\ q^N_{n_{co_2}} \end{bmatrix} \tag{3.30}$$

Macroscopic flux is first written using the vector of normal fluxes on the external

nodes of the microstructure ($\{q_n\}^{ext}$) using finite element matrix representation as follows:

$$\overline{\boldsymbol{q}} = \begin{bmatrix} \overline{\boldsymbol{q}}_{o_2} \\ \\ \overline{\boldsymbol{q}}_{co_2} \end{bmatrix} = \frac{1}{V} \begin{bmatrix} \int_S \boldsymbol{x} q_{n_{o_2}} dS \\ \\ \int_S \boldsymbol{x} q_{n_{co_2}} dS \end{bmatrix} = \boldsymbol{L}\{q_n\}^{ext} \tag{3.31}$$

where L is a matrix of size $4 \times 2N^{ext}$ where N^{ext} is the number of nodes on the external boundary of the microstructure.

To compute the homogenized diffusivity ($\bar{\boldsymbol{\kappa}}$ – a 4×4 matrix) , one needs to compute sensitivity of $\{q_n^{ext}\}$ to perturbations in the macroscopic density gradient $\delta(\overline{\nabla \rho})$ as:

$$\delta\overline{\boldsymbol{q}} = \boldsymbol{L}\{\delta q_n\}^{ext} = \bar{\boldsymbol{\kappa}} \begin{bmatrix} \delta\overline{\nabla \rho}_{o_2} \\ \\ \delta\overline{\nabla \rho}_{co_2} \end{bmatrix} = \bar{\boldsymbol{\kappa}}\{\delta(\overline{\nabla \rho})\} \tag{3.32}$$

To obtain the homogenized diffusivity, the converged finite element solution from the Newton-Raphson iterations at the micro-scale is employed as follows:

$$\begin{bmatrix} \boldsymbol{K}_{ee} & \boldsymbol{K}_{ei} \\ \\ \boldsymbol{K}_{ie} & \boldsymbol{K}_{ii} \end{bmatrix} \begin{bmatrix} \delta\boldsymbol{\rho}^e \\ \\ \delta\boldsymbol{\rho}^i \end{bmatrix} = \begin{bmatrix} 0 \\ \\ 0 \end{bmatrix}$$

In the above equation, the assembled matrix ($\boldsymbol{K}$) on the left hand side is the Jacobian matrix of the Newton-Raphson iteration. The residual on the right hand side goes to zero since the micro-scale solution has converged. Vectors $\delta\boldsymbol{\rho}^e$ and $\delta\boldsymbol{\rho}^i$ contain the densities on the external and internal nodes of the microstructure, respectively. The submatrix $\boldsymbol{K}_{ee}$ contains entries in the Jacobian matrix corresponding to only the external nodes of the microstructure and is of size $2N^{ext} \times 2N^{ext}$. Using our

boundary condition on the temperatures on the external nodes (Eq. 3.1), sensitivity of densities on external nodes of the micro-scale mesh to perturbation in the imposed macroscopic enthalpy gradient can be written as:

$$\{\delta\boldsymbol{\rho}^e\} = \boldsymbol{G}\begin{bmatrix} \delta\overline{\nabla\rho}_{o_2} \\ \\ \delta\overline{\nabla\rho}_{co_2} \end{bmatrix} = \boldsymbol{G}\{\delta(\overline{\nabla\rho})\} \tag{3.33}$$

where G is a matrix of size $2N^{ext} \times 4$.

Substituting the above relation into the converged matrix equation at the micro-scale and taking the known quantities to the right hand side, we obtain the equation:

$$\begin{bmatrix} \boldsymbol{K}_{ee} & \boldsymbol{K}_{ei} \\ \\ \boldsymbol{K}_{ie} & \boldsymbol{K}_{ii} \end{bmatrix}\begin{bmatrix} 0 \\ \\ \delta\boldsymbol{\rho}^i \end{bmatrix} = \begin{bmatrix} -\boldsymbol{K}_{ee}\boldsymbol{G}\{\delta(\overline{\nabla\rho})\} \\ \\ -\boldsymbol{K}_{ie}\boldsymbol{G}\{\delta(\overline{\nabla\rho})\} \end{bmatrix}$$

The vector on the right hand side provides the sensitivity of microscopic flux to the macroscopic density gradient, which leads to the homogenized conductivity, $\bar{\boldsymbol{\kappa}}$ as follows:

$$\delta {q_n}^{ext} = -\boldsymbol{K}_{ee}\boldsymbol{G}\{\delta(\overline{\nabla\rho})\}$$

$$\bar{\boldsymbol{\kappa}} = -\boldsymbol{L}\boldsymbol{K}_{ee}\boldsymbol{G} \tag{3.34}$$

To aid in speeding up the solution process for the multi-scale problem, the algorithm was parallelized using MPI. The macro-scale domain was decomposed and elements in each domain distributed to different processors. The underlying micro-scale problems were solved in serial in each processor. The simulator was developed using object oriented programming and was dynamically linked to the parallel toolbox PetSc [8] for parallel assembly and solution of linear systems. For solution of linear systems, a GMRES solver along with block Jacobi and ILU preconditioning from the PetSc toolbox was employed.

3.5 Tracking of the interface using level set method and adaptive meshing

Level set approach provides a natural way of tracking the degrading interface at the micro-scale during FE computations. To describe the interface, we construct a field ϕ such that at any time t, the interface is equal to the zero level set of ϕ, i.e.,

$$S^I(t) = \{x \in V^+ \cup V^-, \text{ such that } \phi(\boldsymbol{x}, t) = 0\}. \tag{3.35}$$

Initially, ϕ is set equal to the signed distance function from the interface S^I

$$\phi(\boldsymbol{x}, 0) = \begin{cases} +d(\boldsymbol{x}, 0), & \boldsymbol{x} \in V^+; \\ 0, & \boldsymbol{x} \in S^I; \\ -d(\boldsymbol{x}, 0), & \boldsymbol{x} \in V^-. \end{cases} \tag{3.36}$$

where $d(\boldsymbol{x}, 0)$ is the normal distance of a point $\boldsymbol{x}$ from the interface. The idea behind the level set method is to move ϕ with the correct speed $\mathbf{v}$ at the interface. The interface position is thus implicitly stored in ϕ. The equation of motion governing ϕ is given as follows ([74]):

$$\frac{\partial \phi}{\partial t} + \boldsymbol{v} \cdot \nabla \phi = 0. \tag{3.37}$$

This equation moves ϕ with correct speed at the interface so that S^I will always be equal to the zero level set of ϕ. We employ the stabilized Galerkin formulation on unstructured adaptive grids for solving the level set equation. The numerical implementation of the level set method is same as that detailed in Ref. [74].

The mass loss rate of oxygen has been calibrated as an Arrhenius equation using experimental results in [23]. To convert the measured *mass loss* rate to the velocity of oxidation at nodal points in the micro–scale oxidizing interface, we assume that

the intact carbon fiber of initial radius r_0 oxidizes to a smaller radius r after a short duration Δt. The velocity of recession at any point can then be found by scaling the mass loss rate with the initial as well as current radius r_o and r as below:

$$\boldsymbol{v} = \frac{dr}{dt}\boldsymbol{n} = \frac{{r_0}^2}{2r} k_0 e^{\left(\frac{-E_a}{RT}\right)} \left(\frac{P_{O_2}}{P^*_{O_2}}\right)^{k_1} \boldsymbol{n} \tag{3.38}$$

The experimentally calibrated parameters, E_a, k_0, k_1 from Ref. [69] are listed in Table 3.2. We approximate the current radius r using the area of current carbon fiber A as $r = \sqrt{\frac{A}{\pi}}$. Note that an inert coating (pyrolitic carbon) is generally applied on the carbon fiber to provide oxidation resistance. For simplicity, the ensuing simulations assume that the coating is not present and the carbon fiber is fully exposed to oxygen. Nevertheless, the effect of coatings can be easily included in this model by using a different recession velocity (Eq. 3.38) for the coating material.

Table 3.2: List of material constant for the carbon fiber oxidation example.

Material constant	Matrix	Void	C-fiber
Volumetric porosity	0.1	1	0
$\frac{\text{Permeability}}{\text{Viscosity}}\left(\frac{m^2}{kPa\ sec}\right)$	10^{-7}	0	0
Areal porosity	0.00018	1	0
$M_{O_2}(g/mol)$	32		
$M_{CO_2}(g/mol)$	44		
$M_C(g/mol)$	12		
$k_0(s^{-1})$	6452.35		
$E_a(J/mol)$	118300		
$\rho_c(kg/m^3)$	1740		
$r_0(\mu m)$	3.5		

3.6 Computational approach and Numerical Results

The overall solution scheme is shown in Table. 3. Homogenization and Taylor model differ in the way the micro–scale problem is solved, with the homogenization

approach accounting for micro–scale equilibrium.

Table 3.3: Solution scheme for multiscale modeling of carbon fiber oxidation

(1) Initialize macro-scale model and assign a microstructure (and FE meshes) to every integration point.

(2) Apply time increment Δt to the macro-scale problem.

(3) Iteration step:

(3.1) Assemble the macroscopic stiffness matrix.

(3.2) Solve the macroscopic system and compute density and the density gradient at each integration point.

(3.3) Loop over all integration points

(a) (Only done for the first NR iteration) Update the carbon fiber using level set method.

(b) *Taylor model*: Transfer densities to every point in the micro-scale mesh using Eq. 3.10.

Homogenization model: Transfer boundary conditions to micro-scale problem. Assemble and solve the micro-scale problem.

(c) Calculate the volume averaged macro-flux (Eq. 3.16), the source term (Eq. 3.28), the macro-diffusivity (Eq. 3.29 for Taylor and Eq. 3.34 for Homogenization models).

(3.4) Assemble the macroscopic residual vector.

(4) Check convergence, if not converged go to step 3, otherwise go to step 2.

In this section, we focus on the problem of oxidation of an assembly of carbon fibers within *a single carbon tow*. Scanning electron micrographs of cross section of carbon tows reported in Refs. [42, 43] (Fig. 3.2(b)) reveal arrangement of carbon fibers in a hexagonal lattice within a tow. Micrographs obtained at high magnifications show the oxidation of individual carbon fibers (Fig. 3.2(c)) as well as the preferential oxidation of carbon fibers adjoining the porous matrix due to high oxygen availability. As the outer fibers oxidize, oxygen diffuses inward along the voids formed and react with the interior fibers. The oxidized carbon fiber front (Fig. 3.2(b)) evolves inward into the carbon fiber tow, until all the fibers are oxidized. In our numerical model, a section of carbon fiber tow (with about 600 carbon fibers)

is taken to be our macroscopic model. The size of our macroscopic simulation cell (shown in Fig. 3.3(a)) is indicated using dotted lines on the micrographs. In the macroscopic model, the evolution of homogenized carbon density is tracked as oxygen diffuses from the left end to the right end. All the boundaries in the model are insulated (as shown in Fig. 3.2(a)) except one side that is exposed to the external environment of pure oxygen with imposed pressures of $P_{O_2} = 0.1atm$ and $P_{CO_2} = 0atm$ for $t > 0$. The system is modelled at a constant temperature of 950°C. An initial condition (at $t = 0$) of $P_{O_2} = 0.1atm$ and $P_{CO_2} = 0atm$ is imposed at all points in the specimen. The micro–scale physics of carbon fiber oxidation is introduced by modeling a single carbon fiber within a hexagonal unit cell as shown in Fig. 3.3(b). Since the carbon fibers do not mediate the diffusion of the gas species, the carbon fiber is not modeled in the microscale. The unit cell is assigned to each integration point in the macro–grid.

3.6.1 Convergence study

Micro–scale mesh convergence study was performed by considering the volume loss of carbon fibers as the convergence metric. Adaptive meshing is used to track the evolving micro–scale carbon fiber interface. A refinement procedure based on unstructured grids is employed in this work. During mesh refinement, each triangular element is subdivided into four triangles (as shown in Fig. 3.4(a)) by adding middle nodes at its three edges. Information about the level of refinement is stored in a tree data structure following the approach in Ref. [74], which is capable of tracking refined elements and ensures overall grid conformity. Due to the use of such unstructured grids, we report the level of adaptivity using the smallest element edge length in the mesh. The adaptive meshing strategy used in the micro–scale is shown in Fig. 3.4(b). The resulting mesh is coarser in the porous matrix and progressively becomes

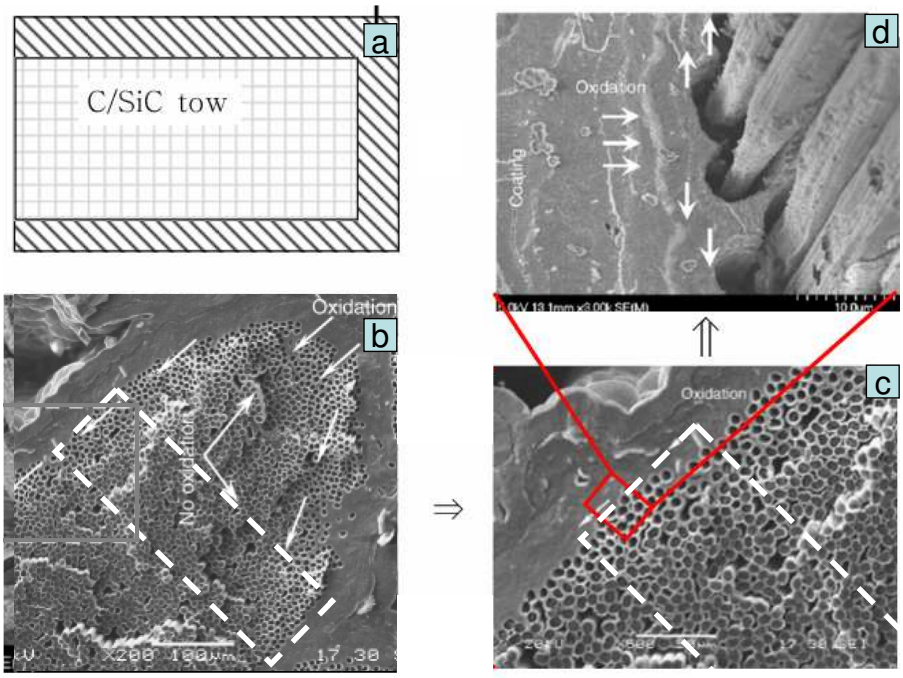

Figure 3.2: *The micrographs represent experimental results of C/SiC composite oxidation in a controlled environment reported in [42] and [43]. Figure (d) shows the simulation cell: all the boundaries in the model are insulated except one side that is exposed to the external oxidizing environment. Size of the simulation cell at the macro–scale is indicated using dotted lines in (b). The simulation cell contains about 600 carbon fibers.*

finer as we reach closer to the evolving interface.

For this micro–scale convergence study, a constant oxygen pressure of $0.05atm$ is imposed at all points in the micro–scale unit cell. As shown in the Fig. 3.5(a), it is seen that the temporal evolution of carbon fiber volume converges as the level of mesh adaptivity increases. Based on this study, we selected the adaptive mesh setting that ensures a minimum element size of 0.029 microns for the micro–scale problem. Subsequently, macro–scale grid convergence was tested using the configuration given in Fig. 3.2(a)). An ambient pressure of $P_{O_2} = 0.1atm$ and $P_{CO_2} = 0atm$ for $t > 0$ is employed. The temporal evolution of macro–scale carbon fiber volume fraction is reported for various different macro–scale FE meshes in Fig. 3.5(b). Taylor model was employed and time–steps were chosen adaptively during the simulation to ensure

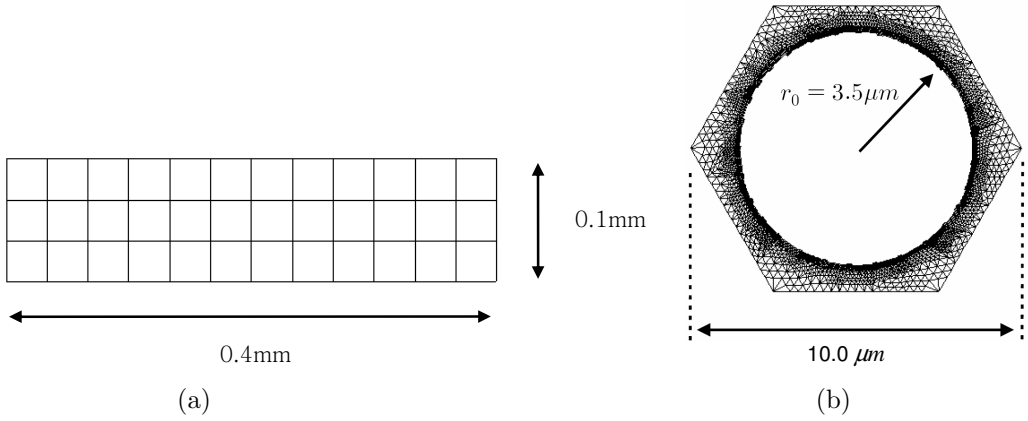

Figure 3.3: *(a) 2D Macro-scale finite element grid (b) Micro–scale finite element grid*

convergence of the overall multi–scale system. A grid with 12 elements along the x-axis and 3 elements along the y- axis was selected (a 12×3 grid, Fig. 3.3(a)) based on this study and employed in the subsequent simulations.

3.6.2 Numerical results of the Taylor and Homogenization multi-scale model

Simulation of carbon tow oxidation in the configuration depicted in Fig. 3.2(a) was carried out using both Taylor and Homogenization approaches. In general, simulations reveal diffusion controlled kinetics at the beginning of oxidation. As the carbon fibers oxidize, a void is created in place of the oxidized carbon fiber. This greatly increases subsequent diffusion of oxygen towards the interior of the carbon tow. Due to increased oxygen availability, a transition from diffusion controlled kinetics to reaction controlled kinetics is seen. This is exemplified by a linear rate law, ie. oxidized carbon volume fraction increasing linearly with respect to time. A mixed rate law of the following form describes the overall oxidation process:

$$\frac{\sqrt{x}}{k_r} + \frac{x}{k_l} = t \tag{3.39}$$

where, k_r and k_l are the rate constants. Fig. 3.6(a) compares the oxidized carbon fiber volume fraction predicted at various times by the Taylor and homogenization approaches. Both Taylor and Homogenization approaches show similar behavior,

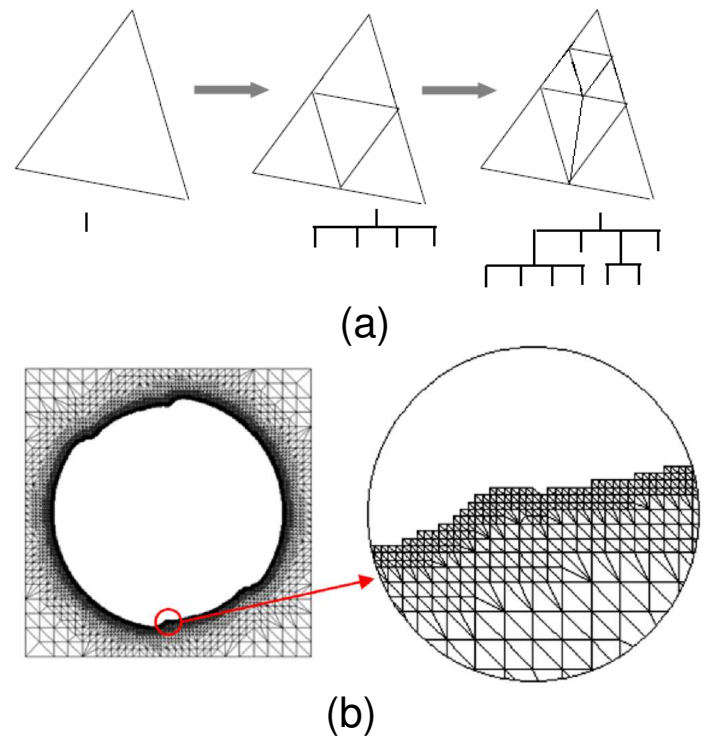

Figure 3.4: (a) A typical sequence of mesh refinement is shown along with the associated data structure. (b) Oxidizing interface is accurately tracked using this adaptive meshing strategy.

and in both cases, the transition to a reaction dominated regime occurs at a time of about 13 seconds. However, the reaction rate constants predicted by the Taylor and Homogenization approaches are quite different as seen in Table. 3.4. The Taylor model provides a overconstrained response compared to FE homogenization approach due to strict imposition of oxygen and carbon dioxide densities within the unit cell. In fact, the Taylor model provides an upper bound response for system, an effect well studied in literature (eg. [70]). This is further exemplified in Fig. 3.6(b) which shows the oxygen partial pressure distribution within the macro–scale mesh at various times. The Taylor model, as expected, predicts faster oxygen transport within the tow compared to the FE homogenization approach. FE homogenization approach solves the micro–scale equilibrium equations and the micro–scale solution is more

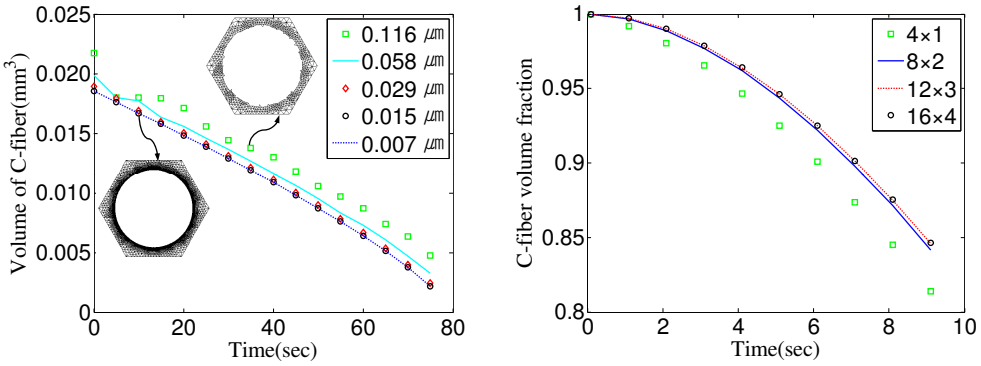

Figure 3.5: *(a) Micro–scale convergence study: Carbon fiber volume at the micro–scale is tracked as a function of time using different levels of adaptive meshing. The minimum element edge length in the mesh is reported here. The volume is calculated with assuming the length in z-direction is 1mm.(b) Macro–scale convergence study: Carbon fiber volume fraction vs. time is plotted for different mesh sizes. A mesh size of $a \times b$ indicates a elements along x–axis and b elements along the y–axis*

physically reasonable. However, the choice of selection of one model versus another is based on the relative importance of accuracy versus computational speed. In the Taylor model, there is no need for finite element computations at the micro–scale and the convergence of the overall non–linear multiscale scheme is faster. In the case considered here, Taylor model was solved four times faster than the homogenization model.

Table 3.4: Square root and linear rate constants obtained by curve fitting the simulation results

	$k_r \times 10^4 (1/s^2)$	$k_l \times 10^2 (1/s)$	Transient time(sec)
Taylor	13.7	3.8	13.1
Homogenization	8.4	2.5	13.1

In order to illustrate changes in the carbon fiber configuration in the micro–scale, the Taylor model solution at selected 6 integration points are shown in Fig. 3.7 at a time of 25.1 seconds. Although the macro–problem studied corresponds to a one dimensional diffusion, the micro–scale oxidation results shown in Fig. 3.7 do not follow this trend. Indeed, the one dimensional nature of the macroscopic density

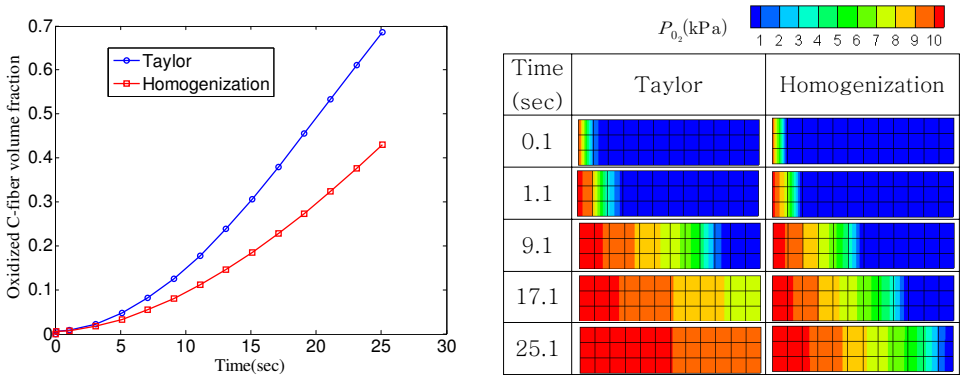

(a) (b)

Figure 3.6: *Comparison of Taylor and Homogenization approaches (a) Recessed carbon fiber volume fraction vs. time at the macro-scale. (b) Oxygen pressure distributions at various times in the macro–scale.*

gradient is considered in the micro–scale simulation through the scale linking equation (Eq. 3.1). However, the characteristic length scale over which the macroscopic field variables vary is much larger than the size of the microscopic volume considered. Consequently, the contribution of the macroscopic gradient term to the micro–scale oxygen and carbon dioxide density (ie. term $\nabla\rho \cdot \boldsymbol{x}$ in Eq. 2.1) is not significant compared to the macroscopic oxygen density term (term ρ_{ref} in Eq. 3.1). In other words, the macroscopic oxygen density field translates to a nearly constant oxygen density at the level of the RVE. This kind of uniform oxidation of carbon fibers is indeed seen from experimental micrographs as shown in Fig. 3.2(d).

A comparison of the simulation results from the Taylor and homogenization approaches at various locations in the macroscopic mesh at a simulation time of 25.1 seconds is shown in Fig. 3.8. In this figure, the tan, white and blue colored areas indicate matrix, void and carbon fiber respectively. Both Taylor and homogenization models indicate complete oxidation of the carbon fibers located closest to the exposed macro–scale surface (left edge) at 25.1 seconds. The oxygen partial pressure solution at the micro–scale shows the contrast between the two approaches. The boundary conditions in the Taylor model lead to enforcement of high oxygen densities within

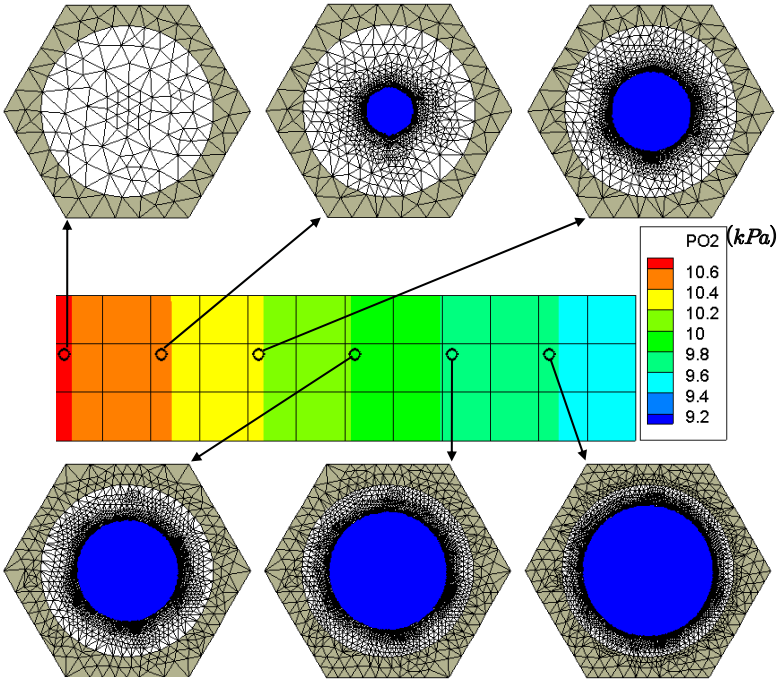

(a)

Figure 3.7: *Carbon fiber configurations in micro at 25.1 seconds at* 950°C*; tan, white and blue colored area indicate matrix, void and carbon fiber respectively.*

the matrix compared to the physically accurate solution from homogenization that satisfies micro–scale equilibrium. In the steady state micro–scale solution, the oxygen density in the void (that is left behind after oxidation of the carbon fiber) is expected to be uniform due to much faster diffusion in the void compared to the porous matrix. This is clearly seen from the homogenization approach, while in the Taylor model, a variation of oxygen density in the void is enforced. Further, in all cases, the Taylor model provides an upper bound for the oxygen density solution (and faster oxidation) at both macro– and micro–scales. The Taylor model predicts partial oxidation while homogenization approach predicts an almost intact carbon fiber at an integration point located on the right end. This effect is clearly seen by plotting the spatial distribution of carbon volume fraction in the composite at 0, 11.1 and 25 seconds (as shown in Fig. 3.9).

The pore structure of C/SiC composite is affected by thermally induced stresses in

the component. Thermal stresses result in matrix cracks and de-bonds between the carbon fibers, the pyro-carbon coating and the SiC matrix. One would expect that the porosity in the matrix will be a complex function of temperature, heating rate and externally applied loads. Deformation and thermal shocks lead to increased damage in the matrix, thus increasing oxygen availability at degrading interfaces. Increased oxidation, in turn, leads to overall weakening of the material making it susceptible to further damage. This phenomena of strong 'stress-oxidation' coupling is explained in [76]. The micro-scale model presented here is a first step towards a multi-scale approach for studying stress-oxidation coupling and associated mechanical property degradation in C/SiC composites. In the future, we plan to model the structural loading and thermal cycling effects that lead to porosity evolution and increased oxygen diffusion in the matrix.

3.7 Conclusion

In this paper, a non-linear coupled macro-micro finite element model is presented for addressing carbon fiber oxidation problems. Oxidation involves evolution of carbon fiber surfaces coupled with flux jump boundary conditions across interfaces that have not been addressed using homogenization approaches. Homogenization of complex micro-scale behavior including moving interfaces and flux jumps has been performed in this work. Based on the Hill's macro-homogeneity condition, macroscopic quantities are evaluated via consistent averaging of the microscopic values. The micro-scale model incorporates the physics associated with oxidation including moving interfaces and flux discontinuities, while the macro-scale model needs to only model diffusion using continuous (homogenized) fields. Two multiscaling procedures were outlined in this work: one based on assumed solution in the micro–scale (Taylor

model) and another based finite element solution of the micro–scale problem (Homogenization approach). A nested finite element solution scheme is implemented into a FE framework and the macroscopic diffusivity is derived in a consistent manner for these two approaches.

The results from these two multi–scaling approaches were compared for a simple one dimensional oxidation of a carbon fiber tow. In both models, the influence of microstructural evolution (e.g. carbon fiber oxidation) on the competition between macroscopic oxygen and carbon dioxide transport in the macro–scale can be introduced and treated effectively. Taylor model is computationally efficient but provides an upper bound response and predicts faster oxygen transport within the tow compared to the FE homogenization approach. The proposed method, when combined with thermo–mechanical field effects, constitutes a powerful tool, for modeling high temperature oxidation of composites. The homogenization approach enhances the understanding and modeling of micro–scale interfacial phenomena and in the future, would allow modeling of interesting mechanisms such as interaction of porosity evolution with carbon fiber oxidation ('stress–oxidation coupling') that cannot be explained without incorporating microstructural details.

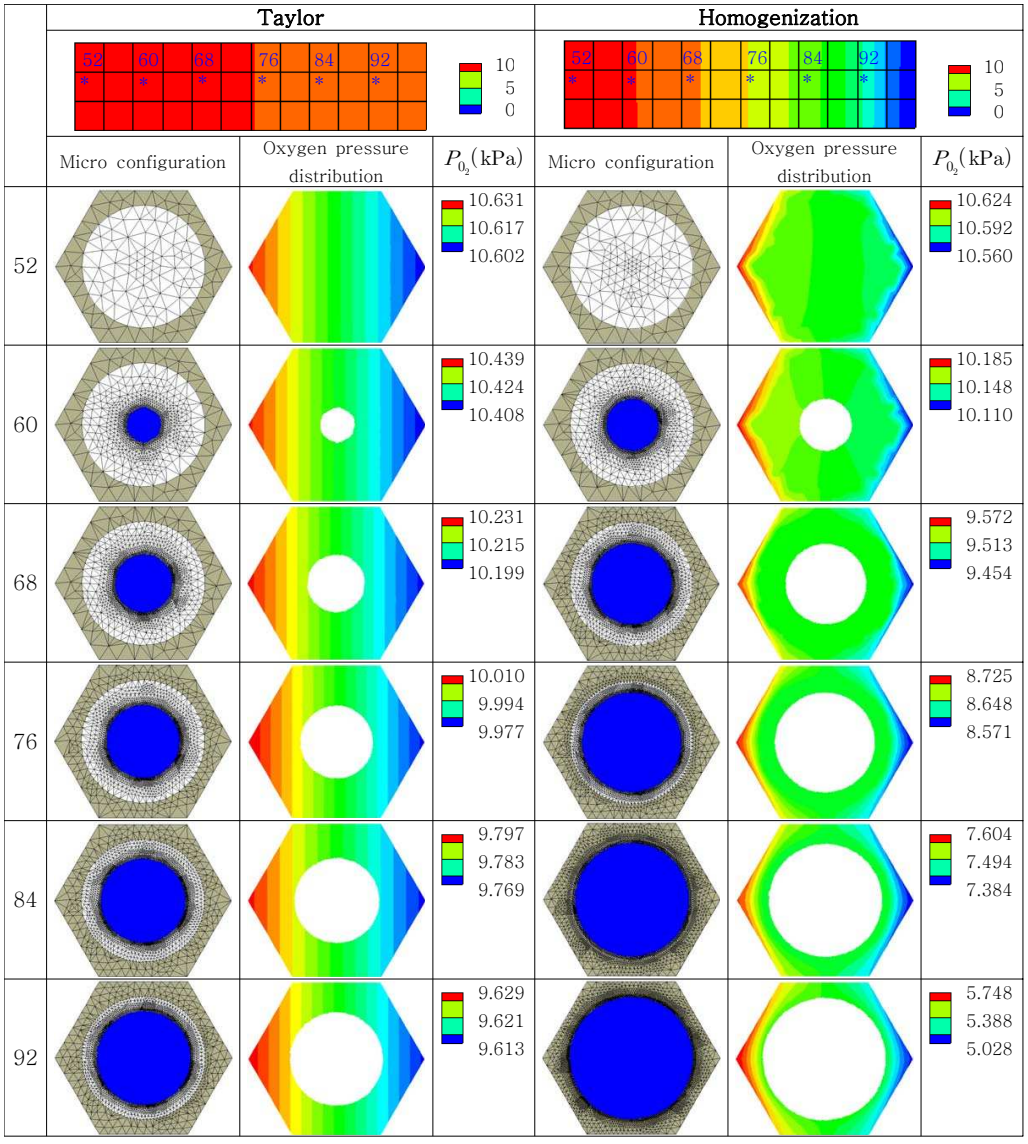

Figure 3.8: *Comparison of carbon fiber configuration and micro–scale oxygen densities for Taylor and homogenization approaches at a simulation time of 25.1 seconds.*

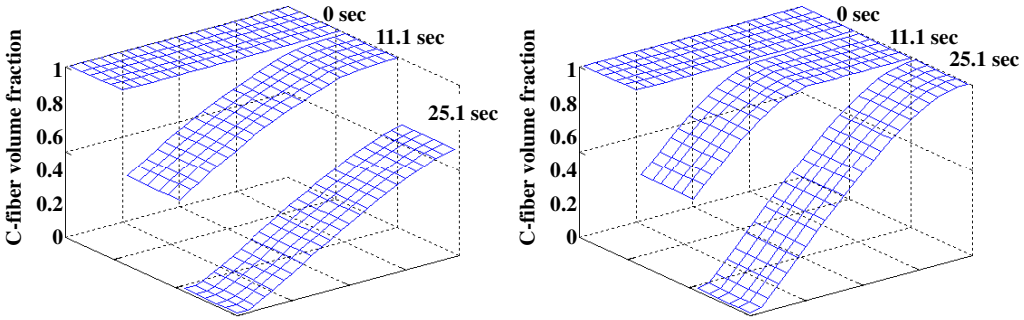

(a) (b)

Figure 3.9: *Spatial distributions of carbon fiber volume fraction at each integration points in macro at 0, 11.1 and 25.1 sec for (a) Taylor and (b) Homogenization model*

CHAPTER IV

Multi-scale model validation with direct numerical simulations(DNS)

[1]In the previous chapter, two different multiscaling approaches (viz. Taylor and Homogenization) methods were directly compared. Lack of analytical models for the complex problem of fiber oxidation prevent us from validating these multiscale approaches directly as was done for the solidification example in chapter 2. Instead, in this chapter, we validate the multiscale model by comparing the homogenization approach with a fully implicit direct numerical simulation.

4.1 Direct numerical simulation

In the direct numerical simulation, micro-scale resolution grids are used to solve the macro–scale problem. This ensures that microstructure dependence is captured directly at the macro-scale albeit with great computational expense. It is expected that multiscaling approaches can give solutions close to what is predicted by a direct numerical simulation. We focus on the problem of oxidation of an assembly of carbon fibers within *a single carbon tow*. The direct numerical simulation(DNS) model is shown in Fig. 4.1 (d). The DNS model has to capture the micro–scale carbon fibers within the tow and thus, involves millions of elements and is clearly more expensive

[1]Reproduced from S Lee and V Sundararaghavan, Validation of Multi-scale model of oxidative degradation of C/SiC composite using direct numerical simulations (DNS), International Journal for Numerical Methods in Engineering, submitted, 2010

than our multi-scale model. The length of the DNS model along the x– axis is $120\mu m$ which implies that 16 fibers were modeled. The corresponding macro–scale models are shown in Fig. 4.1 (b). The micro–scale representative volume element for the multiscale model is shown in Fig. 4.1 (c) with a 7 μm carbon fiber within a hexagonal unit cell. The homogenization approach (rather than the approximate Taylor model) was employed in this study.

The microscopic mass conservation equation is directly solved in the DNS model and is given as:

$$\begin{aligned} \frac{\partial \bar{\rho}_i}{\partial t} + \nabla \cdot \bar{\boldsymbol{q}}_i &= -\nabla \cdot (\rho_i \boldsymbol{v}) \\ \bar{\rho}_i(\Gamma, t > 0) &= \hat{\rho}_i, \quad \bar{\rho}_i(\Omega, t = 0) = \bar{\rho}_{0i} \end{aligned} \tag{4.1}$$

where, $\boldsymbol{q}_i$ denotes the mass flux of species i and ρ_i denotes the partial density of species i, and $\boldsymbol{v}$ represents the velocity of recession of the exposed carbon ($\boldsymbol{v}$ is non-zero only on the evolving interface). The direct numerical model includes both density jump ($[|\rho_i|]$) and flux jump ($[|\boldsymbol{q}_i|]$) for each specie i in the normal direction across the oxidizing interface. The following interface flux condition is used to simulate mass loss of carbon fiber during oxidation:

$$\boldsymbol{q}^+_{O_2} = -\frac{M_{O_2}}{M_C}\rho_c \boldsymbol{v}, \quad \boldsymbol{q}^+_{CO_2} = \frac{M_{CO_2}}{M_C}\rho_c \boldsymbol{v} \text{ on } S^I \tag{4.2}$$

where, ρ_c is the density of the carbon fiber and M_i denotes the molecular mass of species i. The sign in the above equation indicates that oxygen is consumed and carbon dioxide is released at the interface during oxidation.

The constitutive relationships between fluxes and pressure gradients of oxygen and carbon dioxide are derived as shown below (details in section 3.3.1):

$$\begin{aligned} \boldsymbol{q}_{O_2} &= \boldsymbol{\kappa}^{O_2/O_2}\nabla\rho_{O_2} + \boldsymbol{\kappa}^{O_2/CO_2}\nabla\rho_{CO_2} \\ \boldsymbol{q}_{CO_2} &= \boldsymbol{\kappa}^{CO_2/O_2}\nabla\rho_{O_2} + \boldsymbol{\kappa}^{CO_2/CO_2}\nabla\rho_{CO_2} \end{aligned} \tag{4.3}$$

where, $\boldsymbol{\kappa}^{A/B}$ denotes the micro–scale diffusivity relating the mass flux of species A with respect to the pressure gradient of species B and is computed as follows:

$$\begin{aligned}
\boldsymbol{\kappa}^{O_2/O_2} &= -P_{O_2}\frac{1}{\phi\mu_g}\mathbf{k} - \frac{D}{\phi}\boldsymbol{\varphi}^A\frac{P_{CO_2}}{P} \\
\boldsymbol{\kappa}^{O_2/CO_2} &= \frac{M_{O_2}}{M_{CO_2}}(-P_{O_2}\frac{1}{\phi\mu_g}\mathbf{k} + \frac{D}{\phi}\boldsymbol{\varphi}^A\frac{P_{O_2}}{P}) \\
\boldsymbol{\kappa}^{CO_2/O_2} &= \frac{M_{CO_2}}{M_{O_2}}(-P_{CO_2}\frac{1}{\phi\mu_g}\mathbf{k} + \frac{D}{\phi}\boldsymbol{\varphi}^A\frac{P_{CO_2}}{P}) \\
\boldsymbol{\kappa}^{CO_2/CO_2} &= -P_{CO_2}\frac{1}{\phi\mu_g}\mathbf{k} - \frac{D}{\phi}\boldsymbol{\varphi}^A\frac{P_{O_2}}{P}
\end{aligned} \tag{4.4}$$

Two coupled non-linear partial differential equations (Eq. 4.1, one equation each for O_2 and CO_2) are solved using finite element analysis. To solve these non-linear equations, Galerkin finite element method is adopted and the weak form is solved in an incremental iterative manner using the Newton-Raphson method. Level set approach is used to track the degrading interface during FE computations. The mass loss rate of oxygen has been calibrated as an Arrhenius equation using experimental results in [23] and Eq. 3.38 is used to model the interface velocity. We employ the stabilized Galerkin formulation on unstructured adaptive grids for solving the level set equation. In the direct numerical simulation, multiple carbon fiber interfaces are tracked simultaneously using multiple level set functions for each carbon fiber. The numerical implementation of the multi–level set method is same as that detailed in Ref. [74]. The overall solution scheme for the direct numerical model is shown in Table 4.1.

4.2 Computational approach and numerical results

DNS mesh convergence study was performed by considering the volume loss of carbon fibers as the convergence metric. Adaptive meshing (based on unstructured grids) and level set technique is used to track the evolving carbon fiber interface. To

Table 4.1: Solution scheme for direct numerical simulation of carbon fiber oxidation

(1) Initialize FE model for level set method.

(2) Set initial and boundary conditions.

(3) Apply time increment Δt.

(4) Update the carbon fibers using level set method based on the previous time step data.

(5) Obtain new FE model for diffusion from the product of the level set method, and transfer all data.

(6) Set initial guesses for new FE model.

(7) Iteration step:

  (7.1) Assemble the stiffness matrix(Jaccobian) and force vectors.

  (7.2) Solve linearized system and compute residuals.

  (7.3) Compute new guesses.

(8) Check convergence, if not converged go to step 7.

(9) Transfer data from diffusion FEM to level set method. Go to step 3.

test the convergence of this approach, a constant oxygen pressure, $0.1atm$, is applied at every node, and the carbon fiber surfaces were tracked using the level set method. The test results are plotted in Fig. 4.2(b) as a function of number of elements used in the DNS grid. In the figure, it is seen that carbon fiber volume change converges as finer meshes are utilized. The level of mesh adaptivity (or the number of elements) needed for convergence was selected from this preliminary study.

In the 16 fiber tow simulation, an ambient pressure of $P_{O_2} = 0.1atm$ and $P_{CO_2} = 0atm$ for $t > 0$ was imposed on the left end and all other surfaces were insulated (similar to the examples in the previous chapter). The temporal evolution of macro–scale carbon fiber volume fraction is reported for various different macro–scale FE meshes in Fig. 4.3. At the length scales simulated here, the micro–scale meshes become comparable in size to the macro–scale grid. Note that in homogenization approaches, the micro–scale is considered to be much smaller compared to the macro–scale which makes it possible to draw the boundary conditions for the micro–scale

from a single point on the macro–scale. Thus, the use of coarser meshes satisfies the homogenization assumption better. The oxidized carbon volume fraction predicted by both DNS and multiscale model with an 8 element mesh are compared in Fig 4.4(a). The multiscale results show an excellent comparison with DNS approach, although faster oxidation is seen in homogenization approaches with coarser meshes (compare with Fig 4.3(a)). The DNS simulation predicts almost uniform distribution of oxygen volume fraction with a sharp interface separating the oxidized and non-oxidized volumes (Fig 4.4(b)). However, oxygen concentration is smeared in the multiscale model leading to higher oxygen densities in regions to the right of the expected sharp interface. These regions begin to oxidize sooner than expected.

Several selected micro–scale volumes in the homogenized model were also compared with the DNS model directly. Details of the microscopic simulation results from the DNS and multi-scale model are provided in Fig. 4.5. The oxidized carbon volume fractions are shown in Fig. 4.5(b) and Fig 4.5(c), and oxygen pressure contours are shown in Fig 4.5(a) and Fig 4.5(d) at $t = 14.1(sec)$. In (b) and (c), the blue, white, and tan colored areas denote carbon fiber, void(oxidized area), and ceramic matrix respectively. Each carbon fiber in the micro–scale is drawn from a specific point in the macroscopic mesh. Carbon fibers in DNS model are zoomed from regions around these points (shown as blue boxes) in Fig. 4.5. The carbon fiber configurations shown compare reasonably well compared to the DNS simulation. Finally, comparison of computational cost is reported here, and it is concluded at the multi–scale approach provides relatively inexpensive numerical simulations. For the DNS simulation with 16 carbon fibers, the required number of elements is about 400,000 and the computational time is about 3 hours and 43 minutes with 8

processors and parallel computing. However, computational time for the multi-scale homogenization approach is about 1 hour 36 minutes without parallel computation, where 8 and 15,000 elements of macro- and microscopic mesh, respectively, were used.

4.3 Conclusions

Lack of analytical models for the complex problem of fiber oxidation prevent us from validating multiscale approaches directly. Instead, in this chapter, we validated the multiscale model by comparing the homogenization approach with a fully implicit direct numerical simulation. In the direct numerical simulation, micro-scale resolution grids are used to solve the macro–scale problem. This ensures that microstructure dependence is captured, albeit with great computational overhead. We focused on the problem of oxidation of *a single carbon tow* with 16 fibers. The carbon fiber volume fractions predicted by the multiscale model compared well with the direct numerical simulation. In general, based on the homogenization assumption, multiscale simulations with macro–scale meshes that are much larger than micro–scale grids are generally used. As the macro–scale grids becomes coarser, homogenization approaches predict faster oxidation. DNS predicts almost uniform distribution of oxygen pressures with a sharp interface separating the oxidized and non-oxidized volumes. However, oxygen concentration is smeared in the multiscale model leading to higher oxygen densities in regions to the right of the expected sharp interface. These regions begin to oxidize sooner in the multiscale model. In spite of these issues, it is observed that the multiscale model provides reasonable prediction of carbon fiber volume fraction loss with considerably less computational expense. Multiscale modeling is a viable method for simulating oxidation of CMCs with thousands of

carbon fibers, at length scales inaccessible to direct numerical simulations.

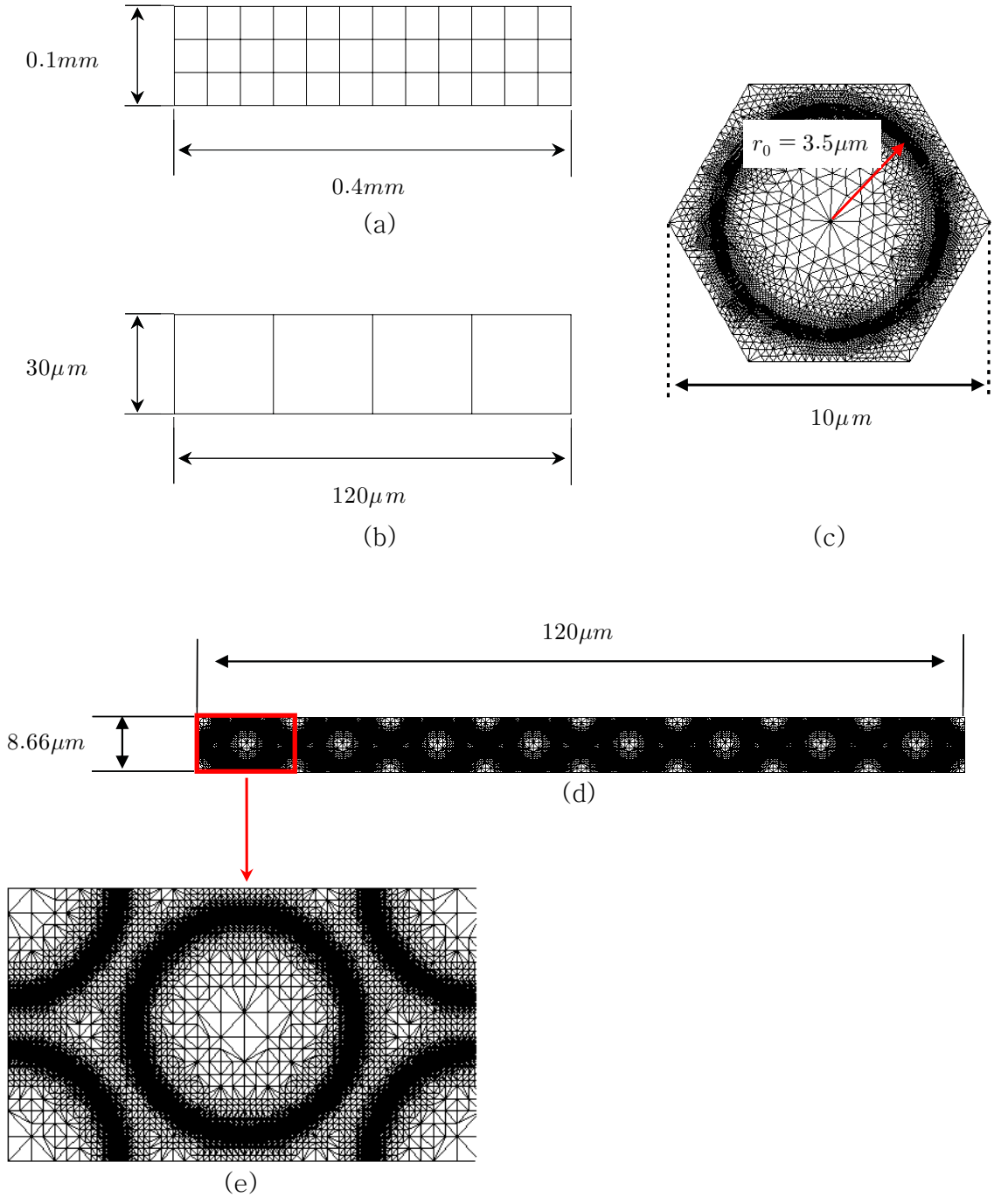

Figure 4.1: *(a) 2D Macro-scale finite element grid (b) 2D Macro-scale finite element grid for validation corresponding to DNS model scale(c) Micro–scale finite element grid (d) Direct numerical simulation finite element grid (e) Larger view of the DNS model over a region indicated by the red box*

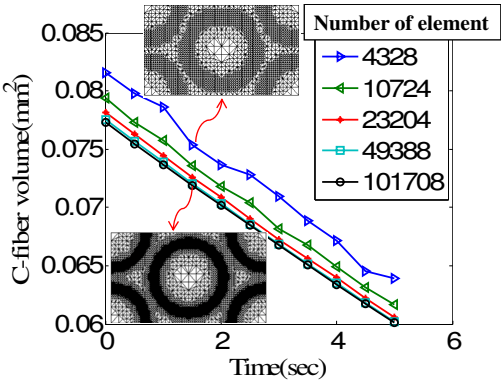

Figure 4.2: *DNS convergence study: DNS models with different levels of adaptive meshing were generated and the convergence of C-fiber volume fraction were tested.*

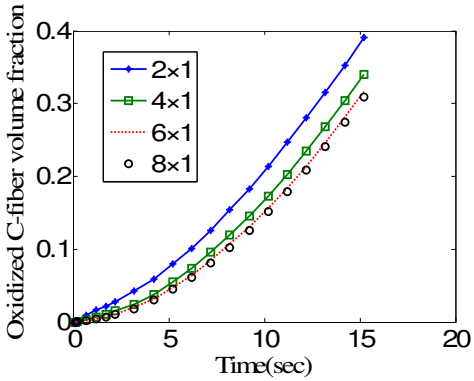

Figure 4.3: *Multi-scale convergence study: Simulations with difference mesh sizes are performed in order to identify the converged macro-scale mesh size. A mesh size of $a \times b$ indicates a elements along x–axis and b elements along the y–axis.*

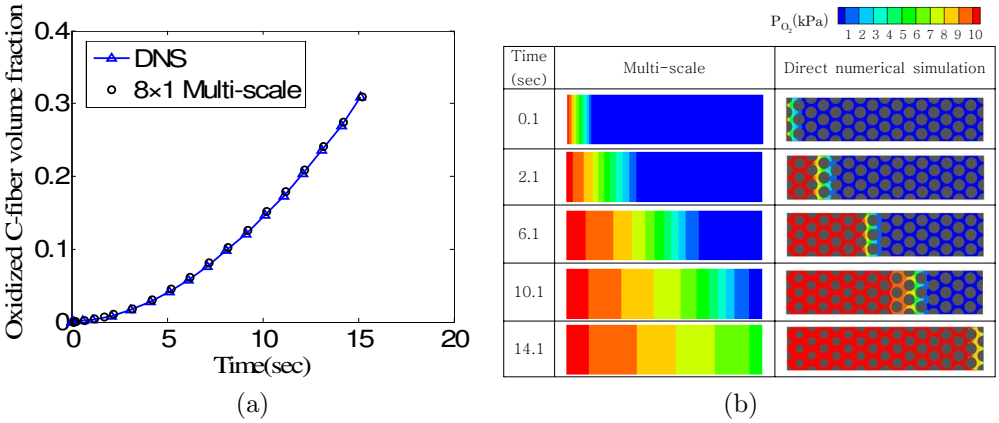

Figure 4.4: *Comparison between DNS and multi-scale simulation results: (a) Oxidized carbon fiber fraction vs. time (b) Oxygen pressure contours at simulation times of 0.1, 2.1, 6.1, 10.1 and 14.1 sec*

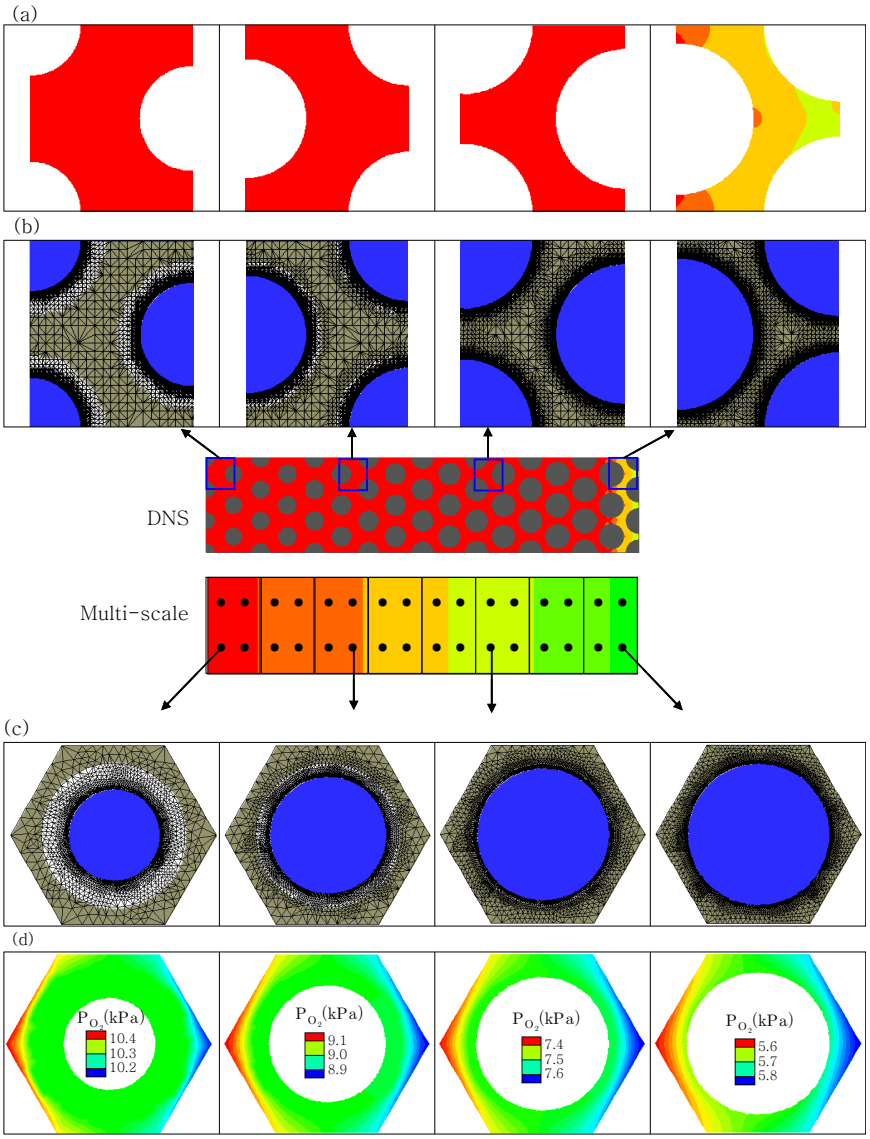

Figure 4.5: *Four selected micro–scale models on the integration points in the macro–grid are compared with the DNS model: (a) and (b) show the micro–scale configuration and oxygen partial pressure, respectively, from DNS approach. Figs (c) and (d) correspond to those from the multi-scale model. Colors blue, white, and tan denote carbon fiber, void, and matrix respectively.*

CHAPTER V

A 3D multiscale model for property degradation of CMCs: Temperature and stress effects

Developments in the previous chapters focused on validation of the multiscale model using a simple tow geometries with few fibers. In real-life applications of CMC components, larger length scales need to be modeled. In particular, woven composites are made up of an intricate weave of carbon fiber tows impregnated with SiC matrix. Each carbon fiber tow may contain thousands of fibers and each component may contain several interwoven tows. In this chapter, we extend our multiscale methodology to address oxidation of complex tow geometries. For model validation, we consider the ceramic matrix composite configuration used in the oxidation experiments at NASA [22]. This composite had a biaxial carbon fiber weave whose geometry was ascertained from SEM images provided in [22]. Steps were taken to reduce the computational expense associated with a full 3D multiscale simulation: (i) Instead of using unstructured meshes adaptive to the carbon fiber tows, we employed a structured FE mesh in the macro-scale. (ii) In addition, a mesh of a representative unit cell (RUC) was created. In the RUC, material indicators were assigned to all the nodes *and* integration points to signify if the point is within a tow or the matrix as shown in the Fig. 5.1 (a). The basic representative unit cell(RUC) geometry is shown in Fig. 5.1(b). The RUC can be periodically translated to generate the composite

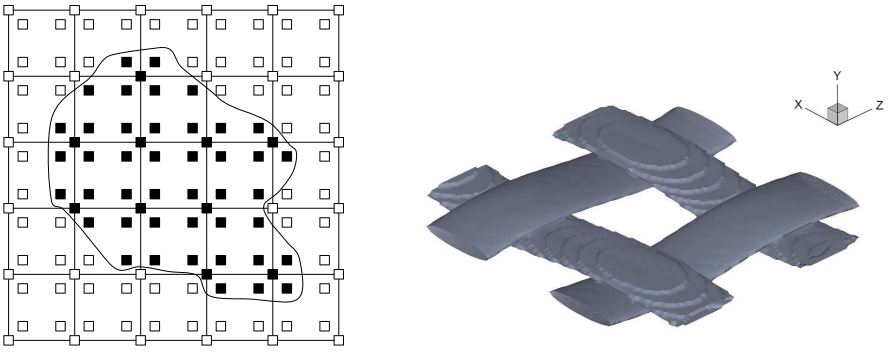

Figure 5.1: *(a) Ceramic matrix and carbon fiber tow are indicated with values 1 and 0 at the finite element nodes and integration points where white box is 1 and black box is 0, (b) Representative unit cell is called to identify the material at any given point in the macroscale mesh.*

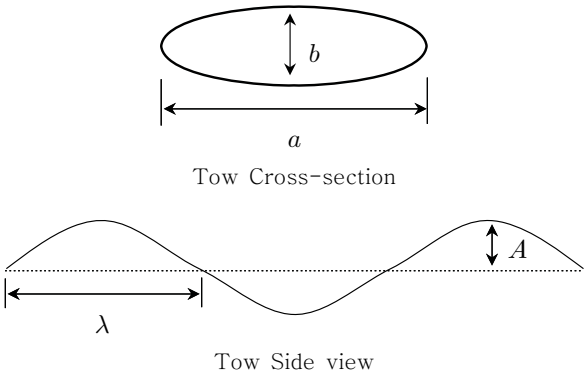

λ	$1.7mm$
A	$0.1mm$
a	$1.2mm$
b	$0.2mm$

Cross sectional dimension

Figure 5.2: *Tow undulation and cross-section dimensions*

structure. The undulation of carbon fiber tow and its cross sectional dimensions for the RUC were computed from SEM images in Ref. [22] and are presented in Fig. 5.2. During simulation of a composite structure, the material indicator corresponding to a location ($\boldsymbol{x}$) in the macro-scale was found by first mapping it to the corresponding point on the RUC, and then, by finding the material indicator assigned to that point. In the FE mesh, additional variables are used to store bias and undulation angles of the carbon fiber.

5.1 Matrix and vector transformation

Although the matrix itself has isotropic properties, the carbon fiber is a transversely isotropic material. It has different properties along the longitudinal and cross sectional plane and the overall mechanical response of the composite depends on fiber configuration. In order to compute degradation in properties (like Young's moduli) during oxidation, it is important to consider the tow undulations and rotate the fiber properties in a local coordinate frame to the global coordinate frame. Let $\boldsymbol{R}_i(\theta)$ denote a rotation with respect to fixed axis, i, through an angle θ. At the level of a carbon fiber, transversely isotropic stiffness is described in the local axes $1-2-3$ as

$$\boldsymbol{D}_f = \begin{bmatrix} D_{11} & D_{12} & D_{12} & 0 & 0 & 0 \\ D_{12} & D_{22} & D_{12} & 0 & 0 & 0 \\ D_{12} & D_{12} & D_{22} & 0 & 0 & 0 \\ 0 & 0 & 0 & D_{44} & 0 & 0 \\ 0 & 0 & 0 & 0 & D_{55} & 0 \\ 0 & 0 & 0 & 0 & 0 & D_{55} \end{bmatrix} \tag{5.1}$$

As shown in Fig. 5.3, biaxial carbon fiber fabric has angles, $\psi = 0$ or $90°$, with respect to global coordinate, $x-y-z$, and undulation angles, θ, known from local axes, $x'-y'-z'$. The rotated matrix in the global reference frame is given as:

$$\bar{\boldsymbol{D}} = \boldsymbol{R}_y^T(\psi)\,\boldsymbol{R}_{z'}^T(\theta)\,\boldsymbol{D}_f\boldsymbol{R}_{z'}(\theta)\,\boldsymbol{R}_y(\psi) \tag{5.2}$$

The rotation matrix for stiffness matrix in cartesian coordinate is given in [55] as:

$$\boldsymbol{R}_y(\theta) = \begin{bmatrix} m^2 & 0 & n^2 & 0 & -2nm & 0 \\ 0 & 1 & 0 & 0 & 0 & 0 \\ n^2 & 0 & m^2 & 0 & 2nm & 0 \\ 0 & 0 & 0 & m & 0 & n \\ nm & 0 & -nm & 0 & -n^2+m^2 & 0 \\ 0 & 0 & 0 & -n & 0 & m \end{bmatrix} \tag{5.3}$$

$$\boldsymbol{R}_{z'}(\theta) = \begin{bmatrix} m^2 & n^2 & 0 & 0 & 0 & 2nm \\ n^2 & m^2 & 0 & 0 & 0 & -2nm \\ 0 & 0 & 1 & 0 & 0 & 0 \\ 0 & 0 & 0 & m & -n & 0 \\ 0 & 0 & 0 & n & m & 0 \\ -nm & nm & 0 & 0 & 0 & -n^2+m^2 \end{bmatrix} \tag{5.4}$$

where $m = \cos(\theta)$ and $n = \sin(\theta)$.

5.2 Computational Homogenization Approach: Micro-scale Boundary Conditions

The multiscale approach for diffusion has already been described in chapter 2 and 3. We purely focus on multiscaling of deformation in this section. To identify

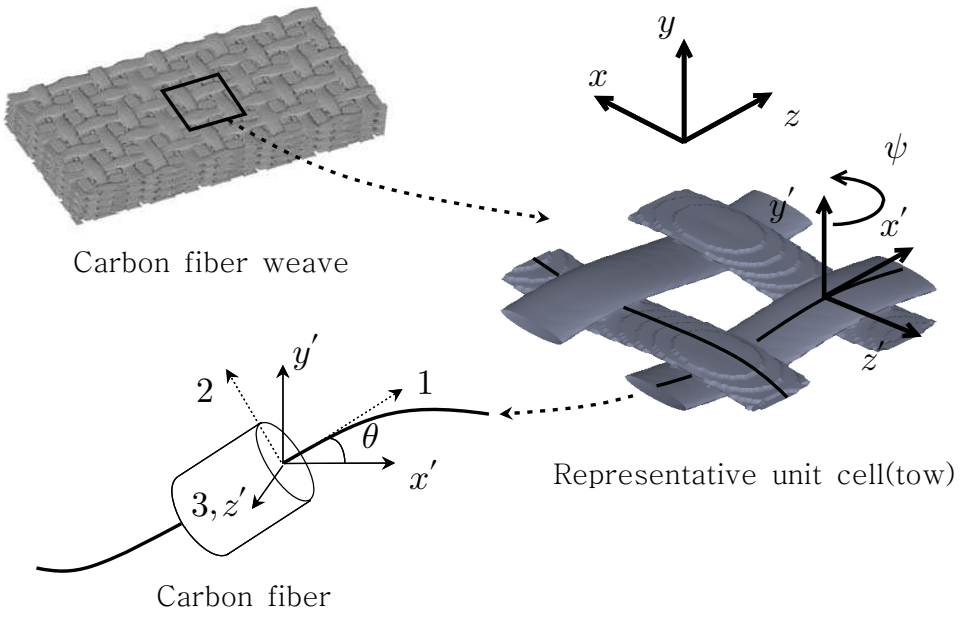

Figure 5.3: *The carbon fiber weave can be described with representative unit cell in which biaxial carbon fiber tows are modeled and the angle ψ denotes directions of carbon fiber tow with respect to $x-y-z$ coordinate system. From the carbon fiber tow, the undulation angle, θ, shows fiber directions with respect to axes $x'-y'-z'$.*

boundary conditions that needs to be employed at the unit-cell level, we employ the computational homogenization approach developed in [70].

Let $\boldsymbol{y} : \mathcal{B}_{ref} \rightarrow \mathcal{B}$ represent the non-linear deformation map of the micro–scale mesh at time t, and $\boldsymbol{F} = \nabla_{ref}\boldsymbol{y}$ the associated tangent map (see Fig. 5.4). $\boldsymbol{F}$ maps points $\boldsymbol{Y} \in \mathcal{B}_{ref}$ onto points $\boldsymbol{y}(\boldsymbol{Y}, t)$ of the current configuration $\mathcal{B}$. The reference microscale configuration is considered of volume $V(\mathcal{B}_{ref})$ and boundary $\partial\mathcal{B}_{ref}$ with outward normal $\boldsymbol{N}$ attached to point $\boldsymbol{X}$ in the macro-continuum ($\boldsymbol{\Omega}_{ref}$). The microstructure at time t of volume $V(\mathcal{B})$ and boundary $\partial\mathcal{B}$ with outward normal $\boldsymbol{n}$ is attached to the material point $\mathbf{x}$ in the macro-continuum $\boldsymbol{\Omega}$ (see Fig. 5.4). We use superposed bars (e.g. $\bar{\boldsymbol{F}}$) to denote macro-scale quantities as before. Voids and cracks are modeled using a damage variable in our model and hence, it is assumed that the geometry is continuous (without cracks).

The most general assumption behind homogenization theory is that the deforma-

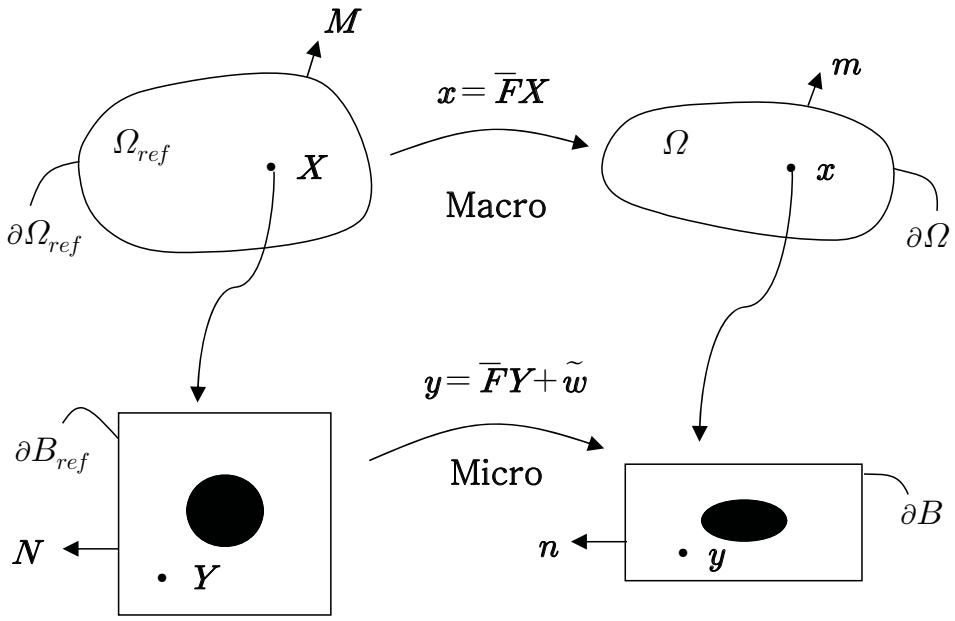

Figure 5.4: *The microstructure homogenization technique: Each integration point in the macro-continuum is associated with an underlying microstructure. The microstructure reference configuration ($\mathcal{B}_{ref}$) and the mapping to the present microstructure configuration ($\mathcal{B}$) are shown in contrast with the homogenized macro-continuum. In total Lagrangian kinematics, $\boldsymbol{X} = \boldsymbol{x}_o$ and $\boldsymbol{Y} = \boldsymbol{y}_o$ are taken from the configurations at time $t = t_o$.*

tion gradient as seen at the macro-scale can be represented purely in terms of the motion of the exterior boundary of the microstructure (see Hill (1972)),

$$\bar{\boldsymbol{F}} = \frac{1}{V(\mathcal{B}_{ref})} \int_{\partial\mathcal{B}_{ref}} \boldsymbol{y} \otimes \boldsymbol{N} dA \tag{5.5}$$

The deformation of the microstructure is then related to the homogenized deformation gradient in the macro-continuum based on the assumption,

$$\mathbf{y} = \bar{\boldsymbol{F}}\mathbf{Y} + \tilde{\mathbf{w}} \tag{5.6}$$

where the deformation consists of a homogeneous part $\bar{\boldsymbol{F}}\boldsymbol{Y}$ and an inhomogeneous part $\tilde{\mathbf{w}}$ referred to as the fluctuation field. As a consequence, we have the relationship, $\boldsymbol{F} = \bar{\boldsymbol{F}} + \tilde{\boldsymbol{F}}$ (with $\tilde{\boldsymbol{F}} = \nabla\tilde{\mathbf{w}}$) between the microscopic ($\boldsymbol{F}$) and the macroscopic ($\bar{\boldsymbol{F}}$) deformation gradients. From the homogenization law (Eq. (5.5)) and the decomposition described above, it can be shown that the superposed field $\tilde{\mathbf{w}}$

follows the equation,

$$\frac{1}{V(\mathcal{B}_{ref})}\int_{\partial\mathcal{B}_{ref}} \tilde{\mathbf{w}} \otimes \boldsymbol{N} dA = 0 \tag{5.7}$$

The condition is satisfied by the use of any one of the three linking assumptions: (1) $\tilde{\mathbf{w}} = 0$ in $\mathcal{B}_{ref}$ (Taylor), (2) $\tilde{\mathbf{w}} = 0$ in $\partial\mathcal{B}_{ref}$ (homogenization), and (3) $\tilde{\mathbf{w}}^{+} = \tilde{\mathbf{w}}^{-}$ (periodic boundary condition).

Macroscopic stress is defined according to a simple virtual work consideration. Here, the variation of the internal work δW_{int} performed by the homogenized PK-I stress tensor $\bar{\boldsymbol{P}}$ at the macroscopic point on arbitrarily virtual displacements of the microstructure $\delta\boldsymbol{y}$ is required to be equal to the work δW_{ext} performed by the external loads on the microstructure. Internal work done by the macroscopic stress can be written as

$$\delta W_{int} = \int_{\mathcal{B}_{ref}} \bar{\boldsymbol{P}}\boldsymbol{\cdot} \nabla_{ref}\delta\boldsymbol{y} dV \tag{5.8}$$

$$= \bar{\boldsymbol{P}}\boldsymbol{\cdot} \int_{\partial\mathcal{B}_{ref}} \delta\boldsymbol{y} \otimes \boldsymbol{N} dA \tag{5.9}$$

External work is given as $\delta W_{ext} = \int_{\partial\mathcal{B}_{ref}} \boldsymbol{p} \cdot \delta\boldsymbol{y} dA$, where $\boldsymbol{p}$ is the traction vector at the boundary of the reference microstructure. For the homogenization boundary condition, the virtual displacements at the boundary of the microstructure are obtained from the variation of the macroscopic deformation gradient as,

$$\delta\boldsymbol{y} = \delta\bar{\boldsymbol{F}}\boldsymbol{Y} \tag{5.10}$$

Thus, the external work can be written as $\delta W_{ext} = \delta\bar{\boldsymbol{F}}\boldsymbol{\cdot} \int_{\partial\mathcal{B}_{ref}} \boldsymbol{Y}\otimes\boldsymbol{p} dA$. For satisfying the balance of virtual work,

$$\begin{aligned}\delta\bar{\boldsymbol{F}}\boldsymbol{\cdot} \int_{\partial\mathcal{B}_{ref}} \boldsymbol{Y} \otimes \boldsymbol{p} dA &= \bar{\boldsymbol{P}}\boldsymbol{\cdot} \int_{\partial\mathcal{B}_{ref}} \delta\boldsymbol{y} \otimes \boldsymbol{N} dA \\ &= \bar{\boldsymbol{P}}\delta\bar{\boldsymbol{F}}\boldsymbol{\cdot} \int_{\partial\mathcal{B}_{ref}} \boldsymbol{Y} \otimes \boldsymbol{N} dA \\ &= \delta\bar{\boldsymbol{F}}\boldsymbol{\cdot} \bar{\boldsymbol{P}} V(\mathcal{B}_{ref})\end{aligned}$$

Taking into account the fact that the equality should be satisfied for any arbitrary variation of the deformation gradient tensor $\delta\bar{\boldsymbol{F}}$, we obtain the macroscopic stresses to be of the form

$$\bar{\boldsymbol{P}} = \frac{1}{V(\mathcal{B}_{ref})} \int_{\partial\mathcal{B}_{ref}} \boldsymbol{Y} \otimes \boldsymbol{p} dA \tag{5.11}$$

An equilibrium state of the micro-structure at a certain stage of the deformation process is then assumed with the equations,

$$\nabla_{ref} \cdot \boldsymbol{P} = 0 \text{ in } \mathcal{B}_{ref} \tag{5.12}$$

$$\boldsymbol{P}^T \boldsymbol{N} = \boldsymbol{p} \text{ on } \partial\mathcal{B}_{ref} \tag{5.13}$$

Using the divergence theorem, macroscopic stresses as defined by Eq. (5.11) can be shown to be the volume-average of the microscopic stresses ($\boldsymbol{P}$)

$$\bar{\boldsymbol{P}} = \frac{1}{V(\mathcal{B}_{ref})} \int_{\mathcal{B}_{ref}} \boldsymbol{P} dV \tag{5.14}$$

Similar result can also be obtained using Hill's macro homogeneity condition (that relates fluxes $\boldsymbol{P}$ and field gradients $\nabla\boldsymbol{u}$):

$$\overline{\nabla\boldsymbol{u}} \cdot \bar{\boldsymbol{P}} = \overline{\nabla\boldsymbol{u} \cdot \boldsymbol{P}} \tag{5.15}$$

According to the Hill's condition, following macroscopic stress can be derived (when using the Taylor model) as:

$$\begin{aligned} \overline{\nabla\boldsymbol{u} \cdot \boldsymbol{P}} &= \frac{1}{V(\mathcal{B}_{ref})} \int_{\mathcal{B}_{ref}} \nabla\boldsymbol{u} \cdot \boldsymbol{P} dV = \frac{1}{V(\mathcal{B}_{ref})} \int_{\mathcal{B}_{ref}} \nabla \left\{ \left(\overline{\boldsymbol{F}} - \mathbf{1}\right) \boldsymbol{Y} \right\} \cdot \boldsymbol{P} dV \\ &= \left(\overline{\boldsymbol{F}} - \mathbf{1}\right) \cdot \frac{1}{V(\mathcal{B}_{ref})} \int_{\mathcal{B}_{ref}} \boldsymbol{P} dV = \overline{\nabla\boldsymbol{u}} \cdot \frac{1}{V(\mathcal{B}_{ref})} \int_{\mathcal{B}_{ref}} \boldsymbol{P} dV \end{aligned} \tag{5.16}$$

The macro stress can be obtained by comparing Eq. 5.16 with Eq. 5.15:

$$\bar{\boldsymbol{P}} = \frac{1}{V(\mathcal{B}_{ref})} \int_{\mathcal{B}_{ref}} \boldsymbol{P} dV \tag{5.17}$$

Apart from these definitions, in macro-problems with temperature effects, the temperature linking is achieved through equating the macro- ($\bar{\theta}$) and micro- (θ) temperatures (and the macro- and micro- mechanical dissipation, if any). Microstructure (material point) simulations are deemed isothermal in this work since the macro-scale temperature evolution problem is not solved.

5.3 Micro–scale model for elasticity

The kinematic problem for microstructure deformation employs the total Lagrangian framework. Here, the total micro-scale deformation gradient $\boldsymbol{F}$ at time $t = t_n$ of configuration $\mathcal{B}_n$ with respect to the initial undeformed configuration ($\mathcal{B}_0$) at time $t = 0$ is assumed to be decomposed as

$$\boldsymbol{F} = \nabla_0 \tilde{\boldsymbol{y}}(\boldsymbol{Y}_0, t_n) \tag{5.18}$$

Going back to Fig.5.4, using the total Lagrangian description of kinematics, $\mathcal{B}_{ref}$ would now refer to $\mathcal{B}_o$. Quantities used in the derivation of homogenized stresses would now be defined with respect to $\mathcal{B}_o$.

The equilibrium equations for the microstructure deformation problem can be expressed in the reference configuration $\mathcal{B}_o$ as,

$$\nabla_o \cdot \boldsymbol{P} = \boldsymbol{0} \tag{5.19}$$

where the PK-I stress $\boldsymbol{P}(\boldsymbol{Y}_o, t)$ is expressed per unit area of $\boldsymbol{B}_o$. The solution of a generic loading increment involves the solution to the principle of virtual work (PVW) given as follows: Calculate $\boldsymbol{y}(\boldsymbol{Y}_o, t)$ such that

$$\int_{\mathcal{B}_o} \boldsymbol{P} \cdot \nabla_o \tilde{\boldsymbol{u}} dV = 0 \tag{5.20}$$

for every admissible test function $\tilde{\boldsymbol{u}}$ expressed over the reference configuration $\mathcal{B}_o$. When using the Taylor model, the displacement increments are specified as $\boldsymbol{u} = (\boldsymbol{F} - \boldsymbol{I})\boldsymbol{Y}$ at every point on the microstructure. The weak form is then solved in an incremental-iterative manner as a result of material non-linearities.

The governing equation can be used for a deformation model presented in Fig. 5.5 in which pore evolution is described during coupled stress-diffusion conditions. Preexisting cracks either close or extend upon mechanical and thermal loading. In the current model, it is included void nucleation and growth as well as void healing due to thermal expansion as studied in [68]. Total deformation resulted in thermal expansion, void, and elastic deformation can be expressed as

$$\boldsymbol{F} = \boldsymbol{F}_e \boldsymbol{F}_v \boldsymbol{F}_\theta \tag{5.21}$$

where, $\boldsymbol{F}_\theta$, $\boldsymbol{F}_v$, and $\boldsymbol{F}_e$ are the deformation gradients representing thermal expansion, void growth, and elastic deformation respectively. $\boldsymbol{F}_v$ is the inelastic deformation gradient attributed to void formation and $\det(\boldsymbol{F}_v)$ can be considered as a measure of internal damage. Damage in the form of void growth comes into play by taking into account the balance of mass for a porous material as

$$\det(\boldsymbol{F}_v) = \frac{1 - \phi_0}{1 - \phi} \tag{5.22}$$

where ϕ_0 and ϕ represent the void volume fractions in the initial and deformed configurations. The functional form for ϕ as a function of stress and temperature is calibrated in the later sections.

Velocity gradient for unstressed isotropic thermal expansion represents thermal part of the deformation as

$$\nabla \boldsymbol{v}_\theta = \dot{\boldsymbol{F}}_\theta \boldsymbol{F}_\theta^{-1} = \alpha \dot{T} \boldsymbol{I} \tag{5.23}$$

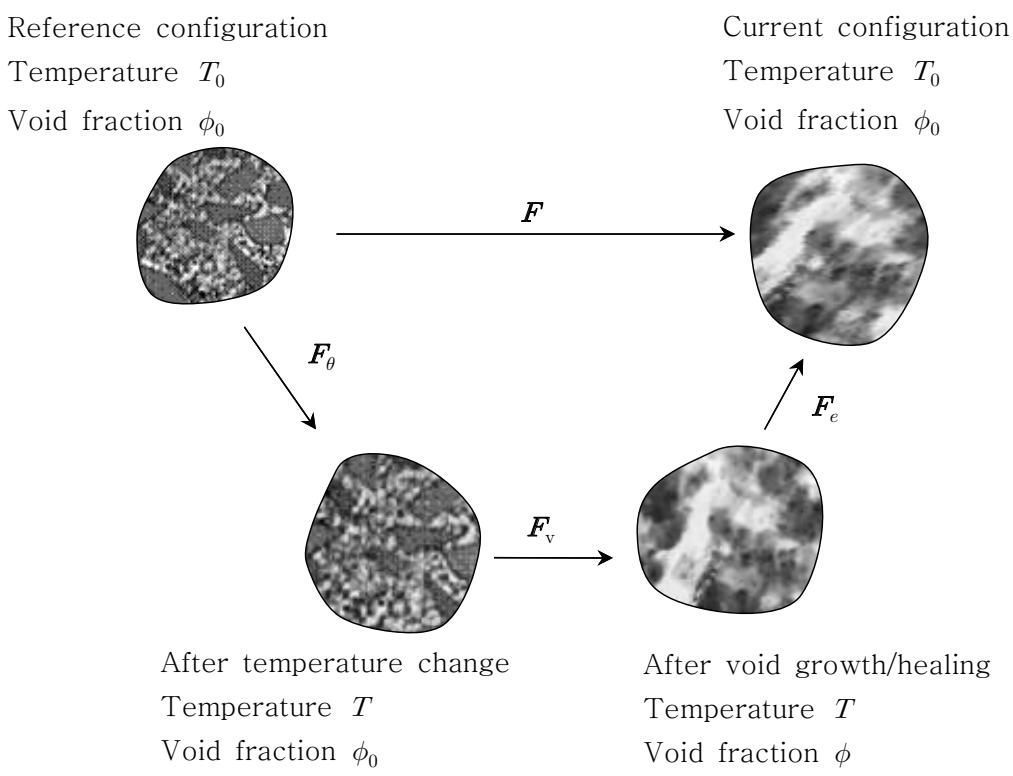

Figure 5.5: *Kinematics coupled with damage evolution in the matrix.*

where, α is coefficient thermal expansion (CTE) and $\boldsymbol{I}$ is the isotropic tensor.

In the case of elastic deformation, the following constitutive relation is considered

$$\boldsymbol{S} = \mathbb{C} : \boldsymbol{E} \tag{5.24}$$

where $\boldsymbol{S}$ and $\mathbb{C}$ are second Piola-Kirchhoff(PK-II) stress and fourth order elasticity tensor respectively. The first Piola-Kirchhoff (PK-I) stress is related to $\boldsymbol{S}$ as $\boldsymbol{P} = \boldsymbol{F}\boldsymbol{S}$. The Lagrangian strain tensor, $\boldsymbol{E}$, is defined in the relaxed unstressed configuration as:

$$\boldsymbol{E} = \frac{1}{2}\left(\boldsymbol{F}_e^T \boldsymbol{F}_e - \mathbf{1}\right) \tag{5.25}$$

The stresses and strains are rewritten in a 6×1 vector format and the 6×6 stiffness matrix is used in subsequent calculations.

$$\boldsymbol{S} = \boldsymbol{D}\boldsymbol{E} \tag{5.26}$$

Different $\boldsymbol{D}$ matrices are used for the matrix, carbon fiber and void: $\boldsymbol{D}_m$ for matrix, $\boldsymbol{D}_c$ for carbon fiber, and $\boldsymbol{D}_v$ for void. Regarding compliance of void, it should be noted that much smaller values are used for void compared to matrix and carbon fiber in order to avoid unexpected numerical stability issues.

5.4 Deformation under mechanical loading

In the finite element solution, Γ_T and Γ_u denote the regions in the initial configuration where traction (T) and displacement boundary conditions, respectively, are applied. We assume that the tractions are explicitly defined on the initial configuration. The finite element weak form for the deformation problem is written as:

$$\boldsymbol{G} = \int_{V(\mathcal{B}_0)} \overline{\boldsymbol{P}} \cdot \nabla \boldsymbol{w} dV - \int_{\partial\Gamma_T} \boldsymbol{w} \cdot T dS = 0 \tag{5.27}$$

where, $\overline{\boldsymbol{u}}$ is the unknown displacement and $\boldsymbol{w}$ denotes the weighting function. The non-linear weak form is solved by adopting Newton-Raphson iteration. Displacement ($\overline{\boldsymbol{u}}^{n+1}$) at $n+1$th iteration is computed as:

$$\overline{\boldsymbol{u}}^{n+1} = \overline{\boldsymbol{u}}^{n} - \boldsymbol{J}^{-1}\left(\overline{\boldsymbol{u}}^{n}\right)\boldsymbol{G}\left(\overline{\boldsymbol{u}}^{n}\right) \tag{5.28}$$

where $\boldsymbol{J}$ is the Jacobian matrix of functional $\boldsymbol{G}$ with respect to $\overline{\boldsymbol{u}}$, and is written as:

$$\boldsymbol{J} = \delta\boldsymbol{G} = \int_{\Omega} \nabla \boldsymbol{w} \cdot \delta\overline{\boldsymbol{P}} dV \tag{5.29}$$

$$\delta\overline{P} = \overline{\mathbb{C}} : \delta\overline{\boldsymbol{F}} \tag{5.30}$$

where $\overline{\mathbb{C}}$ is the fourth order elasticity tensor computed from the microscale model. At the micro-scale, using 5.17, the homogenized 6×6 elasticity matrix for the Taylor

model can be obtained as:

$$\overline{\boldsymbol{D}}_f = \frac{1}{V}\int_V \left(\boldsymbol{D}_m V_m + \boldsymbol{D}_f V_f + \boldsymbol{D}_v V_v\right) dV \tag{5.31}$$

Eq. 5.2 is subsequently used to rotate $\overline{\boldsymbol{D}}_f$ and obtain the homogenized stiffness matrix, $\overline{\boldsymbol{D}}$, corresponding to the particular tow orientation at the macro–scale point.

5.5 Micro–scale Taylor model for O_2 and CO_2 diffusion in porous matrix

In the micro-scale model the following interface flux condition is used to simulate mass loss of carbon fiber during oxidation:

$$\boldsymbol{q}^v_{O_2} = -\varphi^S \frac{M_{O_2}}{M_C}\rho_c \boldsymbol{v}, \quad \boldsymbol{q}^v_{CO_2} = \varphi^S \frac{M_{CO_2}}{M_C}\rho_c \boldsymbol{v} \text{ on } S^{I_2} \tag{5.32}$$

where, ρ_c is the density of the carbon fiber and M_i denotes the molecular mass of species i. In the equation, surface area fraction, φ^S, is introduced to represent pore morphology dependence to the reaction rate as presented in[69]. The sign in the above equation indicates that oxygen is consumed and carbon dioxide is released at the interface during oxidation. The presence of interface flux at the micro–scale leads to a homogenized source term (for oxygen and carbon dioxide densities) in the macroscopic model. The recession speed of the carbon fiber, $\boldsymbol{v}$, depends on temperature and material composition. Because the carbon fiber is initially coated by pyrocarbon, different oxidation rates were used to account for the coating. The reaction rate has a Arrhenius form, assuming that pyrocarbon coating has a larger activation energy compared to the carbon fiber. The rate constant of $6452.32(s^{-1})$ is used for both carbon fiber and the coating. An activation energy of $118.3(kJ/mole)$ is used for carbon fiber [69] and a value of $127.76(kJ/mole)$ is used for modeling the coating.

The mass flux of species within the matrix with volumetric porosity (ϕ) is a result of both pressure gradient driven flow and concentration gradient driven flow. The

net flux is represented as:

$$\boldsymbol{q} = \boldsymbol{q}_i^{\alpha} + \boldsymbol{q}_i^{\beta} \tag{5.33}$$

where $\boldsymbol{q}_i^{\alpha}$ and $\boldsymbol{q}_i^{\beta}$ are the mass flux of species i due to pressure gradient-driven flow and concentration gradient-driven flow, respectively.

The flux contribution within the porous matrix due to pressure gradient driven flow is given by the Darcy's equation as:

$$\boldsymbol{q}_i^{\alpha} = -\rho_i^p \frac{1}{\mu_g} \mathbf{k} \nabla P \tag{5.34}$$

Here, $\rho_i^p = \frac{\rho_i}{\phi}$ denotes the partial density of the species i in the pore. In addition, μ_g denotes the viscosity of the gas mixture, $\mathbf{k} = k\boldsymbol{I}$ ($\boldsymbol{I}$ is the identity matrix) denotes the second-order material permeability tensor and P ($= \sum_i P_i = P_{O_2} + P_{CO_2}$) represents the total pressure of the gas mixture within the pore. The partial pressures (P_i) for each specie i are obtained using the ideal gas law ($\rho_i^P = \frac{M_i P_i}{RT}$, where R is the universal gas constant and T is the temperature). Similarly, the density of the mixture within the pore can be computed as $\rho^p = \frac{MP}{RT}$, where M is the averaged molecular weight of the gas mixture.

The concentration gradient driven mass flux in the porous matrix (based on Ref. [69]) is given using Fick's law of diffusion that involves the second-order areal porosity tensor ($\boldsymbol{\varphi}^A$) which is used as a measure of resistance to concentration gradient-driven flow through the pore network:

$$\boldsymbol{q}_i^{\beta} = -\rho^p D \boldsymbol{\varphi}^A \nabla \left(\frac{\rho_i^p}{\rho^p} \right) \tag{5.35}$$

where D is the diffusivity of oxygen with respect to carbon dioxide. The areal porosity tensor can be thought of as a ratio of porosity to the tortuosity [6]. We employ the calibrated isotropic areal porosity from Ref. [69] for the matrix in the

micro-scale calculations. The oxygen and carbon dioxide density field distributions in the micro–scale are directly obtained from the macro–scale solution using the Taylor boundary conditions (Eq. 3.10). The fluxes at all points within the microstructure are subsequently calculated using Eq. 5.33.

5.5.1 Diffusion properties for pore matrix

As temperature increases, volumetric porosity decreases due to thermal expansion. From the reference temperature, T_0, the expected porosity changing with respect to current temperature, T, is modeled as:

$$\phi_{th} = \lambda_1 \alpha_m \left(T_0 - T\right) \tag{5.36}$$

where λ_1 is a constant estimated via comparing thermogravimetric analysis (TGA) and numerical simulation, and α_m is the matrix coefficient of thermal expansion. However, this equation may give negative porosity when T_0 is greater than T. Moreover, the minimum porosity has an lower bound due to saturation effects. Therefore, the following numerical treatment of porosity is considered.

$$\phi_{th} = \begin{cases} A_1 T^2 + B_1 T + C_1 & 873.15 \leq \quad T \quad < 1073.15K \\ \lambda_1 \alpha_m \left(T_0 - T\right) & 1073.15 \leq \quad T \quad \leq 1223.15K \\ A_2 T^2 + B_2 T + C_2 & 1223.15 < \quad T \quad \leq 1373K \\ \phi_{th}(1373.15K) & 1373.15K < \quad T \end{cases} \tag{5.37}$$

where, equations $A_1 T^2 + B_1 T + C_1$ and $A_2 T^2 + B_2 T + C_2$ are used to smooth transitions. In the above equation, the temperature criterions, $873.15K$ $1373.15K$, are used based on experimental observation [22]. The constants were obtained by

comparing experimental data and numerical simulation results; $\lambda_1 = 526.1$, $T_0 = 1238.5K$, $A_1 = -7.45 \times 10^{-7}$, $B_1 = 1.3 \times 10^{-3}$, $C_1 = -0.1376$, $A_2 = 1.47 \times 10^{-6}$, $B_2 = -4.04 \times 10^{-3}$, and $C_2 = 2.78$. Porosity plots as a function of temperature without the influence of stresses is shown in Fig. 5.6 (a).

Another consideration for the porosity evolution is the effect of externally applied stress. A parametric form of void evolution as a function of hydrostatic stress, $\sigma = \frac{1}{3} tr\left(\boldsymbol{S}\right)$, is assumed in this work. If we assume that the rate of deformation tensor is symmetric and its diagonal quantities are given by hydrostatic stress as $d_{11} = d_{22} = d_{33} = f\left(\sigma\right)$, then, the porosity and stress relation is derived from Eq. 5.22

$$\phi_m = 1 + \left(\phi_{th} - 1\right) \exp\left(-3 \int_0^t f\left(\sigma\right) d\xi\right) \tag{5.38}$$

Considering the fact that porosity cannot be smaller than zero or greater than 1, the following conditions should be satisfied.

$$\begin{cases} \phi_m > 0 & S < 0 \\ \\ \phi_m <= \phi_s & S >= 0 \end{cases} \tag{5.39}$$

where ϕ_s is the saturation porosity and Fig. 5.6 shows stress dependent porosity for different temperature cases: 873.15, 1073.15, 1173.15, and 1223.15 K. The functional form was obtained by comparing numerical simulation with TGA results in [22].

At the microscale, homogenized macro porosity, $\overline{\phi}$, is then written based on the total volume of microscale cell, V, the matrix, V_m, and the void V_v

$$\overline{\phi} = \frac{1}{V}\left(\phi_m V_m + V_v\right) \tag{5.40}$$

In modeling of mass diffusion in a porous matrix at micro–scale as described in [6], an areal porosity parameter representing resistance of consentration gradient

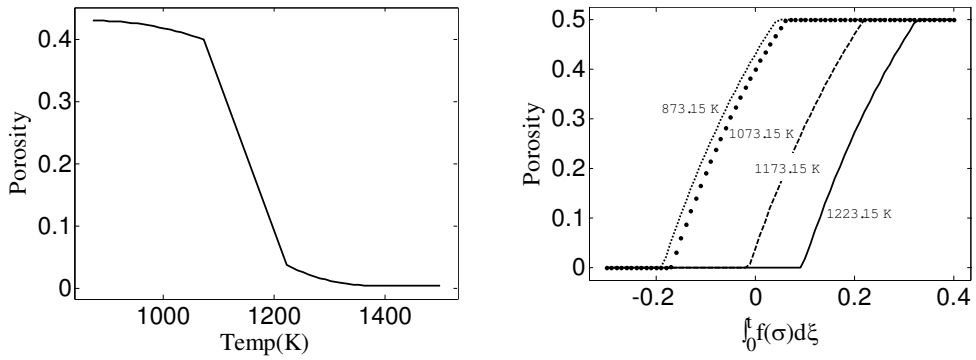

(a) (b)

Figure 5.6: *Predicted (a) porosity vs. temperature curve at zero applied stress (b) porosity curves depended on stress at temperature = 873.15, 1073.15, 1173.15, and 1223.15 K*

driven flow is defined. The quantity is defined as the ratio of volumetric porosity to tortuosity factor κ, as:

$$\varphi^A = \frac{\phi_m}{\kappa} \tag{5.41}$$

Assuming that the matrix is material of packed with spherical particles, the tortuosity factor can be obtained as a function of porosity. As described in [18], the tortuosity factor is τ^2, where τ is the tortuosity which can be computed as [14]

$$\tau = \frac{1}{\phi_m^n} \tag{5.42}$$

Therefore, areal porosity can be estimated as a function of volumetric porosity as

$$\varphi^A = \phi_m^{2n+1} \tag{5.43}$$

where n is determined by the geometric configuration of pores; with $n = 0.4$ used for the spherical particle packing case.

The variation of permeability according to volumetric porosity is further assumed based on the spherical packing of matrix. Based on semi-empirical and semi-theoretical derivation, the relationship between permeability and volumetric porosity

is presented in [41], known as the Kozeny–Carman equation, as

$$\kappa = \frac{d_m^2}{180} \frac{\phi_m^3}{(1-\phi_m)^2} \tag{5.44}$$

where d_m is the mean diameter of particles.

The surface area fraction of carbon fiber open to matrix pores is introduced in [69]. The temperature dependent surface area fraction in that work was very close to an exponential form, as $c_1 \exp(c_2 T)$. Based on this observation, the surface area fraction is modeled as a function of volumetric porosity instead of temperature as the porosity is a linear function of temperature when $1073.15 \leq T \leq 1223.15K$(see Eq. 5.37).

$$\varphi^S = d_1 \exp(d_2 \phi_m) \tag{5.45}$$

However, out of the linear region, since $\phi_{th} = AT^2 + BT + C$, the temperature can be written as:

$$T = \frac{-B \pm \sqrt{B^2 - 4A(C - \phi_m)}}{2A} \tag{5.46}$$

Linearization of the temperature using Taylor expansion and substituting into $c_1 \exp(c_2 T)$ gives exponential functions with different constants.

$$\varphi^S = e_1 \exp(e_2 \phi_m) \tag{5.47}$$

The overall surface area fraction (in the absence of applied stresses) can be written as:

$$\varphi^S = \begin{cases} e_1 \exp(e_2 \phi_m) & 873.15 \leq T < 1073.15K \\ d_1 \exp(d_2 \phi_m) & 1073.15 \leq T \leq 1223.15K \\ f_1 \exp(f_2 \phi_m) & 1223.15 < T \leq 1373K \end{cases} \tag{5.48}$$

where, constants e_1, e_2, d_1, d_2, f_1, and f_2 are determined by use of curve fitting approach with results in [69].

Temperature dependence to air viscosity can be found in [81]. Two approximations, power law and Sutherland law, provide gas viscosity as a function of temperature:

$$\frac{\mu}{\mu_0} = \begin{cases} \left(\frac{T}{T_0}\right)^n & \text{Power law} \\ \frac{\left(\frac{T}{T_0}\right)^{\frac{3}{2}}(T_0+S)}{T+S} & \text{Sutherland law} \end{cases} \tag{5.49}$$

where μ_0 is reference viscosity at a reference temperature T_0, and constant n and S are computed from experimental data.

In order to calibrate the volumetric porosity, 4 tow level multiscale simulation results are obtained for 700, 800, 900, and 950°C and are compared in successive iterations until they match with the TGA data. Based on the achieved volumetric porosity as a main variable, areal porosity, permeability, and surface area fraction are shown in Fig. 5.7 (a), (b), and (c). The constants in this work are listed here: $d_m = 10.0\mu m$, $c_1 = 5.85 \times 10^{-4}$, and $c_2 = 124.8$. Air viscosity verse temperature plot in Fig. 5.7 is obtained based on Sutherland law where the constants for air are used as $\mu_0 = 1.71 \times 10^{-5}\,(Ns/m^2)$ at $T_0 = 273.15\,(K)$, $n = 0.7$, and $S = 110K$.

5.6 Macro-scale model for O_2 and CO_2 diffusion in C/SiC

The macroscopic simulation is performed using a diffusion equation defined on a uniformly meshed domain (Ω) with boundaries defined as Γ. Degrading interfaces are explicitly modeled at the micro-scale, while only homogenized equations are modeled at the macro-scale.

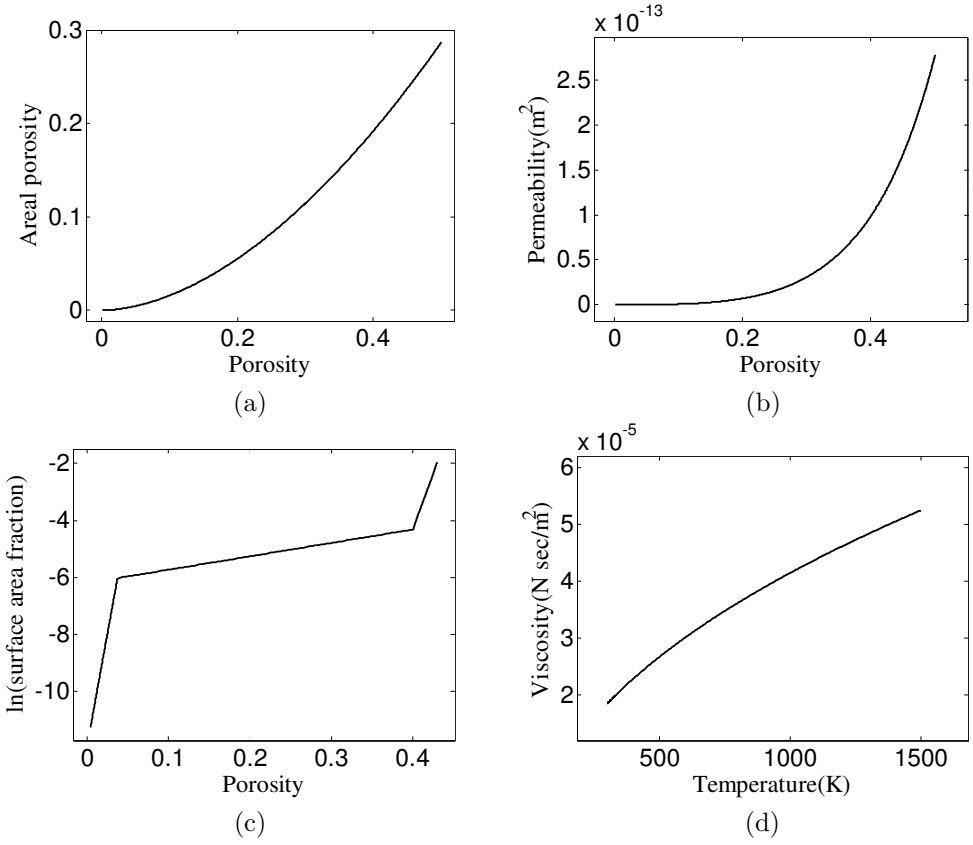

Figure 5.7: *Predicted (a) Aerial porosity, (b) Permeability, (c) Surface area fraction vs. porosity, and air viscosity vs. temperature*

Governing equations for gas species both O_2 and CO_2 are given as:

$$\begin{aligned} \frac{\partial \bar{\rho}_{O_2}}{\partial t} + \nabla \cdot \bar{\boldsymbol{q}}_{O_2} &= \bar{Q}_{O_2} \\ \frac{\partial \bar{\rho}_{CO_2}}{\partial t} + \nabla \cdot \bar{\boldsymbol{q}}_{CO_2} &= -\bar{Q}_{CO_2} \\ \bar{\rho}(\Gamma, t > 0) = \hat{\rho}, \quad \bar{\rho}(\Omega, t = 0) &= \bar{\rho}_0 \end{aligned} \tag{5.50}$$

where, $\bar{\rho}$ is the macroscopic (homogenized) partial density and $\bar{Q}_i$ is the homogenized mass consumption rate of species i per unit bulk volume defined as (where f is the volume fraction of the burnt carbon fiber at the micro–scale):

$$\bar{Q}_i = \rho_c \frac{M_i}{M_c} \frac{\partial f}{\partial t} \tag{5.51}$$

To solve the non-linear transient macroscopic equations (Eq. 5.50), Galerkin finite element method and backward Euler time integration are adopted and the weak form is solved in an incremental iterative manner using the Newton-Raphson method. The $(\lambda + 1)^{th}$ Newton-Raphson step at time $(t + 1)$ involves solution of the system $\boldsymbol{K}\{\delta\bar{\boldsymbol{\rho}}^{\lambda+1,t+1}\} = \boldsymbol{f}$, where the unknown vector in the above system is the increment in the partial density ($\delta\bar{\boldsymbol{\rho}}^{\lambda+1,t+1}$) of oxygen and carbon dioxide. In our numerical approach, the reference density ρ_{ref} and consumption rate $\bar{Q}$ (of each species i) for the next time step are evaluated at the end of each time step of the simulation. The reference density ρ_{ref} is obtained using the macro–micro balance of mass condition ($\bar{\rho} = \frac{1}{V}\int_V \rho dV$) and Eq. 2.1. This definition is consistent with the condition that stored mass at macro-scale is same as the average micro-scale stored mass [36]. To further understand the micro-scale quantities that are needed to create the overall system of equations, the Jacobian matrix and force vector for a finite element e with shape functions N_i occupying a volume Ω^e are expanded below:

$$K_{ij}^{t+1,\lambda} = \begin{bmatrix} \frac{1}{\triangle t}\int_{\Omega^e} N_i N_j dV - \int_{\Omega^e} \frac{dN_i}{dx_p} \bar{\kappa}_{pq}^{O_2/O_2} \frac{dN_i}{dx_q} dV & -\int_{\Omega^e} \frac{dN_i}{dx_p} \bar{\kappa}_{pq}^{O_2/CO_2} \frac{dN_i}{dx_q} dV \\ -\int_{\Omega^e} \frac{dN_i}{dx_p} \bar{\kappa}_{pq}^{CO_2/O_2} \frac{dN_i}{dx_q} dV & \frac{1}{\triangle t}\int_{\Omega^e} N_i N_j dV - \int_{\Omega^e} \frac{dN_i}{dx_p} \bar{\kappa}_{pq}^{CO_2/CO_2} \frac{dN_i}{dx_q} dV \end{bmatrix}$$

$$f_i^{t+1,\lambda} = \begin{bmatrix} -\int_{\Omega^e} N_i \frac{\bar{\rho}_{O_2} - \bar{\rho}^t_{O_2}}{\triangle t} dV + \int_{\Omega^e} \frac{dN_i}{dx_p} \bar{q}_{O_2 p} dV + \int_{\Omega^e} N_i \bar{Q}^t_{O_2} dV \\ -\int_{\Omega^e} N_i \frac{\bar{\rho}_{CO_2} - \bar{\rho}^t_{CO_2}}{\triangle t} dV + \int_{\Omega^e} \frac{dN_i}{dx_p} \bar{q}_{CO_2 p} dV + \int_{\Omega^e} N_i \bar{Q}^t_{CO_2} dV \end{bmatrix}$$

From the above equations, it is seen that homogenized diffusivities $\bar{\boldsymbol{\kappa}}^{A/B}$ relating the mass flux of species A with respect to the pressure gradient of species B needs to be defined at each integration point in the macro-scale. The evaluation of the homogenized diffusivity for Taylor and Homogenization approaches are listed below: In the Taylor model, the diffusivity is directly obtained as:

$$\bar{\boldsymbol{\kappa}}^{A/B} = \frac{1}{V}\int_{\Omega} \boldsymbol{\kappa}^{A/B} dV \tag{5.52}$$

5.7 Computational approach and numerical Examples

3D oxidative carbon fiber reinforced ceramic matrix is simulated with the multi–scale finite element model. In the first few examples, stress–diffusion coupling was not enforced. Instead the mechanical properties of the oxidized fibers were computed directly from the oxidized tow system by imposing a stress boundary condition along the z– axis and measuring the strains along different direction. The results have also been compared to the elastic moduli degradation computed using a volume averaged stiffness matrix at the tow level. The domain for the simulation and boundary conditions are explained in Fig. 5.8. Initially, the C/SiC coupon is saturated with 1

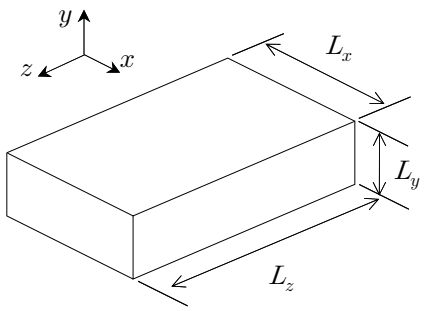

Boundary conditions

		Diffusion only	Stress, diffusion coupled
Dimension(cm)	:	$L_x = 1.02,\ L_y = 0.33,\ L_z = 1.27$	$L_x = L_z = 1.02,\ L_y = 0.33$
$z = L_z$	:	$\boldsymbol{PN} = 0$	$\boldsymbol{PN} = \boldsymbol{T}(t)$
$x = y = z = 0$	:	$\boldsymbol{u} = 0$	
$x = 0,\ x = L_x$	:	$P_{O_2} = 1\,atm,\ P_{CO_2} = 0\,atm$	
$z = 0,\ z = L_z$	:	$P_{O_2} = 1\,atm,\ P_{CO_2} = 0\,atm$	Insulated
$y = 0,\ y = L_y$	:	Insulated	

Initial conditions

$t = 0$	:	$\boldsymbol{u} = 0$ $P_{O_2} = 1\,atm,\ P_{CO_2} = 0\,atm$

Figure 5.8: *Numerical simulation model: Geometry, initial and boundary conditions*

atm carbon dioxide. Subsequently, the system is exposed to 1 atm oxygen along the x- and z- axis. Insulation conditions take placed at top and bottom of the coupon, and the composite is subjected to a uniaxial tension on the face at $z = 1.27cm$; applied stress reaches up to $172MPa$ within 2.5 minutes. The displacement constraints allows that body can slide on the faces at $x = 0$, $y = 0$, and $z = 0$.

The solution schemes based on the multi–scale Taylor model is described in Table 5.1 and the material constants used are listed in Table 5.2: Young's moduli E, Poisson's ratio, and coefficient of thermal expansion α. The properties are based on local coordinate system, 1-2-3 axes as shown in Fig. 5.3, and moduli are given in GPa and coefficient of thermal expansion is in $1/K$ units.

To aid in speeding up the solution process for the multi–scale problem, the al-

gorithm was parallelized using MPI. The macro-scale domain was decomposed and elements in each domain distributed to different processors. The underlying micro-scale problems were solved in serial in each processor. The simulator was developed using object oriented programming and was dynamically linked to the parallel toolbox PetSc [8] for parallel assembly and solution of linear systems. For solution of linear systems, a GMRES solver along with block Jacobi and ILU preconditioning from the PetSc toolbox was employed.

5.8 Numerical simulation results

Grid size sensitivity is critical to validate the simulation model. Based on our structured mesh at the macroscale, convergence study was performed with FE grids whose element sizes are decreased until simulation results converged. The macro–scale FE mesh density was determined by this grid convergence strategy. For the convergence study, O_2 and CO_2 diffusion was simulated under a temperature of 800°C without any externally applied stress. The simulation is performed up to 2.5 hours and carbon fiber loss at this time is recorded as a function of number of element in the FE mesh. A 5760 element macro-mesh was selected based on the convergence study. The graph in the Fig. 5.9 (a) indicates the carbon fiber volume loss versus the number of elements, and the result shows the convergence of simulation results as finer meshes are used. A hexagonal unit cell 3D microscale model is employed in this study. Note that the micro–scale volume has a fixed coordinate system and is not rotated based on the tow orientation. Instead, the fields and fluxes at the tow level are rotated to the micro–scale coordinate system and imposed on the microscale unit cell.

In the next simulation, oxidative diffusion results were compared directly with

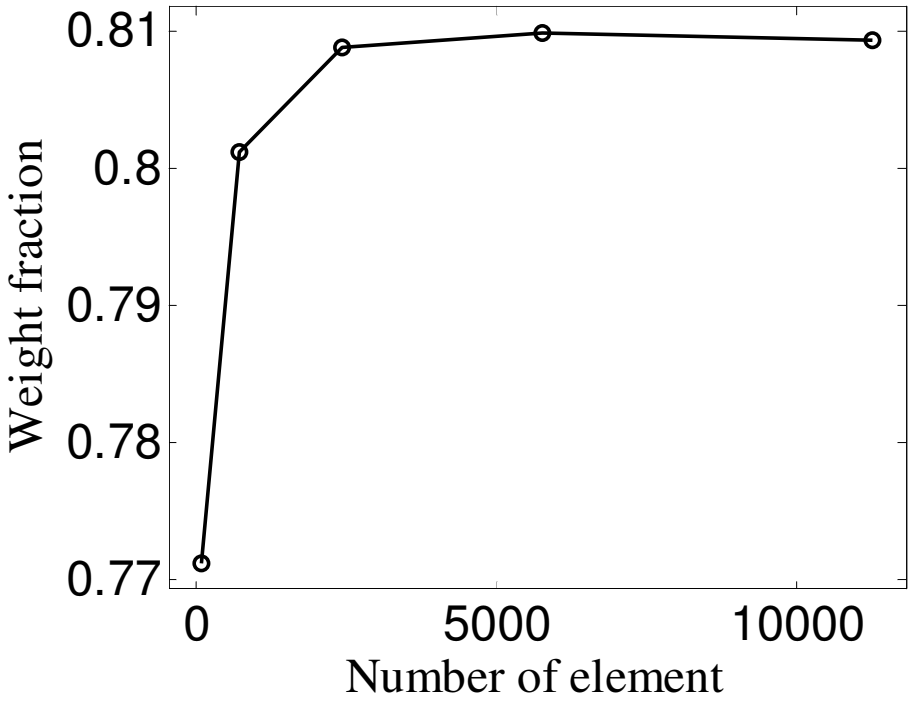

Figure 5.9: *Macro model grid convergence; Simulation shows the carbon fiber volume change at 2.5 hours and at* 800°C *as a function of number of elements used in the macro–scale mesh.*

TGA experiments. Note that we use a material indicator to denote if a point is in the fiber region of tow region and then a micro–scale cell is drawn from that point. The use of structured grids is not optimal for capturing the curvature of the tows. However, using material indicators the curvature can be accounted for reasonably well during the entire composite simulation. Numerical simulation of O_2 and CO_2 diffusion simulation was performed on the structured macro–scale grid and results are compared with TGA experiments at several different temperatures. The initial composite had 50 % carbon by weight. Predictions of carbon fiber loss at various temperature and times are shown in the Fig. 5.10, and the comparison reveals that the 3D FE model can indeed demonstrate the experimental observations of carbon fiber oxidation trends successfully.

Several interesting oxidation behaviors were observed from these simulations. Ox-

idation is most severe at 700°C. At this temperature, presence of high porosity (due to lower temperature) and moderately high reaction rates (note that reaction rates depend on temperature through Arrhenius equation), lead to a high oxidation rate. As temperature decreases, the oxidation begins to follow a sigmoidal curve (note the curve at 600°C in Fig. 5.10). At lower temperatures, the porosity is higher, leading to faster diffusion. However, the reaction rates are lower leading to a weight loss behavior that is controlled by the speed of chemical reaction rather than the diffusion rate. The porosity at 600°C and 700°C were not much different, hence the reason for the sigmoidal curve observed at 600°C was inferred to be due to the combined influence of reaction controlled kinetics and the presence of the pyrocarbon coating on the carbon fiber. Once the coating is consumed, the reaction rates become faster and follows similar trends observed at 700°C. As temperature increases, the weight loss drastically drops. At 700°C complete oxidation is seen at 8 hours. However, at 950°C, only a fraction of the carbon fiber is consumed even after 25 hours. The reason for this behavior is the decreased porosity at higher temperatures. As temperature increases, the matrix expands and the pores close, leading to a weight loss behavior that is controlled by the availability of oxygen rather than the reaction rate. Another interesting behavior is seen at very high temperatures. The weight loss rates begin to increase at 1100°C. Simulations reveal that the behavior is due to porosity saturation at 1100°C. Beyond 1100°C, the volumetric porosity reaches saturation and is not affected by an increase in temperature. However, the reaction rates increase leading to faster oxidation. It is seen that at 1250°C and 1400°C the oxidation rates show a different kind of parabolic behavior with increased oxidation rate as time progresses (instead of decreased rate of oxidation as a function of time at lower temperatures). This behavior is well captured by our simulations.

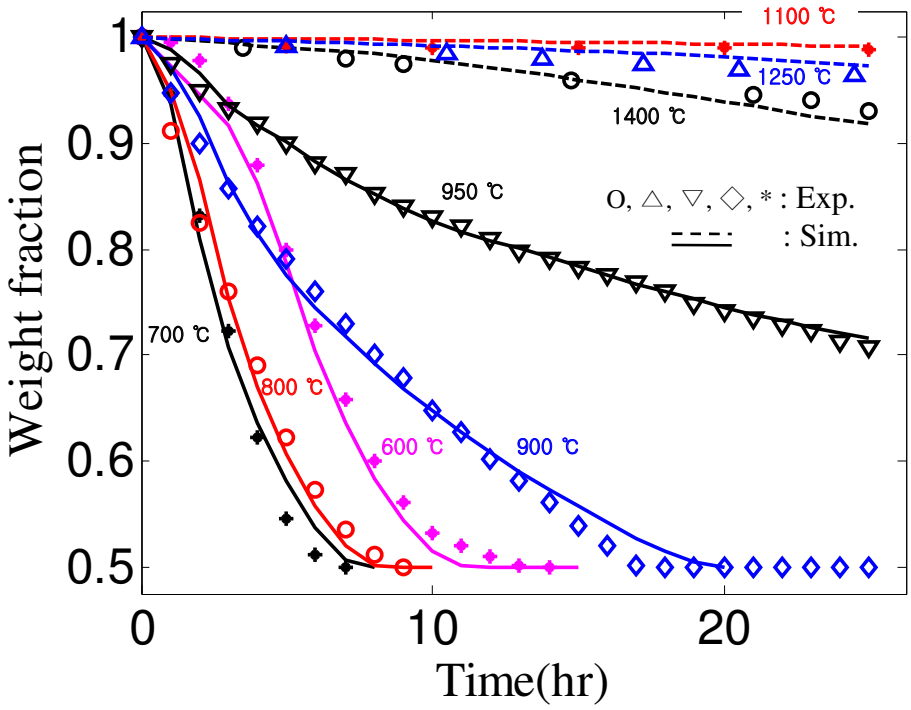

Figure 5.10: *Percent weight fraction remaining: Simulation results are directly compared with thermogravimetric analysis at different temperatures.*

As a measure of mechanical degradation of the composite, we computed the variation of Young's modulus of the composite (along the z– direction) as a function of temperature. During mechanical testing, small loads were applied to compute the elastic response (ie. Young's modulus) and thus, stress–diffusion coupling and porosity changes due to these stresses were not modeled. The mechanical properties of the oxidized fibers were computed directly from the oxidized tow system by imposing a stress boundary condition along the z– axis and measuring the strains along different direction. The results have also been compared to the elastic moduli degradation computed using a volume averaged stiffness matrix at the tow level. When using the volume averaged stiffness matrix, the following equation is used to find the elastic moduli (where the averaged D matrix $\bar{D}$) computed at the micro–scale; matrix is rotated based on the tow orientation and the quantity is volume averaged over the

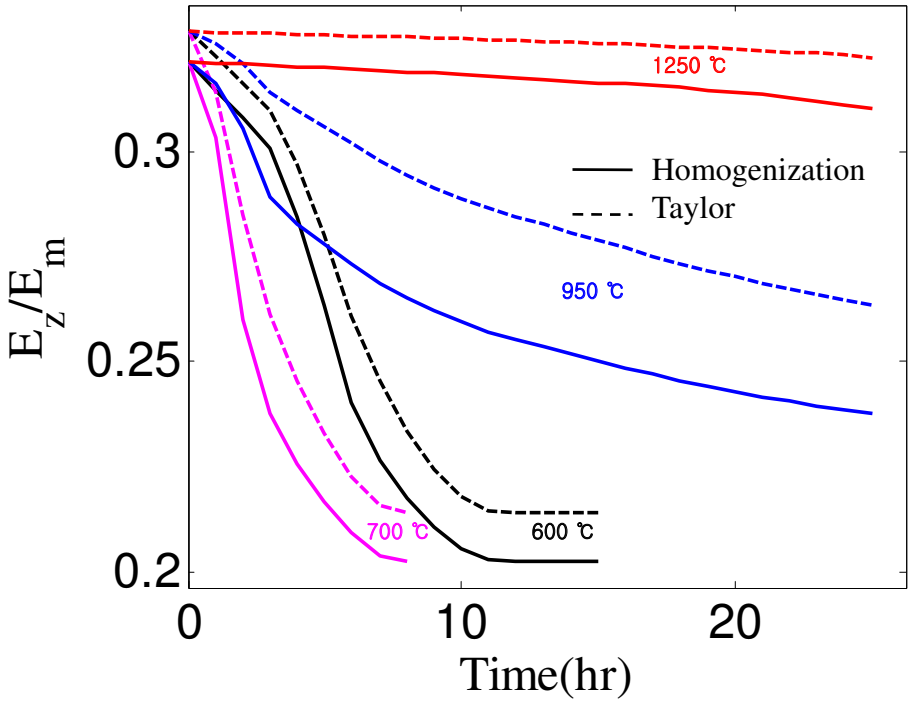

(a) (b)

Figure 5.11: *Young's modulus in z direction is predicted at different temperatures and times using Finite element homogenization (solid line) and Taylor(broken line) approaches.*

macro–scale ($< . >$ indicates a volume average):

$$E = \frac{1}{< \bar{D}^{-1} >_{11}} \tag{5.53}$$

The above equation is used in Taylor type multiscale models and is known to give a upper bound response. As shown in Fig. 5.11, the Taylor model predict a stiffer response. The homogenization approach (finite element study) shows that the mechanical degradation follows trends similar to that of overall oxidation. Note that in the plot, the overall modulus is given in the form of a ratio with respect to the matrix moduli.

Next, we studied the overall evolution of oxygen partial pressure at the tow level and the results are shown in Fig. 5.12. All these plots use the same oxygen pressure contour levels for easier comparison. At lower temperatures oxidation is much faster

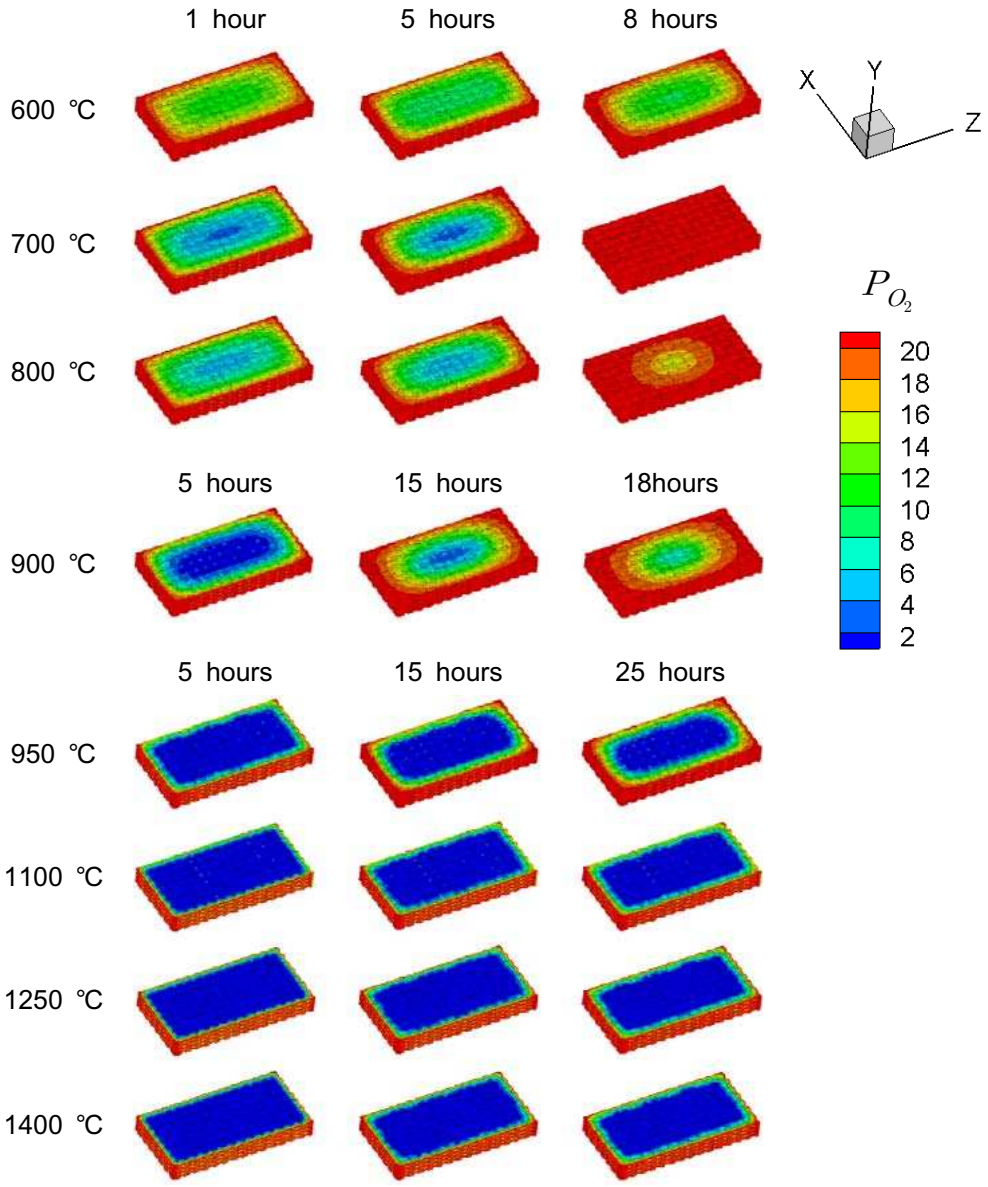

Figure 5.12: *Oxygen pressure distributions at 600*°C*-1400*°C

and hence, the table is split into a lower temperature regime with results shown at 1, 5 and 8 hours, and a higher temperature regime with results shown at 5, 15, 18 and 25 hours. At lower temperatures, the porosity is high and the oxygen pressures are more uniformly distributed. At higher temperatures, the porosity is extremely low and the diffusion (and oxidation) occurs at the outer edge of the model with negligible oxidation in the interior. Over time, the boundary between the oxidized and non-oxidized regions move inward leading to the so-called 'shrinking core' oxidation behavior reported in experiments[76]. In the lab experiment reported in [76], a constant-load rupture test was performed at 800°C and 1200°C. The temperature at which the oxidation behavior transitions from uniform pattern to a shrinking core pattern was seen to be between 700°C and 950°C in the TGA experiment, whereas the transition temperature was between 800°C and 1200°C in stressed–oxidation tests. The reason that the transition temperature is higher in stressed oxidation test is because tensile stresses tend to increase the porosity and thus, increase diffusion rates at higher temperatures. The carbon fiber volume fraction lost in the lower temperature regimes are plotted in Fig. 5.13. These are shown as 2D plots with carbon fiber volume fractions averaged along the depth of the tow (along y– axis). The inhomogeneity in carbon fiber distribution due to complex nature of tow weave results in a seemingly noisy distribution of carbon fibers in the composite. At 600°C, after 5 hours, the oxidation is seen to be uniformly spread over the entire tow area. However, the shrinking core behavior is clearly seen at higher temperature regimes (shown in Fig. 5.14). It is seen that oxidation at 950°C is faster than oxidation at 1400°C due to higher porosity at lower temperatures. Further, it is also seen that oxidation at 1400°C is in fact faster than 1250°C due to porosity saturation.

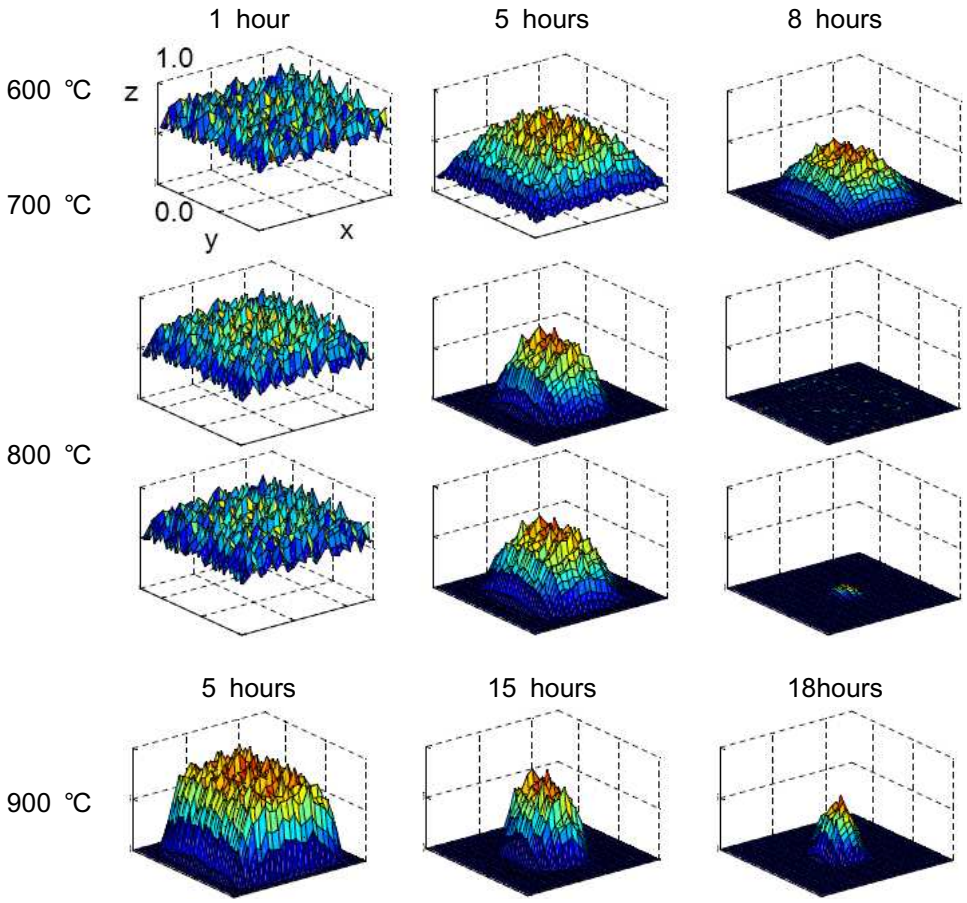

Figure 5.13: *Spatial distribution of carbon fiber volume fraction at* 600°C - 900°C

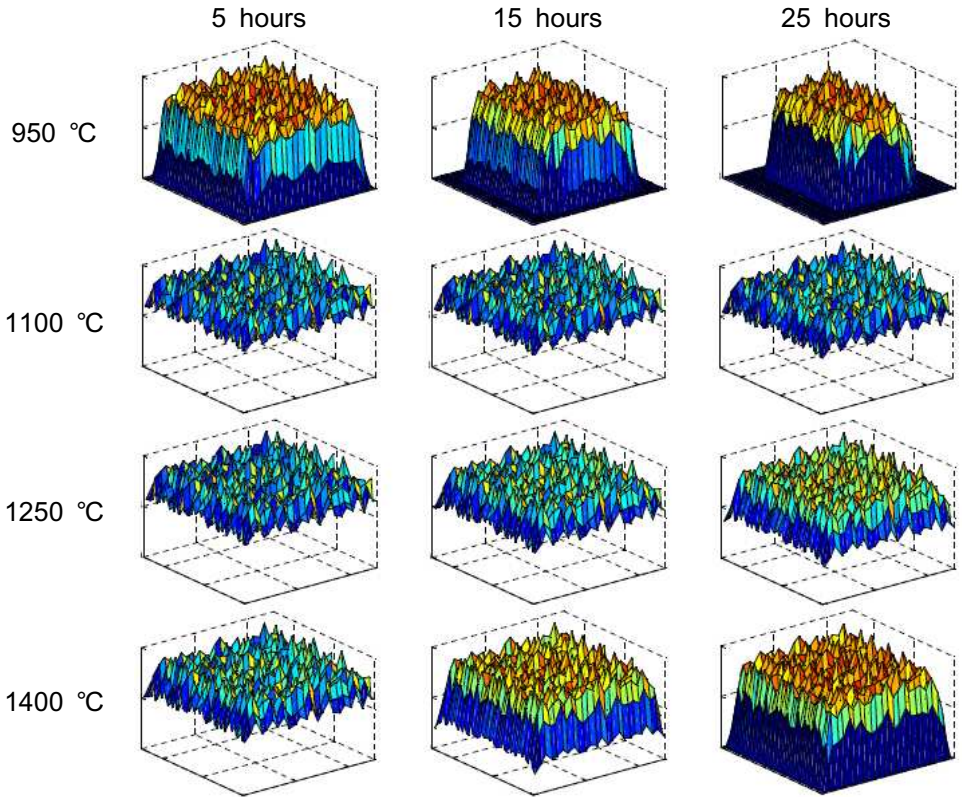

Figure 5.14: *Spatial distribution of carbon fiber volume fraction at* 950°C - 1400°C

5.8.1 Comparison of oxidation behavior in the presence of applied stresses

As a preliminary study, a multi–scale simulation is performed in which stress-diffusion coupled degradation of the carbon fiber is studied for three cases at 1000°C: (i) stresses applied in an inert atmosphere (ii) oxidation in the absence of applied stresses, and (iii) stresses applied during oxidation. These three simulations were compared to identify the coupled effects of oxidation and stress. The comparisons are shown in Fig. 5.15 where (a) shows time vs. strain curves, and (b) denotes the loss of the volume fraction of the carbon fiber. In the tensile test, the following functional form of rate of deformation in terms of hydrostatic stress ($\sigma = \frac{1}{3} tr\,(\boldsymbol{S})$) was employed based on experimental observations in [59].

$$d_{11} = d_{22} = d_{33} = \lambda \sigma^n \tag{5.54}$$

Curves in Fig. 5.15 (a) compares simulation results for two boundary conditions, 1 atm inert gas and 1 atm air, respectively as boundary conditions. In this simulation, uniaxial tension is applied until its value reaches 172MPa and the specimen is then held at 172MPa. The solid line denotes TGA result reported in [22], and solid lines with circle and star show simulation results for 1 atm air and inert gas boundary conditions, respectively. The simulation result in the oxidizing environment is compared with the experiment result (TGA) and shows a good match with experimental trends. It is seen that mechanical stiffness is decreased (or strain increases for the applied constant stress: creep behavior) when the composite is exposed to air at high temperature. Comparing with the results from the case with no oxidation, it is concluded that the loss of carbon fibers is the main cause for the degradation in mechanical properties.

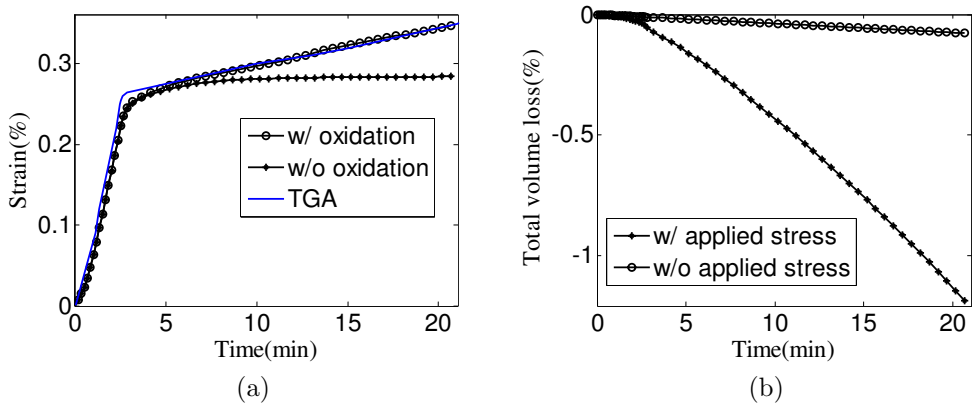

(a) (b)

Figure 5.15: *(a) Strain vs. time; solid line shows TGA experiment results (solid lines with circle and star denote simulation results for 1 atm air and inert gas environment cases respectively). (b) Total volume losses in the composite (solid lines with circle and star denote no stress applied and stress applied respectively)*

In Fig. 5.15 (b), the simulation results for the unstressed case and the case with applied stresses are compared. Comparison of the two plots show that presence of stresses can significantly increase carbon fiber oxidation. In the presence of tensile stresses, the pores expand and increased volume of oxygen becomes available in the interior. The increased porosity accelerates burn up of the carbon fibers, and loss of the fibers decreases the stiffness of the composite. This causes the loads to be concentrated on the matrix and results in even more damage. A combination of these events is termed 'stress oxidation' coupling which leads to rapid degradation of CMCs.

5.9 Conclusion

A multi–scale framework based on computational homogenization is developed for modeling thermo-chemo-mechanical oxidation at the length–scale of a interwoven tow based composite structure. At the micro-scale, oxidation at the scale of individual carbon fibers is modeled using a hexagonal unit cell, and homogenized material properties are transferred to the macro-scale model. In order to couple the

macro–scale and micro–scale simulation, the fields and flux quantities for the oriented tows are appropriately rotated and assigned to the micro-scale mesh. At the micro–scale, physical mechanism of carbon fiber mass loss was computed based on diffusion of oxygen in the porous SiC matrix, reaction and surface recession on the carbon fibers. The overall degradation of the composite is computed by employing a 3D structured FE mesh containing a material indicator for the carbon fiber tow and the matrix. In the FE mesh, additional variables are used to store bias and undulation angles of the carbon fiber. In order to couple stress and diffusion, a damage model was developed that provides the volumetric porosity in the material as a function of stress and temperature. The diffusion properties implicitly depend on the volumetric porosity through various functional forms developed in this work. The validation of the 3D oxidation model of the composite is performed by comparing with TGA experiment results from [22]. A variety of transition behaviors were successfully reproduced. Oxidation was found to be most severe at 700°C. As temperature decreases, the oxidation begins to follow a sigmoidal behavior with slow initial oxidation followed by faster oxidation. The reason for the sigmoidal curve observed at 600°C was inferred to be due to the combined influence of reaction controlled kinetics and the presence of the pyrocarbon coating on the carbon fiber. At higher temperatures the oxidation rate is slower due to decreased porosity. As temperature increases, the matrix expands and the pores close, leading to a weight loss behavior that is controlled by the availability of oxygen rather than the reaction rate. Another interesting behavior is seen at very high temperatures. The weight loss rates begin to increase at 1100°C due to porosity saturation. Further, the shrinking core oxidation behavior at these high temperature, as observed in experiments, are well captured by our simulations. A preliminary study of the effect of stresses on

oxidation behavior revealed that oxidation is much higher in the presence of stresses. By comparing oxidation behavior in a oxygen rich and an inert environment, we found that high temperature creep behavior mainly depends on oxidation of carbon fiber. The property degradation at the carbon fiber level was homogenized and used to successfully compute the macroscopic degradation of mechanical properties. The decrease in elastic modulus during high temperature oxidation was found to follow the same trends at the decrease in carbon volume fraction.

Table 5.1: Solution scheme for multi–scale modeling of C/SiC

(1) Initialize macro-scale model and assign a microstructure to every integration point.

(2) Apply time increment Δt to the macro-scale problem.

(3) Iteration step: O_2 and CO_2 diffusion

  (3.1) Assemble the macroscopic stiffness matrix.

  (3.2) Solve the macroscopic system and compute density and the density gradient at each integration point.

  (3.3) Rotate density gradient vectors.

  (3.4) Loop over all integration points

    (a) (Only done for the first NR iteration) Update the carbon fiber radius using chemical reaction velosity.

    (b) Transfer densities to every point in the micro-scale using Eq. 3.10.

    (c) Calculate the volume averaged macro-flux (Eq. 3.16), the source term (Eq. 3.28), the macro-diffusivity (Eq. 5.52)

    (d) Rotate macro-flux vector and macro-diffusivity tensor according to carbon fiber direction

  (3.5) Assemble the macroscopic residual vector.

(4) Check convergence, if not converged go to step 3, otherwise go to step 5.

(5) Iteration step: Stress-strain

  (5.1) Assemble the macroscopic stiffness matrix.

  (5.2) Solve the macroscopic system and compute deformation gradient.

  (5.3) Rotate deformation gradient matrix.

  (5.4) Loop over all integration points

    (a) Transfer deformations to every point in the micro-scale using $\boldsymbol{u} = (\boldsymbol{F} - \boldsymbol{I})\boldsymbol{Y}$

    (b) Calculate the volume averaged the macro-elasticity (Eq. 5.31).

    (c) Rotate macro-elasticity tensor.

    (d) Obtain 4th order elasticity tensor from 2nd order tensor.

  (5.5) Assemble the macroscopic residual vector.

(6) Check convergence, if not converged go to step 5, otherwise go to step 2.

Table 5.2: Material properties employed in the multiscale model of 3D CMC oxidation

Material	E_1	E_2	ν_1	ν_2	G_{12}	α_1	α_2
Carbon fiber	115	31.7	16.1	0.19	0.14	-0.1×10^{-6}	7.0×10^{-6}
Matrix	250		0.14			4.6×10^{-6}	

Table 5.3: Porosity and surface area fraction for CMC oxidation simulations

Temp.(°C)	$Porosity$	$Surfaceareafraction$
600	0.430	0.14000
700	0.423	0.01481
800	0.400	0.01333
900	0.158	0.00427
950	0.037	0.00242
1100	0.004	0.00001

CHAPTER VI

Suggestions for future research

Experimental studies on high temperature materials are difficult due to the inability to reproduce the harsh environments in which these materials are used. Validated computer models are extremely important for these materials. In this thesis, a multi-scale homogenization method is presented that is used to model the material physics at macro- and micro-scales. The model includes discontinuities in field variables, fluxes, and moving interfaces. In chapter II, the model was validated with an analytical solution for phase change, and in subsequent chapters III, IV, and V, the approach was applied to the oxidation problem. We separated the computational domain into macro- and micro- scales to reduce computational expense and improve accuracy. The numerical treatments and establishment successfully demonstrated the potentials of the methodology. However, there are several avenues for more advance studies which can be roughly categorized into three areas: (i) Exploration of oxidation physics in new materials, including ultra high temperature composites (UHTCs). (ii) Modeling anisotropy in porosity and transport properties calibrated from advanced experimental studies. (iii) Modeling the effect of other degrading agents like moisture that accelerate degradation (iv) Modeling traction separation relationships in the matrix using molecular simulations to further understand matrix

damage at a fundamental level.

6.1 Modeling UHTCs

At extreme temperatures, SiC and ZrB_2 surfaces are directly exposed to the ambient conditions and may form a porous surface layer of oxides. A micro-scale model that provides a closer tie-in of this complex oxide layer morphology with mass and energy transfer at the surface is extremely desireable. The thermal boundary conditions for the microscale model need to obtained from flow simulations or plasma torch experiments. The numerical micro-scale model can be used to predict sub-surface temperature and species distribution. Tomographic imaging experiments are also extremely valuable for future studies. If a 3D microstructure of a oxidized specimen can be obtained, one could predict anisotropic porosities, 3D pore connectivity and effective properties (such as conductivity and elastic moduli) accurately. This data can be used in the microscale material model. Micro-scale 3D images can also be used to compute micro-crack densities and porosity evolution for developing models for mechanical damage during ablation. The models developed in this work can then be used at the micro-scale to compute oxygen and other gas specie concentrations in the porous oxide matrix and liquid oxides (e.g. boria, silica) under non-equilibrium conditions[53]. The computed oxygen vapor pressure can be used in bulk reaction rate equations to predict overall rates of recession and energy release at different exposure conditions.

6.2 Anisotropic diffusion

The comparison between theory and experiment clearly indicates that the details of the geometry of anisotropic systems exert an important influence on effective transport coefficients in [33]. The theoretical calculations indicate that the effective

diffusivity tensor cannot be accurately predicted in terms of only the void fraction and the particle geometry. Recently, effects of direction dependent diffusivity have been investigated by systematically varying rod packing density in [46]. In this study, the direction dependent normalized diffusivity is obtained using lattice walk algorithm [47], and it is shown that anisotropic pore structure of the rod system enables high diffusive migration along the longitudinal direction.

Furthermore, in Payne and co-workers [80, 54], a review of Darcy's law and the influence of anisotropic permeability was explored. The earlier contributions that introduce methods of measuring anisotropic permeability of porous media was presented in [58]. Because the diffusion of gas species in the pore space is restricted by anisotropic permeability, the resultant diffusivity was also anisotropic. In the previous chapters, the importance of geometry also has been emphasized. different material configurations as well as the existence of discontinuity introduced time dependent conductivity, porosity, diffusivity, and permeability. Further extending these models, introduction of anisotropic properties can be implemented to enhance simulations. In fact, isotropic material properties are used in the previous chapters; however when homogenization approaches are used, partially anisotropic effective quantities are transferred to the macro-scale model. In order to utilize the direction–dependent properties when using Taylor micro-scale conditions, it is necessary to find anisotropic material properties at the level of micro-scale.

6.3 Modeling micro- damage with molecular dynamics

Carbon fiber oxidation at high temperatures has been observed to initiate along cracks in the matrix between the fiber tows and the SiC seal coat. Thus, for evaluating the mechanical properties of the composite at high temperatures, also becomes

essential to couple the effect of operating stresses on interfacial failure in the seal coatings. Increase in crack widths and interface separation in the presence of stresses and their effect on oxidation needs to be studied using molecular models. To obtain accurate transport coefficients and reaction rate constants for the microstructural model of the fiber and coating material, one could perform molecular dynamic simulations([73, 63, 72, 82, 83]) with accurate multi-body potentials [71]. Apart from the value of obtaining reaction rates for the micro-scale model with minimal physical assumptions, such a model gives us the predictive ability needed to design new fiber coating materials to minimize oxidation. The proposed modeling methodology is shown in Fig. 6.1. Results of crack prediction in microstructure with molecular

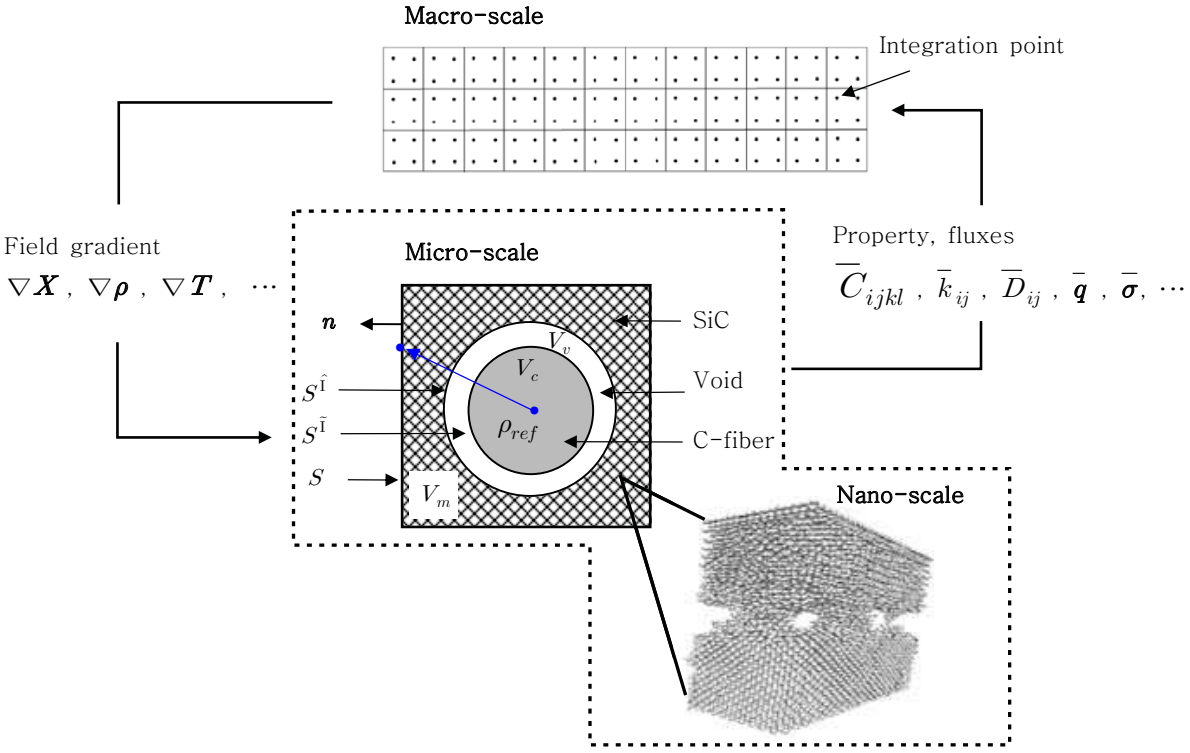

Figure 6.1: *The transport parameters such as diffusivity and traction–separation laws for the micro-scale model can be calculated from molecular simulations. We performed a preliminary study to this end in Ref. [37]*

dynamics simulation [37] are shown in the Fig. 6.2 and 6.3. In this simulation, it is

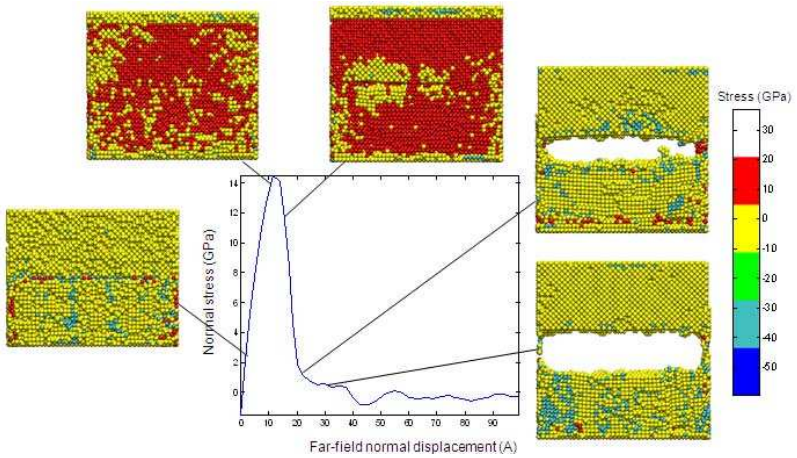

Figure 6.2: *Normal stress displacement response of the interface model: During tensile separation, the normal stress displacement response shows a dominant peak with associated peak stress. Peak stress is around 14 GPa.*

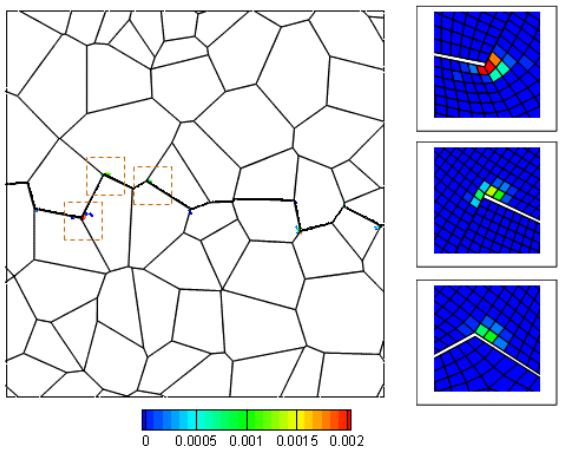

Figure 6.3: *The plastic strain locations during initiation of plasticity. The plastic strains are concentrated on grain boundary triple points or sharp corners(SiC is polycrystalline.)*

observed that the macroscopically observed nonlinearity in the stress-strain response is mainly due to the inelastic response of the grain boundaries. Plastic deformation in the interior of the grains, prior to the initiation of grain boundary cracks, was not observed. The stress concentrations at the tips of the distributed grain boundary cracks, and at grain boundary triple junctions, cause a limited amount of plastic deformation in the high strength grain interiors. Simulations such as this will be valuable in understanding parameters such as fracture toughness at the continuum

scale for further refining damage or cohesive crack models.

6.4 SiC oxidation - effect of moisture

In chapters dealing with carbon fiber reinforced silicon carbide (C/SiC), the matrix is assumed to withstand high temperature conditions without oxidation. This assumption is supported by Jorgensen([31]) who noted that the rate of oxidation is very slow (an order of magnitude slower) compared to carbon fiber; carbon fiber is consumed in an hour (see [22] and silicon carbide takes several days. However, the existence of moisture in the gaseous atmosphere strongly affects the oxidation rate. Further experimental evidences of the moisture effects on the stress rupture behavior of ceramic matrix composite (CMC) has been presented in [40]. In attempting to predict life time of C/SiC in actual use, modeling the effect of other degrading agents such as moisture becomes essential.

APPENDICES

APPENDIX A

Volume average of heat flux at the micro-scale

Using the governing equation at the micro-scale (Eq. 2.8), we obtain the expression for $\nabla \cdot \boldsymbol{xq}$ as:

$$\nabla \cdot \boldsymbol{xq} = \boldsymbol{q} + \boldsymbol{x}\nabla \cdot \boldsymbol{q} = \boldsymbol{q} - \boldsymbol{x}\nabla \cdot (\rho c T \boldsymbol{v})$$

Using the above equation and application of the generalized divergence theorem, we can obtain the volume average of heat flux as:

$$\frac{1}{V}\int \boldsymbol{q} dV = \frac{1}{V}\int_V (\nabla \cdot \boldsymbol{xq} + \boldsymbol{x}\nabla \cdot (\rho c T \boldsymbol{v}))dV$$
$$= \frac{1}{V}\int_S \boldsymbol{x} q_n dS + \frac{1}{V}\int_{S^I} \boldsymbol{x}[|q_n|]dS^I + \frac{1}{V}\int_V \boldsymbol{x}\nabla \cdot (\rho c T \boldsymbol{v})dV$$

The last term in the above equation can be rewritten as:

$$\frac{1}{V}\int_V \boldsymbol{x}\nabla \cdot (\rho c T \boldsymbol{v})dV = \frac{1}{V}\int_V \nabla \cdot (\rho c T \boldsymbol{x} \otimes \boldsymbol{v})dV - \frac{1}{V}\int_V \rho c T \boldsymbol{v} dV$$
$$= \frac{1}{V}\int_{S^I} \boldsymbol{x}[|\rho c|]T v_n dS^I$$

In the above derivation, we have used the fact that particle velocity is zero at all points in the domain except at the interface to eliminate the terms involving volume

integral of velocity. The above equation can be used to obtain the expression for volume average of heat flux as:

$$\frac{1}{V}\int \boldsymbol{q} dV = \frac{1}{V}\int_S \boldsymbol{x} q_n dS + \frac{1}{V}\int_{S^I} \boldsymbol{x}([|q_n|] + [|\rho c|]Tv_n) dS^I = \frac{1}{V}\int_S \boldsymbol{x} q_n dS$$

As a consequence of this derivation, we prove that the volume averaged heat flux can be obtained using information on the boundary of the microstructure.

APPENDIX B

Homogenized Flux Derivation Based on Hill's Macro-homogeneity Condition

The fluxes in the homogenization approach are derived such that the macro–homogeneity condition is satisfied. The micro-scale partial density field of each species i is denoted as ρ and no subscripts are used to maintain generality. Based on local mass balance equation (Eq. 3.19), it can be proved that the integral of normal mass flux over the unit cell surface goes to zero as follows:

$$\begin{aligned}\int_S q_n dS &= \int_V \nabla \cdot \boldsymbol{q} dV - \int_{S^I} [|q_n|] dS^I \\ &= -\int_V \nabla \cdot (\rho \boldsymbol{v}) dV - \int_{S^I} [|q_n|] dS^I \\ &= -\int_{S^I} (v_n [|\rho|] + [|q_n|]) dS^I = 0\end{aligned}$$

The above relation is subsequently used for homogenization of the micro-scale flux.

Application of the governing equation (Eq. 3.18) changes the macro-homogeneity condition to the following form:

$$\overline{\nabla \rho} \cdot \overline{\boldsymbol{q}} = \overline{\nabla \rho \cdot \boldsymbol{q}} = \frac{1}{V} \int_V (\nabla \cdot (\rho \boldsymbol{q}) - \rho \nabla \cdot \boldsymbol{q}) dV$$
$$= \frac{1}{V} \int_S \rho q_n dS + \frac{1}{V} \int_{S^I} [|\rho q_n|] dS^I + \frac{1}{V} \int_V \rho \nabla \cdot (\rho \boldsymbol{v}) dV$$

We can reduce the first term in the above equation using the definition of micro-scale density (Eq. 3.1) and the homogeneous boundary conditions as:

$$\frac{1}{V}\int_S \rho q_n dS = \frac{1}{V}\int_S [\rho_{ref} + \overline{\nabla\rho}\cdot\boldsymbol{x}]q_n dS$$
$$= \overline{\nabla\rho}\cdot\frac{1}{V}\int_S \boldsymbol{x}q_n dS \text{ (using } \int_S q_n dS = 0)$$

The second and third terms in the above equations are again reduced using the generalized divergence theorem as:

$$\frac{1}{V}\int_{S^I}[|\rho q_n|]dS^I + \frac{1}{V}\int_V \rho\nabla\cdot(\rho\boldsymbol{v})dV$$
$$= \frac{1}{V}\int_{S^I}[|\rho q_n|]dS^I + \frac{1}{V}\int_V \nabla\cdot(\rho^2\boldsymbol{v})dV - \frac{1}{V}\int_V \nabla\rho\cdot(\rho\boldsymbol{v})dV$$
$$= \frac{1}{V}\int_{S^I}[|\rho q_n|]dS^I + \frac{1}{V}\int_{S^I}[|\rho^2|]v_n dS^I$$

In the above derivation, we use local mass balance equation and the fact that the particle velocity is zero at all points in the material except the interface. The second term in the above equation contains the oxygen density field and flux jump across the oxidizing interface. This term is reduced as follows:

$$\frac{1}{V}\int_{S^I}[|\rho q_n|]dS^I + \frac{1}{V}\int_V \rho\nabla\cdot(\rho\boldsymbol{v})dV$$
$$= \frac{1}{V}\int_{S^I}[|\rho q_n|]dS^I + \frac{1}{V}\int_V \nabla\cdot(\rho^2\boldsymbol{v})dV - \frac{1}{V}\int_V \nabla\rho\cdot(\rho\boldsymbol{v})dV$$
$$= \frac{1}{V}\int_{S^I}[|\rho q_n|]dS^I + \frac{1}{V}\int_{S^I}[|\rho^2|]v_n dS^I$$

In the above derivation, we have used the notion that oxygen density and oxygen flux is small inside the Carbon fiber. Combining all the above equations, the macroscopic flux is obtained as:

$$\overline{\boldsymbol{q}} = \frac{1}{V}\int_S \boldsymbol{x}q_n dS$$

Using the governing equation at the micro-scale (Eq. 3.18), we obtain the expression for $\nabla \cdot \boldsymbol{xq}$ as:

$$\nabla \cdot \boldsymbol{xq} = \boldsymbol{q} + \boldsymbol{x}\nabla \cdot \boldsymbol{q} = \boldsymbol{q} - \boldsymbol{x}\nabla \cdot (\rho \boldsymbol{v})$$

Using the above equation and application of the generalized divergence theorem, we can obtain the volume average of heat flux as:

$$\frac{1}{V}\int \boldsymbol{q} dV = \frac{1}{V}\int_V (\nabla \cdot \boldsymbol{xq} + \boldsymbol{x}\nabla \cdot (\rho \boldsymbol{v}))dV$$
$$= \frac{1}{V}\int_S \boldsymbol{x} q_n dS + \frac{1}{V}\int_{S^I} \boldsymbol{x}[|q_n|]dS^I + \frac{1}{V}\int_V \boldsymbol{x}\nabla \cdot (\rho \boldsymbol{v})dV$$

The last term in the above equation can be rewritten as:

$$\frac{1}{V}\int_V \boldsymbol{x}\nabla \cdot (\rho \boldsymbol{v})dV = \frac{1}{V}\int_V \nabla \cdot (\rho \boldsymbol{x} \otimes \boldsymbol{v})dV - \frac{1}{V}\int_V \rho \boldsymbol{v} dV$$
$$= \frac{1}{V}\int_{S^I} \boldsymbol{x}[[\rho]] v_n dS^I$$

In the above derivation, we have used the fact that particle velocity is zero at all points in the domain except at the interface to eliminate the terms involving volume integral of velocity. The above equation can be used along with the interface mass balance condition (Eq. 3.19) to obtain the expression for volume average of mass flux as:

$$\frac{1}{V}\int \boldsymbol{q} dV = \frac{1}{V}\int_S \boldsymbol{x} q_n dS + \frac{1}{V}\int_{S^I} \boldsymbol{x}([|q_n|] + [[\rho]] v_n)dS^I = \frac{1}{V}\int_S \boldsymbol{x} q_n dS = \overline{\boldsymbol{q}}$$

As a consequence of this derivation, we prove that the micro–scale volume average flux is equal to the macro–scale flux as a consequence of Hill's macro–homogeneity condition.

BIBLIOGRAPHY

BIBLIOGRAPHY

[1] TB Anderson and R Jackson. Fluid mechanical description of fluidized beds. equations of motion. *Industrial & Engineering Chemistry Fundamentals*, 6(4):527–539, 1967.

[2] JL Auriault. Effective macroscopic description for heat conduction in periodic composites. *International Journal of Heat and Mass Transfer*, 26(6):861 – 869, 1983.

[3] I Babuska. Solution of interface problems by homogenization. i. *SIAM Journal on Mathematical Analysis*, 7(5):603–634, 1976.

[4] I Babuska. Solution of interface problems by homogenization. ii. *SIAM Journal on Mathematical Analysis*, 7(5):635–645, 1976.

[5] I Babuska. Solution of interface problems by homogenization. iii. *SIAM Journal on Mathematical Analysis*, 8(6):923–937, 1977.

[6] MP Bacos, JM Dorvaux, O Lavigne, and J Talandier. C/c composite oxidation model: Iii. physical basis, limitations and applications. *Carbon*, 38(1):105–117, 2000.

[7] NS Bakhvalov and G Panasenko. *Homogenisation: Averaging Processes in Periodic Media*. Mathematical Problems in the Mechanics of Composite Materials(Mathematics and its Applications). Kluwer Academic Publishers, 1989.

[8] S Balay, K Buschelman, V Eijkhout, WD Gropp, D Kaushik, MG Knepley, LC McInnes, BF Smith, and H Zhang. *PETSc Users Manual. Tech. Rep. ANL-95/11 - Revision 2.1.5*. Argonne National Laboratory, 2004.

[9] T Belytschko, S Loehnert, and JH Song. Multiscale aggregating discontinuities: A method for circumventing loss of material stability. *International Journal for Numerical Methods in Engineering*, 73(6):869–894, 2008.

[10] RB Bird, WE Stewart, and EN Lightfoot. *Transport Phenomena*. John Wiley & Sons, New York, NY, 1960.

[11] C Boutin. Microstructural influence on heat conduction. *International Journal of Heat and Mass Transfer*, 38(17):3181 – 3195, 1995.

[12] B Budiansky. On the elastic moduli of some heterogeneous materials. *Journal of the Mechanics and Physics of Solids*, 13(4):223–227, 1965.

[13] J Crank. *Free and Moving Boundary Problems.* Clarendon Press, Oxford, 1985.

[14] R Dias, JA Teixeira, M Mota, and A Yelshin. Tortuosity variation in a low density binary particulate bed. *Separation and Purification Technology*, 51(2):180 – 184, 2006.

[15] C Eck, P Knabner, and S Korotov. A two-scale method for the computation of solid-liquid phase transitions with dendritic microstructure. *Journal of Computational Physics*, 178(1):58 – 80, 2002.

[16] AJ Eckel, JD Cawley, and TA Parthasarathy. Oxidation kinetics of a continuous carbon phase in a nonreactive matrix. *Journal of the American Ceramic Society*, 78(4):972–980, 1995.

[17] WL Edward. Neutron transport and diffusion in inhomogeneous media. i. *Journal of Mathematical Physics*, 16(7):1421–1427, 1975.

[18] N Epstein. On tortuosity and the tortuosity factor in flow and diffusion through porous media. *Chemical Engineering Science*, 44(3):777–779, 1989.

[19] DE Glass. Ceramic matrix composite (cmc) thermal protection systems (tps) and hot structures for hypersonic vehicles. aiaa paper 2008-2682. In *15th AIAA International Space Planes and Hypersonic Systems and Technologies Conference, 28 Apr.1-May*, Dayton, OH, United States, 2008.

[20] V Gravemeier, S Lenz, and W Wall. Towards a taxonomy for multiscale methods in computational mechanics: building blocks of existing methods. *Computational Mechanics*, 41(2):279–291, 2008.

[21] J Guedes and N Kikuchi. Preprocessing and postprocessing for materials based on the homogenization method with adaptive finite element methods. *Computer Methods in Applied Mechanics and Engineering*, 83(2):143 – 198, 1990.

[22] MC Halbig. The oxidation kinetics of continuous carbon fibers in a cracked ceramic matrix composite. Technical report, NASA/TM-2001-210520, 2001.

[23] MC Halbig. Carbon oxidation studies and the evaluation of oxidation inhibited c/sic composites. In *28th Annual Conference on Composites, Materials and Structures, 26-30 Jan.*, Cocoa Beach, FL, U.S.A. United States, 2004.

[24] Z Hashin. Analysis of composite materials—a survey. *Journal of Applied Mechanics*, 50(3):481–505, 1983.

[25] Z Hashin and S Shtrikman. A variational approach to the theory of the elastic behaviour of polycrystals. *Journal of the Mechanics and Physics of Solids*, 10(4):343–352, 1962.

[26] R Hill. Elastic properties of reinforced solids: Some theoretical principles. *Journal of the Mechanics and Physics of Solids*, 11(5):357–372, 1963.

[27] R Hill. A self-consistent mechanics of composite materials. *Journal of the Mechanics and Physics of Solids*, 13(4):213–222, 1965.

[28] R Hill. On constitutive macro-variables for heterogeneous solids at finite strain. *Proceedings of the Royal Society of London. A. Mathematical and Physical Sciences*, 326(1565):131–147, 1972.

[29] SJ Hollister and N Kikuchi. A comparison of homogenization and standard mechanics analyses for periodic porous composites. *Computational Mechanics*, 10(2):73–95, 1992.

[30] M Jiang, I Jasiuk, and M Ostoja-Starzewski. Apparent thermal conductivity of periodic two-dimensional composites. *Computational Materials Science*, 25(3):329 – 338, 2002.

[31] PJ Jorgensen, ME Wadsworth, and IB Cutler. Oxidation of silicon carbide. *Journal of the American Ceramic Society*, 42(12):613–616, 1959.

[32] JB Keller. Effective behavior of heterogeneous media, proc. symposium on statistical mechanics and statistical methods. pages 631–644. Plenum Press, New York, 1977.

[33] JH Kim, JA Ochoa, and S Whitaker. Diffusion in anisotropic porous media. *Transport in Porous Media*, 2(4):327–356, 1987.

[34] V Kouznetsova, WAM Brekelmans, and FPT Baaijens. An approach to micro-macro modeling of heterogeneous materials. *Computational Mechanics*, 27(1):37–48, 2001.

[35] PD Lee, A Chirazi, RC Atwood, and W Wang. Multiscale modelling of solidification microstructures, including microsegregation and microporosity, in an al-si-cu alloy. *Materials Science and Engineering A*, 365(1-2):57 – 65, 2004.

[36] S Lee and V Sundararaghavan. Multi-scale homogenization of moving interface problems with flux jumps: application to solidification. *Computational Mechanics*, 44(3):297–307, 2009.

[37] S Lee and V Sundararaghavan. Calibration of nanocrystalline grain boundary model using atomistic simulations. *International Journal for Multiscale Computational Engineering*, 8(5), 2010.

[38] S Lee and V Sundararaghavan. Multi-scale modeling of moving interface problems with flux and field jumps: Application to oxidative degradation of ceramic matrix composites. *International Journal for Numerical Methods in Engineering*, 2010. Published online.

[39] RJ LeVeque. *Numerical methods for conservation laws*. Birkhauser, Basel, 1992.

[40] S Mall and JL Ryba. Effects of moisture on tensile stress rupture behavior of a sic/sic composite at elevated temperatures. *Composites Science and Technology*, 68(1):274–282, 2008.

[41] WL McCabe, JC Smith, and P Harriott. *Unit Operations of Chemical Engineering*. McGraw-Hill, New York, 2005.

[42] H Mei, LF Cheng, and LT Zhang. Damage mechanisms of c/sic composites subjected to constant load and thermal cycling in oxidizing atmosphere. *Scripta Materialia*, 54(2):163–168, 2006.

[43] H Mei, LF Cheng, and LT Zhang. Thermal cycling damage mechanisms of c/sic composites in displacement constraint and oxidizing atmosphere. *Journal of the American Ceramic Society*, 89(7):2330–2334, 2006.

[44] C Miehe. Numerical computation of algorithmic (consistent) tangent moduli in large-strain computational inelasticity. *Computer Methods in Applied Mechanics and Engineering*, 134(3-4):223 – 240, 1996.

[45] C Miehe, J Schroeder, and J Schotte. Computational homogenization analysis in finite plasticity simulation of texture development in polycrystalline materials. *Computer Methods in Applied Mechanics and Engineering*, 171(3-4):387 – 418, 1999.

[46] Y Nakashima and S Kamiya. Anisotropic diffusion in fibrous porous media. 13(1):1–11, 2010.

[47] Y Nakashima, S Kamiya, and T Nakano. Diffusion ellipsoids of anisotropic porous rocks calculated by x-ray computed tomography-based random walk simulations. *Water Resour. Res.*, 44(12):W12435, 2008.

[48] AK Noor and RS Shah. Effective thermoelastic and thermal properties of unidirectional fiber-reinforced composites and their sensitivity coefficients. *Composite Structures*, 26(1-2):7–23, 1993.

[49] M Ostoja-Starzewski. Towards stochastic continuum thermodynamics. *Journal of Non-Equilibrium Thermodynamics*, 27(4):335–348, 2002.

[50] M Ostoja-Starzewski and J Schulte. Bounding of effective thermal conductivities of multiscale materials by essential and natural boundary conditions. *Phys. Rev. B*, 54(1):278–285, Jul 1996.

[51] I Ozdemir, WAM Brekelmans, and MGD Geers. Computational homogenization for heat conduction in heterogeneous solids. *International Journal for Numerical Methods in Engineering*, 73(2):185–204, 2008.

[52] I Ozdemir, WAM Brekelmans, and MGD Geers. FE^2 computational homogenization for the thermo-mechanical analysis of heterogeneous solids. *Computer Methods in Applied Mechanics and Engineering*, 198(3-4):602 – 613, 2008.

[53] TA Parthasarathy, RA Rapp, M Opeka, and RJ Kerans. A model for the oxidation of zrb2, hfb2 and tib2. *Acta Materialia*, 55:5999–6010, 2007.

[54] LE Payne, JF Rodrigues, and B Straughan. Effect of anisotropic permeability on darcy's law. *Mathematical Methods in the Applied Sciences*, 24(6):427–438, 2001.

[55] SC Quek, AM Waas, KW Shahwan, and V Agaram. Analysis of 2d triaxial flat braided textile composites. *International Journal of Mechanical Sciences*, 45(6-7):1077–1096, 2003.

[56] H Rafii-Tabar and A Chirazi. Multi-scale computational modelling of solidification phenomena. *Physics Reports*, 365(3):145 – 249, 2002.

[57] VS Rao, TJR Hughes, and K Garikipati. On modelling thermal oxidation of silicon ii: numerical aspects. *International Journal for Numerical Methods in Engineering*, 47(1-3):359–377, 2000.

[58] PA Rice, DJ Fontugne, RG Latini, G Raimondo, and AJ Barduhn. Anisotropic permeability in porous media. 62(6):31, 1970.

[59] RW Rice. *Porosity of ceramics*. Marcel Dekker, New York, N. Y., 1998.

[60] BW Rosen and Z Hashin. Effective thermal expansion coefficients and specific heats of composite materials. *International Journal of Engineering Science*, 8(2):157–173, 1970.

[61] LI Rubenstein. *The Stefan problem, Translations of Mathematical Monographs*, volume 27. American Mathematical Society, Providence, RI, 1971.

[62] E Sanchez-Palencia. Comportements local et macroscopique d'un type de milieux physiques heterogenes. *International Journal of Engineering Science*, 12(4):331–351, 1974.

[63] J Schiotz, T Vegge, FDD Tolla, and KW Jacobsen. Atomic-scale simulations of the mechanical deformation of nanocrystalline metals. *Physical Review B*, 60(17):11971, 1999.

[64] W Shyy, HS Udaykumar, MM Rao, and RW Smith. *Computational Fluid Dynamics with Moving Boundaries*. Dover, Mineola, New York, 1st edition, 2007.

[65] O Sigmund and S Torquato. Design of materials with extreme thermal expansion using a three-phase topology optimization method. *Journal of the Mechanics and Physics of Solids*, 45(6):1037 – 1067, 1997.

[66] JC Slattery. Flow of viscoelastic fluids through porous media. *AIChE Journal*, 13(6):1066–1071, 1967.

[67] RJM Smit, WAM Brekelmans, and HEH Meijer. Prediction of the mechanical behavior of nonlinear heterogeneous systems by multi-level finite element modeling. *Computer Methods in Applied Mechanics and Engineering*, 155(1-2):181 – 192, 1998.

[68] A Srikanth and N Zabaras. A computational model for the finite element analysis of thermoplasticity coupled with ductile damage at finite strains. *International Journal for Numerical Methods in Engineering*, 45(11):1569–1605, 1999.

[69] RM Sullivan. A model for the oxidation of carbon silicon carbide composite structures. *Carbon*, 43(2):275–285, 2005.

[70] V Sundararaghavan and N Zabaras. Design of microstructure-sensitive properties in elasto-viscoplastic polycrystals using multi-scale homogenization. *International Journal of Plasticity*, 22(10):1799–1824, 2006.

[71] V Sundararaghavan and N Zabaras. Weighted multibody expansions for computing stable structures of multiatom systems. *Physical Review B*, 77(6):064101, 2008.

[72] H Van Swygenhoven. Plastic deformation in metals with nanosized grains: atomistic simulations and experiments. *Materials Science Forum*, 447-448:3–10, 2004.

[73] H Van Swygenhoven, M Spaczer, A Caro, and D Farkas. Competing plastic deformation mechanisms in nanophase metals. *Physical Review B*, 60(1):22, 1999.

[74] L Tan and N Zabaras. A level set simulation of dendritic solidification of multi-component alloys. *Journal of Computational Physics*, 221(1):9–40, 2007.

[75] L Tan and N Zabaras. Multiscale modeling of alloy solidification using a database approach. *Journal of Computational Physics*, 227(1):728 – 754, 2007.

[76] MJ Verrilli and A alomino. Temperature dependence on the strength and stress rupture behavior of a carbon-fiber reinforced silicon carbide matrix (c/sic) composite. *Ceramic Engineering and Science Proceedings*, 24(4):443–449, 2003.

[77] C Wang and C Beckermann. Equiaxed dendritic solidification with convection: Part i. multiscale/multiphase modeling. *Metallurgical and Materials Transactions A*, 27(9):2754–2764, 1996.

[78] JT Ward and JB Hamblen. Influence of diffusion of oxygen on the rate of combustion of solid carbon. *Industrial & Engineering Chemistry*, 19(9):1025–1027, 1927.

[79] S Whitaker. Diffusion and dispersion in porous media. *AIChE Journal*, 13(3):420–427, 1967.

[80] S Whitaker. The forchheimer equation: A theoretical development. *Transport in Porous Media*, 25(1):27–61, 1996.

[81] FM White. *Fluid Mechanics*. McGraw-Hill, New York, 2001.

[82] V Yamakov, E Saether, DR Phillips, and EH Glaessgen. Molecular-dynamics simulation-based cohesive zone representation of intergranular fracture processes in aluminum. *Journal of the Mechanics and Physics of Solids*, 54(9):1899–1928, 2006.

[83] V Yamakov, D Wolf, M Salazar, SR Phillpot, and H Gleiter. Length-scale effects in the nucleation of extended dislocations in nanocrystalline al by molecular-dynamics simulation. *Acta Materialia*, 49(14):2713–2722, 2001.